PEDRO WALFIR MARTINS E SOUZA NETO

The Circulation On The Rio Grande Rise: Mean Flow, Internal Tides, and Eddies

São Paulo

2022

PEDRO WALFIR MARTINS E SOUZA NETO

The Circulation On The Rio Grande Rise: Mean Flow, Internal Tides, and Eddies

A thesis submitted to the Instituto Oceanográfico of the Universidade de São Paulo in partial fulfilment for the degree of Master of Science in Oceanography, with emphasis in Physical Oceanography.

Advisor: Prof. Dr. Ilson Carlos Almeida da Silveira

São Paulo

2022

Souza-Neto, Pedro Walfir. **The Circulation On The Rio Grande Rise: Mean Flow, Internal Tides, and Eddies**. A thesis submitted to the Instituto Oceanográfico of the Universidade de São Paulo in partial fulfilment for the degree of Master of Science in Oceanography, with emphasis in Physical Oceanography.

Approved on 05/05/2022

Corrected Version

Judging Committee

Prof PhD _____ Institution _____

Grade _____ Signature _____

Prof PhD _____ Institution _____

Grade _____ Signature _____

Prof PhD _____ Institution _____

Grade _____ Signature _____

Acknowledgments

I would like to share my most sincere acknowledgment to everyone who has supported me along this journey so far. Especially to those who were by my side during this period which was difficult for many. A special thanks to my mother Rosália and father Pedro, without your support and guidance none of this would be possible. You are responsible for all the things I have achieved, without the solid foundation you have given me in all aspects of life, I would hardly be where I am today. I love you. I am also grateful for the two wonderful sisters I have and love very much. Ninha and Lu, I miss you. Also, I would like to express my gratitude to my beloved girlfriend Alana, an amazing woman who is always by my side, and I am lucky to share every moment with her. I love you so much.

To my advisor and friend Ilson, thank you for all the guidance, teachings, and opportunities given during the time I was at LaDO. I hope that I can work directly with you in the next years.

I thank all the friends who came by and are at LaDO. Every day it is possible to learn a little from you. A particular acknowledgment to my friend Borracha, with whom I shared my master's subjects and learned to model. Nor could I forget my friend Xuxa for his help with the model and the particular interest and attention given during the development of my research.

Furthermore, I am grateful for everyone I had the opportunity to meet during my undergraduate and graduate studies. A hug to all of the XIV class. Especially for my friends: Maromba, Bozo, Tele, Mega, and Borracha.

I would like to thank all my teachers for their shared knowledge. In particular, Professor Belmiro Castro, Ilson Silveira, Paulo Polito, Olga Sato, Pedro Leite, Marcelo Dottori, Joseph Harari, Ricardo Camargo and Sueli Godoi for their precious teaching.

I can't forget to thank Ricardo, Eder, Daniel, Ana Paula, Silvana, Leticia, Wagner, and Marta for the support that makes things easier during the bachelor's and master's.

Finally, this study was financed in part by the Coordenação de Aperfeiçoamento de Pessoal de Nível Superior - Brasil (CAPES) - Finance Code 001, and by Fundação de Amparo à Pesquisa do Estado de São Paulo (FAPESP) Proc. 2020/04315-0.

"As long as you live,
keep learning how to live."

– Seneca

RESUMO

Souza-Neto, Pedro Walfir. **A Circulação na Elevação do Rio Grande: Escoamento médio, marés internas e vórtices**. 2022. Dissertação de Mestrado - Instituto Oceanográfico, Universidade de São Paulo, São Paulo.

A Elevação do Rio Grande (ERG) é uma elevação oceânica assísmica com formato aproximadamente circular no Oceano Atlântico Sul, localizada em cerca de 31°S e 35°W. A feição se estende desde o fundo do oceano até aproximadamente 500 m de profundidade. A ERG é cortada de oeste-leste por uma falha denominada Fenda Cruzeiro do Sul (FCS). A ERG é um local importante para a exploração futura de crostas de Fe-Mn e pode levar à expansão da Zona Econômica Exclusiva do Brasil. Apesar disso, ainda são poucas as informações sobre a circulação local e sua variabilidade. O principal objetivo dessa pesquisa é caracterizar os padrões da circulação média dentro do FCS e identificar os fenômenos associados à sua variabilidade. Para atingir nosso objetivo usamos dados *in-situ*, bem como modelagem numérica regional, que revela que a ERG é uma região com vários processos dinâmicos ocorrendo. Entre eles temos a formação de: circulações anticiclônicas, marés internas e vórtices de submesoescala. De forma geral, o ramo sul da Corrente Sul Equatorial se bifurca em torno da ERG e é um dos mecanismos responsáveis por forçar a circulação dentro da FCS. Entre 500 e 1200 m, ao redor dos cumes da ERG, observa-se a formação de circulações anticiclônicas assimétricas que desempenham um papel importante em ditar a circulação dentro da FCS. Acima da ERG, as marés internas são um dos principais mecanismos geradores de variabilidade, com amplitude da mesma magnitude do escoamento médio. Dentro da FCS, ela é responsável por gerar inversões no campo de velocidade. As amplitudes de maré mais altas estão localizadas nos cumes do ERG, com um segundo pico de amplitude adjacente ao fundo no vale da FCS. Os picos de amplitude provavelmente estão relacionados à formação de feixes de maré devido à topografia íngreme. A circulação dentro do FCS é dominada por pertur-

bações que muitas vezes geram vórtices de submesoescala. Dentro do FCS existem três locais principais de formação de vórtices, (1) a abertura leste (34,5°W), (2) a abertura do talude norte da FCS (35°W) e (3) a ponta oeste da abertura do talude norte da FCS. Em relação aos gatilhos dos vórtices, a análise de conversão de energia indica a presença de instabilidade baroclínica e barotrópica. Além disso, existe o desenvolvimento de um misto de instabilidade inercial e simétrica.

Palavras-chave: Elevação do Rio Grande, Fenda Cruzeiro do Sul, circulação anticiclônica, marés internas, vórtices de submesoescala

ABSTRACT

Souza-Neto, Pedro Walfir. **The Circulation On The Rio Grande Rise: Mean Flow, Internal Tides, and Eddies**. 2022. Master's Thesis - Oceanographic Institute, University of Sao Paulo, Sao Paulo.

The Rio Grande Rise (RGR) is an aseismic oceanic elevation with an approximately circular shape in the South Atlantic Ocean, whose center is located at about 31°S and 35°W. The feature extends from 5000 m to approximately 500 m in depth. The RGR is cut from west-east by a fault called Cruzeiro do Sul Rift (CSR). The RGR is an important site for future exploration of Fe-Mn crusts and can lead to an expansion of the Brazil's Exclusive Economic Zone. Nevertheless, there is virtually no information about local circulation and its variability. The main objective of this research is to characterize the mean circulation pattern within the CSR, and identify the phenomena associated with its variability. To achieve our objective we use *in-situ* data, as well as regional numerical modeling, to show that the RGR is a region with several dynamic processes taking place simultaneously. Among them we have the formation of: anticyclonic circulations, internal tides and submesoscale eddies. In general, the southern branch of the South Equatorial Current (SEC) bifurcates around the RGR and is one of the mechanisms responsible for forcing the circulation inside the CSR. Between 500 and 1200 m, around the RGR summits, we observe the formation of asymmetric anticyclonic circulations that play an important role in dictating the circulation inside the CSR. Above the RGR, the internal tides are one of the main mechanisms that generate variability, with wave amplitudes of the same magnitude as the mean flow. Inside the CSR, tides are responsible for generating inversions in the velocity field. Higher tidal amplitudes are located at the RGR summits, with second amplitude peaks adjacent to the bottom at the CSR valley. The amplitude peaks are probably related to the formation of tidal beams due to the steep topography. The circulation within the CSR is dominated by perturbations on impinging SEC branches that often generate submesoscale eddies. Inside the CSR there are three major sites of eddy formation, (1) the east opening (34.5°W), (2) the CSR northern slope opening (35°W) and (3) the west tip of the CSR

northern slope opening. In regards to the eddy triggers, the energy conversion analysis indicates the presence of baroclinic and barotropic instability. Also, there is the development of a mix of inertial and symmetric instabilities.

Key-words: Rio Grande Rise, Fenda Cruzeiro do Sul, anticyclonic circulation, internal tides, submesoscale eddies

List of Figures

List of Tables

Acronyms

AAIW	Antarctic Intermediate Water
ADCP	Acoustic Doppler Current Profiler
AGRIF	Adaptative Mesh Refinement In Fortran
AODN	Astralian Ocean Data Network
BC	Brazil Current
BP	Buoyancy Production
BRDR	Baroclinic Rossby Deformation Radius
CMEMS	Copernicus Marine Environment Monitoring Service
CODAS	Common Ocean Data Access System
CPRM	Companhia de Pesquisa de Recursos Minerais
CROCO	Coastal and Regional Ocean COmmunity model
CSR	Cruzeiro do Sul Rift
CTD	Conductivity, Temperature, Depth and Oxygen
EOFs	Empirical orthogonal functions
ERA5	ECMWF Reanalysis v5
GEBCO	GEneral Bathymetric Chart of the Oceans
HC	Hunter Channel
HSP	Horizontal Shear Production
IMOS	Integrated Marine Observing System
IWBC	Intermediate Western Boundary Current
KPP	K-Profile Parameterization
LADCP	Lowered Acoustic Doppler Current Profiler
NADW	North Atlantic Deep Water
NEMO	Nucleus for European Modelling of the Ocean
OGCM	Ocean General Circulation Model
PDF	Probability Dnesity Function
PSD	Power Spectrum Density
QG	Quasi Geostrophic
RGR	Rio Grande Rise

RGRe	Rio Grande Rise east
RGRw	Rio Grande Rise west
Ri	Richardson number
Ro	Rossby number
ROMS	Regional Ocean Model System
SACW	South Atlantic Central Water
SEC	South Equatorial Current
SP	Shear Production
SPP	São Paulo Plateau
SSEC	Southern South Equatorial Current
std	standard deviation
TW	Tropical Water
UCDW	Upper Circumpolar Deep Water
VC	Vema Channel
VMADCP	Vessel Mounted Acoustic Doppler Current Profiler
VSP	Vertical Shear Production
WOA	World Ocean Atlas

Contents

1 Introduction

This thesis investigates the circulation pattern in the Cruzeiro do Sul Rift (CSR) and its surroundings, as well as identifies the phenomena related to its variability in the Rio Grande Rise (RGR). In the following sections, we review the literature about the RGR topography and the large scale circulation around it, describe the thesis motivation, formulate the scientific questions to be answered and present the objectives through which we achieve our goal.

1.1 The Rio Grande Rise

The Rio Grande Elevation (RGR) is an aseismic oceanic elevation with an approximately circular shape in the South Atlantic Ocean, more precisely in the southwestern portion between 28°S - 35°S and 29°W - 39°W (Figure 1.1). It is located approximately 1000 km eastward of the Brazilian coast. It is considered to be the largest plateau in the South Atlantic, having approximately 3,000 km^2. The feature extends from 5000 m to approximately 500 m deep (Camboa & Rabinowitz, 1984; Benites et al., 2020). Regarding the origin of the RGR, the most accepted hypotheses are (i) a stationary hot spot or (ii) a continental fragment remaining from the Atlantic opening (Camboa & Rabinowitz, 1984). Recently, the second hypothesis has gained more support with the discovery of granite rocks at its site (Santos et al., 2019).

The RGR is cut by a fracture zone oriented in the southeast-northwest direction. Also RGR can be divided into RGR West and RGR East (Figure 1.1), where the first has a more elliptical shape, while the second has a rectangular shape oriented in the north-south direction (Cavalcanti et al., 2015). The RGR West, which from now on we'll just call it RGR, is cut by a fault called Cruzeiro do Sul Rift (CSR) which is about 30 km wide and over 2 km deep (Praxedes et al., 2019). We would like to emphasize that the CSR is deeper in the southern portion, while in the northern portion it is shallower, as seen in Figure 1.2.

Despite the efforts, very little is known about the dynamics and spatial-temporal variability of the circulation in the RGR. The only work focused on characterizing the circulation in the RGR on a local scale is Harlamov et al. (2015), who found velocity values at the top of the

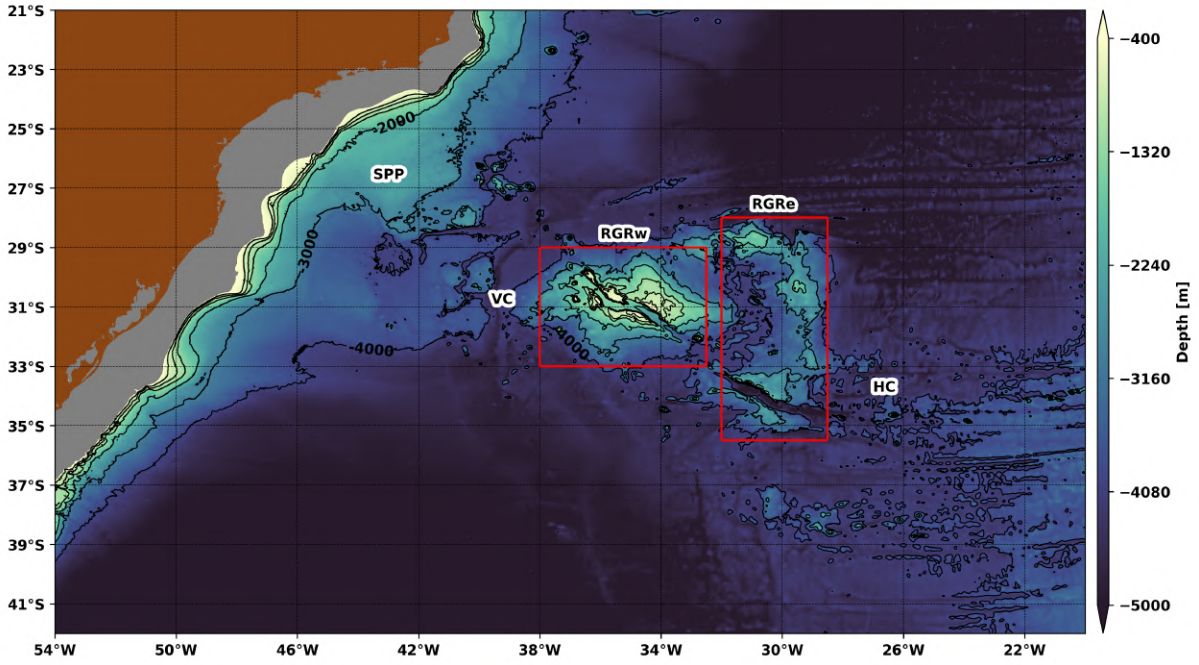

Figure 1.1: Southwest Atlantic Ocean bathymetric map. The map highlights the main topographical features: São Paulo Plateau (SPP), Vema Channel (VC), Hunter Channel (HC) and marked by the red rectangles the Rio Grande Elevation (RGR) that can be divided into RGR West (RGRw) and RGR East (RGRe). The Cruzeiro do Sul Rift cuts the entire RGR in the northwest-southeast direction.Bathymetry data obtained from GEneral Bathymetric Chart of the Oceans (GEBCO) (GEBCO Bathymetric Compilation Group 2021, 2021).

RGR on the order of 0.1 m s^{-1}, which can reach peaks of 0.5 m s^{-1}, varying mainly due to tidal effects. They found a set of undulations in the sediment, including within the CSR, which suggests the presence of intense currents. According to Yeo et al. (2019), currents more intense than 0.2 m s^{-1} may be able to erode the surface of Fe-Mn crusts.

Later, Lisniowski et al. (2017) described the sediment wave fields, observed in Figure 1.3. These fields can extend over zones of up to 30 km and are between 1.2 m - 2.9 m in height with 250 m - 550 m in wavelength and have most of the crests oriented towards the east-west, parallel to CSR. The authors suggest that the breaking of internal waves are responsible for generating intense currents in the CSR and its surroundings, transporting sediment that gives rise to the sediment wave fields.

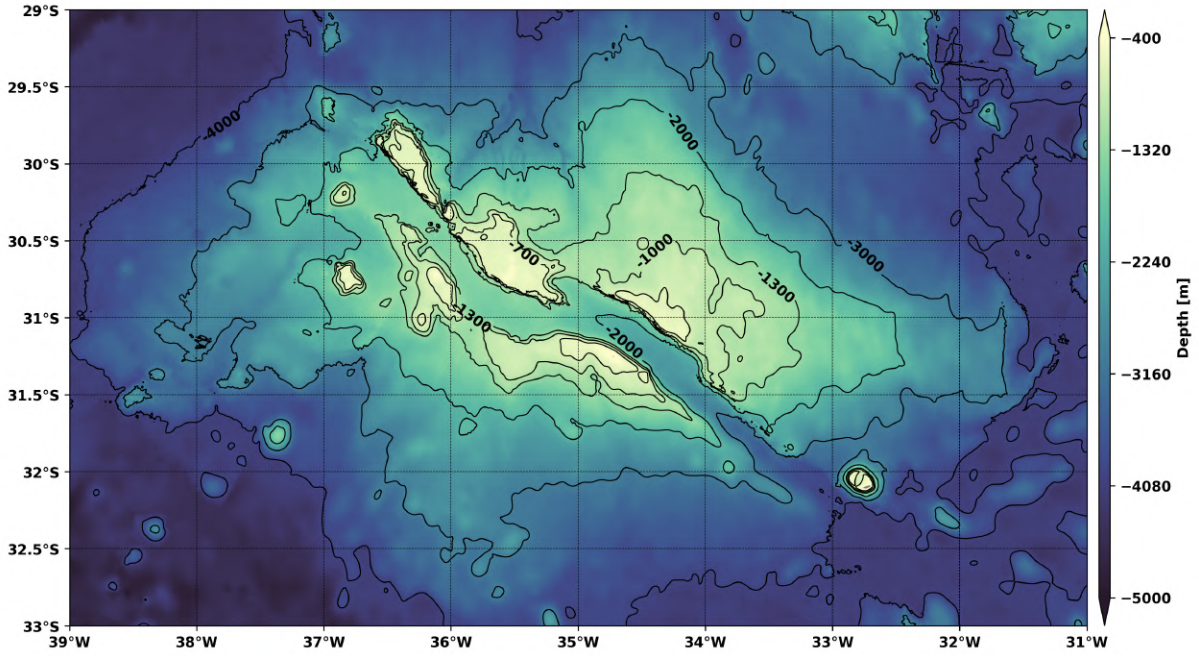

Figure 1.2: Bathymetric map of the RGR. The map highlights the CSR cutting the feature, as well as, the topographic gradient along the CSR. Bathymetry data obtained from GEBCO (GEBCO Bathymetric Compilation Group 2021, 2021).

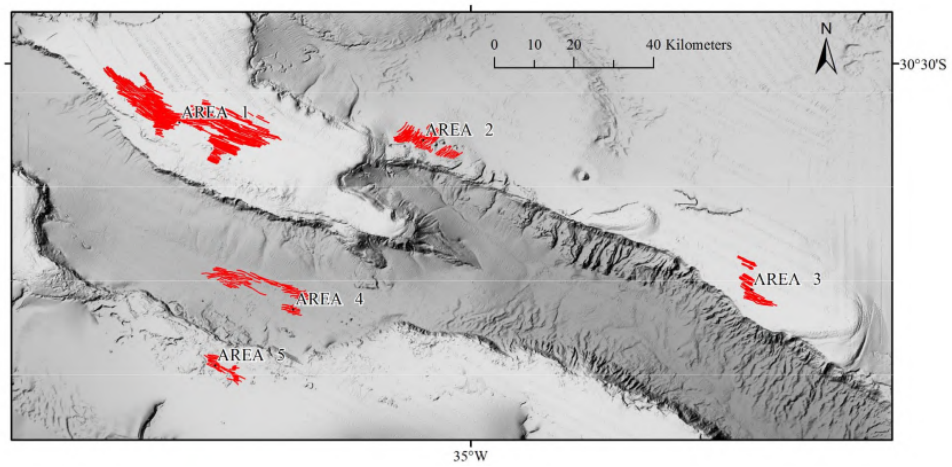

Figure 1.3: Bathymetric map of the RGR. The red fields highlight the five identified sediment wave fields. Extracted from Lisniowski et al. (2017).

The RGR has a diverse environment that is composed of different bottom substrates (Figure 1.4). The classification made by Lisniowski (2020) in partnership with the *Companhia de*

Pesquisa de Recursos Minerais (CPRM) is composed of six classes, namely: deep muddy basins, Fe-Mn crusted plates, foraminiferous sands, fragmented rocks between sediments, carbonatic plates and/or dunes, and sloping outcrops and walls. The Fe-Mn crusted plates were observed up to 1500 m in depth. Also, polymetallic nodules are present in areas classified as fragmented rocks between sediments and sloping outcrops and walls. Interesting to note that the bottom of the CSR works as a large ditch where basically foraminifera sand is accumulated.

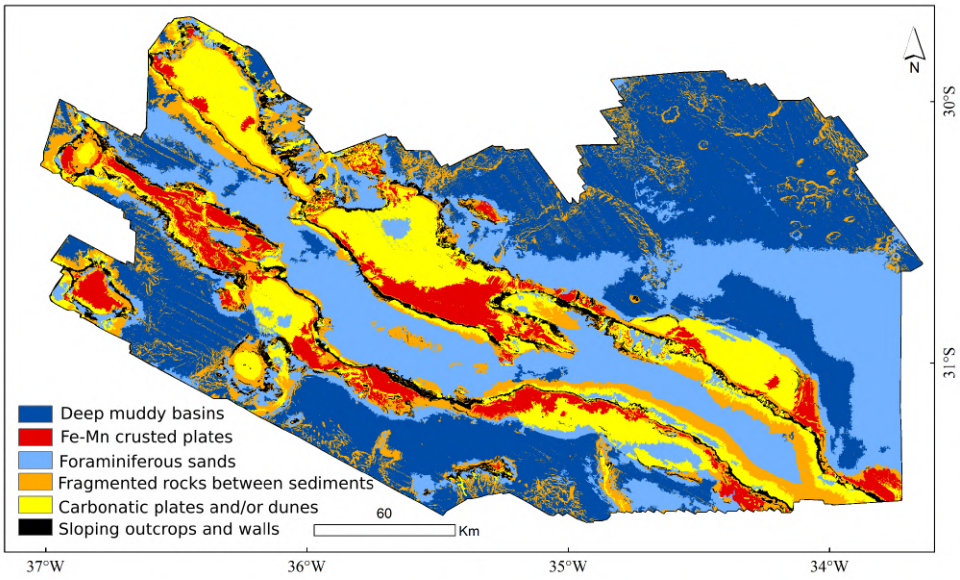

Figure 1.4: Classification map of the bottom substrates in the RGR. Extracted and adapted from Lisniowski (2020).

Due to the potential for mining polymetallic crusts, there is a greater political and economic interest in the region, related to the presence of crusts rich in rare metals such as Co, Ni, Mn, Mo, Th, Ti among others, which are essential for the industry of high technology (Hein et al., 2013; Montserrat et al., 2019). This interest led to the promotion of several scientific projects to study the region, such as the FAPESP–NERC Thematic Project "Marine ferromanganese deposits: a major resource of E-tech elements (Process 2014/50820-7), which made possible the acquisition of the data used for the development of this thesis. Details of the project can be obtained from Jovane et al. (2019).

1.2 The southern branch of the South Equatorial Current

The South Equatorial Current (SEC) is historically acknowledged to be split in three main branches, being at the surface the SEC northern branch (∼2°S), the SEC central branch (∼5°S), and the southern SEC branch (SSEC; ∼15°S) (Peterson & Stramma, 1991). Stramma (1991) suggested that just the SSEC branch bifurcates when it hits the Brazilian continental margin. The predictions made by Stramma (1991) was only confirmed later by Stramma & England (1999) and Rodrigues et al. (2007), who showed that in the annual mean the surface SSEC bifurcates around 14°S and is responsible for closing the South Atlantic Subtropical Gyre.

According to Stramma & England (1999) the SSEC bifurcation are in fact a multi-layer bifurcation system: the surface layer bifurcation occurs about 14°S (0–100 m), the pycnoclinic layer bifurcation happens close to 20°S (100–500 m), and in the intermediate layer, the bifurcation are present about 25°S (500–1200 m). Stramma & England (1999), Boebel et al. (1999) and Núñez-Riboni et al. (2005) showed the presence of the Subtropical Gyre in the intermediate layer occurring approximately between 23°S and 46°S. The eastward flow happens between 33°S and 46°S, and the westward branch lies between 22°S and 32°S, in the RGR domain. Almost at the same latitude interval that is an intense eddy corridor to the west, presented by Garzoli & Matano (2011) between 26°S and 34°S.

More recently, Luko et al. (2021) showed using altimetry and a set of four reanalyses– three of them being eddy-permitting (0.25°× 0.25° horizontal resolution), and one are eddy-resolving (0.083°× 0.083° horizontal resolution) – that the SSEC itself is a multi-band jet. Indeed, the SSEC consists of six branches: 11°S, 14°S, 18°S, 21°S, 26°S, and 30°S (Figure 1.5). Of all branches, only the 26°S and the 30°S branches are extend down to the intermediate layer. After the 30°S branch hits the RGR about 30°W, it split in two branches. The northern band gives origin to the Intemediate Western Boundary Current (IWBC) (Boebel et al., 1999; Silveira et al., 2004; Legeais et al., 2013), while the southern band are responsible for increasing the Brazil Current (BC) transport. On the other hand, the 26°S branch hits the Brazilian continental margin and turns northward increasing the IWBC transport, corroborating Boebel et al. (1999) and Legeais et al. (2013) showing that the Santos Bifurcation, that gives origin to the IWBC, occurs between

26°S e 30°S.

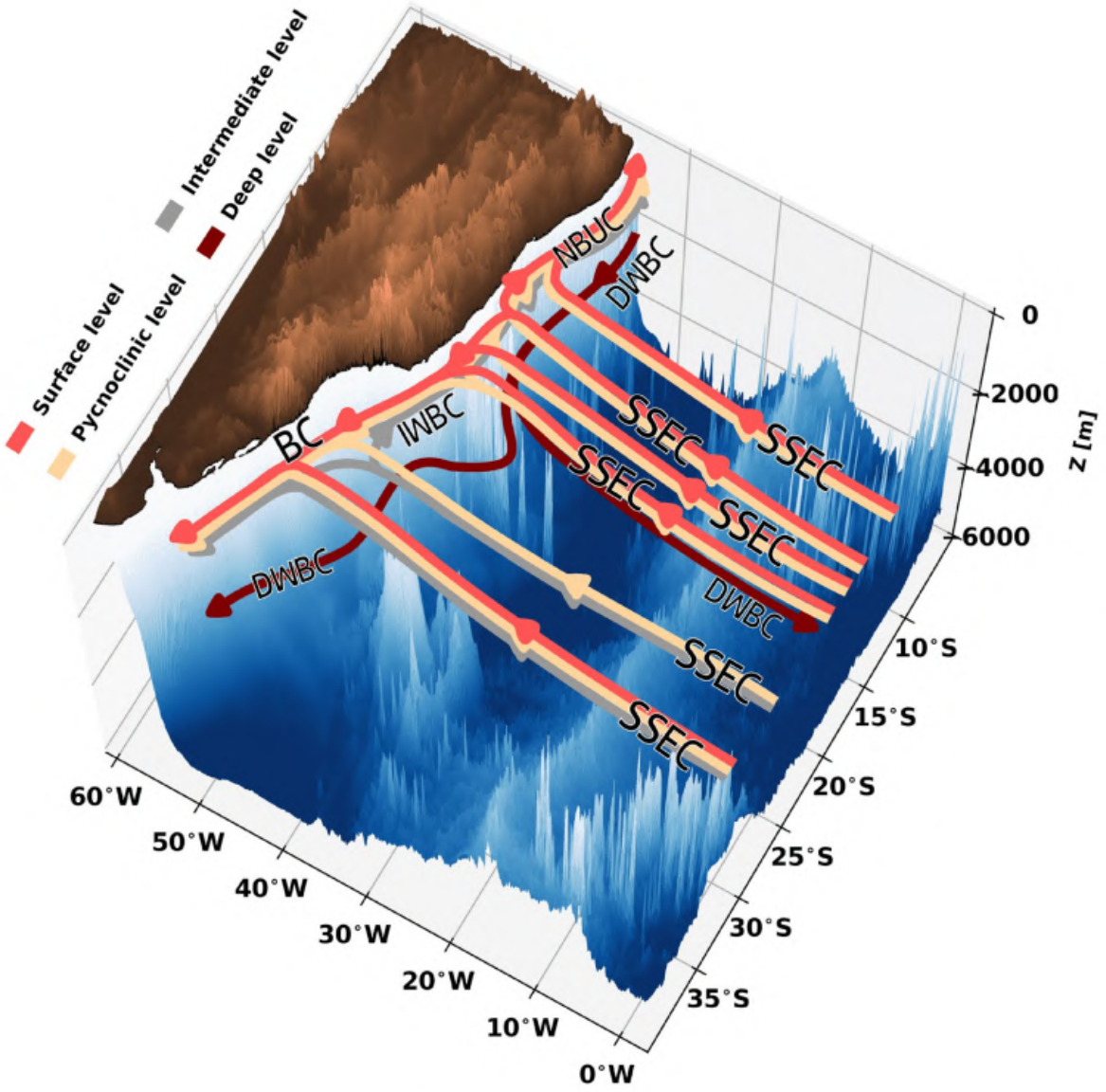

Figure 1.5: Multi-bands SSEC pathway scheme throughout the South Atlantic. DWBC: Deep Western Boundary Current. NBUC: Noth Brazil Undercurrent. Extracted from Luko et al. (2021).

1.3 Motivation

Hydrodynamics within submerged canyons is still an intense object of investigation by the scientific community due to its implications in other major areas of Oceanography, in addition to Physical Oceanography, such as in the larval dispersion patterns (Vic et al., 2018). The RGR is located in the Southwest Atlantic and, given the complexity of the environment and the scarcity of local information, it is critical to characterize the processes that occur there and shape it geomorphologically. In addition, we have the proximity to the Brazilian Exclusive Economic Zone and the presence of Fe-Mn crusts above the RGR plateau. The latter arouses political and economic interest in the region given the great value that this material has for high-tech industries (Hein et al., 2013; Montserrat et al., 2019).

Since 2015, Brazil has the exclusive right to explore crusts on RGR for 15 years. Furthermore, new evidence suggests that the rocks in the region have characteristics of the continental crust (Santos et al., 2019), thus, they would belong to Brazil, which in the future could lead to the further expansion of the Brazilian Exclusive Economic Zone (Silva, 2021). Consequently, there is growing incentive for scientific research aimed at a better RGR characterization in order to keep Brazil active in the region.

Despite the great effort employed to characterize the RGR region, the local circulation is practically unknown when compared to the geophysical and geological knowledge of the region. To understand the sediment motion over the RGR, we must identify which dynamics is responsible for allowing the exposure of the Fe-Mn crust plates. We need to understand the local currents and how they vary spatially and temporally.

As the CSR is an integral part of the RGR, cutting the feature from northwest to southeast, and there is the presence of SSEC's 30°S band impinging at the RGR, we should have a unique hydrodynamics in the region. Thus, throughout this thesis, we will seek to raise information that until now were mostly restricted in space and time, and at qualitative sense in the literature. The local dynamics needs more studies of a better understanding of the circulation in the RGR, more specifically, the circulation within the CSR.

1.4 Scientific Hypotheses and Questions

Given the scarcity of information on circulation in the RGR and its surroundings, that is the absence of studies with a regional spatial and temporal coverage of the area. The same is true for more localized studies, those with a higher spatial and temporal resolution. There are no studies about the mean circulation surrounding and over the CSR either. The only results suggesting possible events occurring within the CSR and its vicinities are those of Harlamov et al. (2015) and Lisniowski et al. (2017). These suggest the presence of internal waves at the site. In addition, we have the presence of a larger-scale forcing given by the SSEC that interacts with the RGR (Luko et al., 2021). From the available information regarding circulation in the region, we can make certain hypotheses that will guide the work hereafter. The presence of the SSEC branch invites us to speculate whether it is responsible for forcing circulation within the CSR since this feature is east-west oriented. Furthermore, we also speculate whether the amplitude of the internal tides would be large enough to modify the mean flow present at the site, thus playing an important role in controlling sediment deposition.

Moreover, we formulate the main hypothesis of this thesis as:

- **The circulation inside the CSR is not stationary, being the principal causes of the variability: internal waves at the tidal frequency, and the SSEC.**

Based on the main hypothesis, we created two secondary hypotheses to understand the possible consequences linked to each of the main causes of CSR variability. The first secondary hypothesis is related to the internal tides, which, given their distribution over the RGR, may be responsible for the sediment distribution pattern, thus providing the outcropping of Fe-Mn crusts. The second secondary hypothesis is related to the possible entry of SSEC into the CSR. Depending on how this occurs, it may generate a series of perturbations within the rift. These perturbations would arise from the direct interaction of the current with the CSR slopes. Thus, the two secondary hypotheses are:

- **Internal tides control sediment deposition in the RGR.**
- **The impinging of the SSEC generates perturbations in the mean flow within the CSR limits.**

To evaluate these hypotheses, we have developed some scientific questions that we should answer throughout this study. They are the following:

- How is the mean flow within the CSR?
- How is the distribution of the internal tides inside the CSR?
- If SSEC enters the CSR, how is it responsible for modifying the flow?
- How the mean flow and the internal waves near the bottom can control the sediment distribution and exposure of Fe-Mn crusts?

1.5 Objectives

General

The central objective of this thesis is to characterize the mean circulation patterns within the CSR and identify the phenomena associated with their variability.

Specific objectives

- Characterize the distribution of internal tides;
- Understand the role of SSEC in the CSR dynamics; and
- Understand the circulation over the bottom.

2 Datasets

To achieve our objectives, we use *in-situ* data obtained by the Marine E-Tech project (Jovane et al., 2019) on board the R/V Alpha Crucis vessel. Also, we make use of regional numerical modeling to achieve a greater spatial and temporal coverage, coupled with a greater spatial and temporal resolution. Together, this set of information allows us to evaluate and understand the dynamics in the RGR domain. Therefore, we seek to enable a considerable advance in the understanding of the region dynamics.

2.1 Observations

The *in-situ* dataset has two vertical transects of Conductivity, Temperature, Depth and Oxigen (CTD-O; Sea-Bird Electronics 9 plus) and Lowered Acoustic Doppler Current Profiler (LADCP; WorkHorse 300 kHz from Teledyne RDI), one parallel and one perpendicular to CSR that extend from the surface to the bottom (Figure 2.1). The dataset also consists of Vessel Mounted Acoustic Doppler Current Profiler (VMADCP; Ocean Surveyor 75 kHz from Teledyne RDI) profiles along the ship route, which can be used to estimate velocities up to approximately 400 m depth.

In addition to the hydrographic data, we have a mooring line located at 31.172°S and 34.748°W, placed at the CSR slope, having a duration of approximately one year and two months, ranging from 04/02/2018 to 12/04/2019, with a temporal resolution of 20 minutes. The mooring consists of two Teledyne RDI WorkHorse 300-kHz ADCPs pointed in opposite directions with approximately 2 m vertical resolution. The ADCPs were approximately 20 m from the bottom, which was at 1250 m (Figure 2.2).

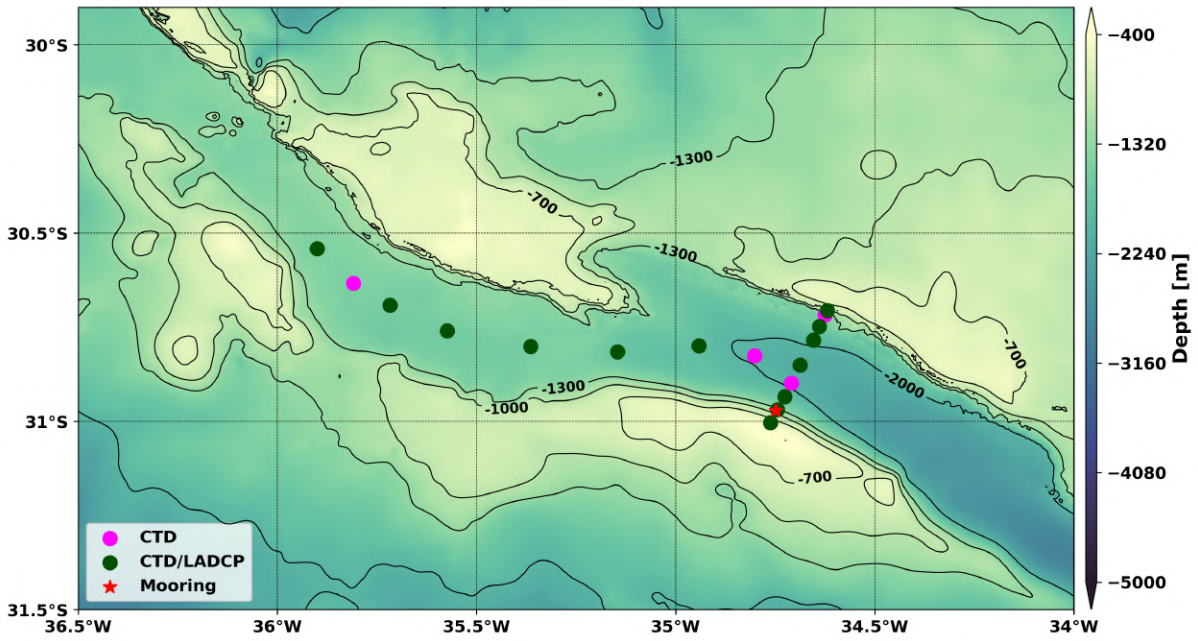

Figure 2.1: ERG map with the position of the oceanographic stations and Marine E-Tech Mooring. The green stations have CTD/LADCP data, the red ones have only CTD and the yellow star represents the location of the mooring line.

2.1.1 Data Processing

CTD-O Data

The CTD-O profiles were processed following these steps (Thomson & Emery, 2014):

- *Loop Edit*: Excludes spurious data resulting from abrupt changes in the pressure sensor.
- *Despike*: Excludes spurious data that exceeds two standard deviations from the 101-sample moving window.
- *Binning*: Averages the data for regular 1 m intervals.

VADCP Data

The VMADCP data were processed using the Common Ocean Data Access System (CODAS) program, developed by the University of Hawaii. The program reads the raw data and combines

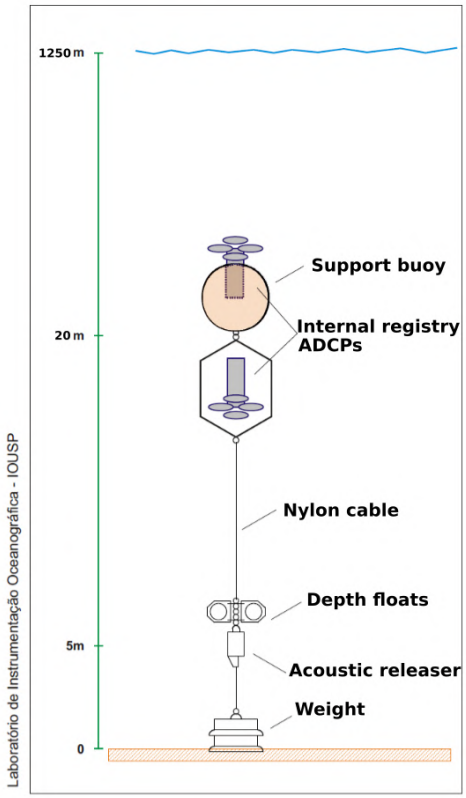

Figure 2.2: Scheme of the mooring line placed at the south slope of the CSR, at the 1250 m isobath, exhibiting two 300-kHz ADCPs pointed in opposite directions.

it with auxiliary ship measurements such as position, ship speed, heading, pitch, and roll to correct the raw data and obtain the ocean speed. In the last processing step, parameters such as percent good and signal magnitude eliminate spurious data.

LADCP Data

The LADCP data were processed using the LDEO IX program (Thurnherr, 2018). The LADCP processing uses both the CTD data and the VMADCP data. The LADCP processing uses the Vessel's GPS information to increase the accuracy of the velocity data. This information allows a better estimation of the barotropic flow component and magnetic declination calculation.

Mooring Data

The ADCPs from the mooring had the tilt variations of the equipment as pitch and roll corrected internally by the equipment. The Integrated Marine Observing System (IMOS) program, developed by the Australian Ocean Data Network (AODN) to process instruments attached to oceanographic moorings, allowed the data quality control. Empirical orthogonal functions (EOFs) filled the information gaps along with the time series. This method does not alter the time series statistics (Beckers & Rixen, 2003). The same method was employed by Rocha et al. (2014) and Simoes-Sousa et al. (2021).

2.2 Circulation Model Setup

The high-resolution realistic simulation of the RGR circulation are built with the Coastal and Regional Ocean COmmunity model (CROCO; Jullien et al., 2019). The CROCO is a model constructed over the Regional Ocean Model System - Adaptative Mesh Refinement In Fortran (ROMS-AGRIF; Shchepetkin & McWilliams, 2005). The simulation is carried out under the hydrostatic approximation and solves the primitive equations in an Earth-centered rotating environment for the potential temperature, salinity, and velocity. CROCO has terrain-following coordinates, this configuration allows us to solve the dynamics in all domain using the same amount of vertical levels that adjust to the local topography, a better feature since we model a region with large topographic gradients.

The numerical domain covers the area between 24°W and 44°W in longitude, and 24°S and 38°S in latitude, with the RGR in the center of the domain (Figure 2.3a). The model's horizontal resolution is 1/50°, approximately 1.8 km. In turn, the model has 30 vertical levels refined near the surface and the seafloor with the following parameters of stretching: $\theta_s = 6$ and $\theta_b = 4$ (Figure 2.3b).

CROCO is a split-explicit free-surface ocean model, 3rd-order time-stepping. The salinity, temperature, and baroclinic momentum advance with a long time-step of 108 s. While the barotropic momentum and surface elevation advance with a small time-step of 4 s, to respect the maximum Courant–Friedrichs–Lewy (CFL) number allowed in our configuration.

The model horizontal momentum advection discretization is a 5th-order upwind scheme. It

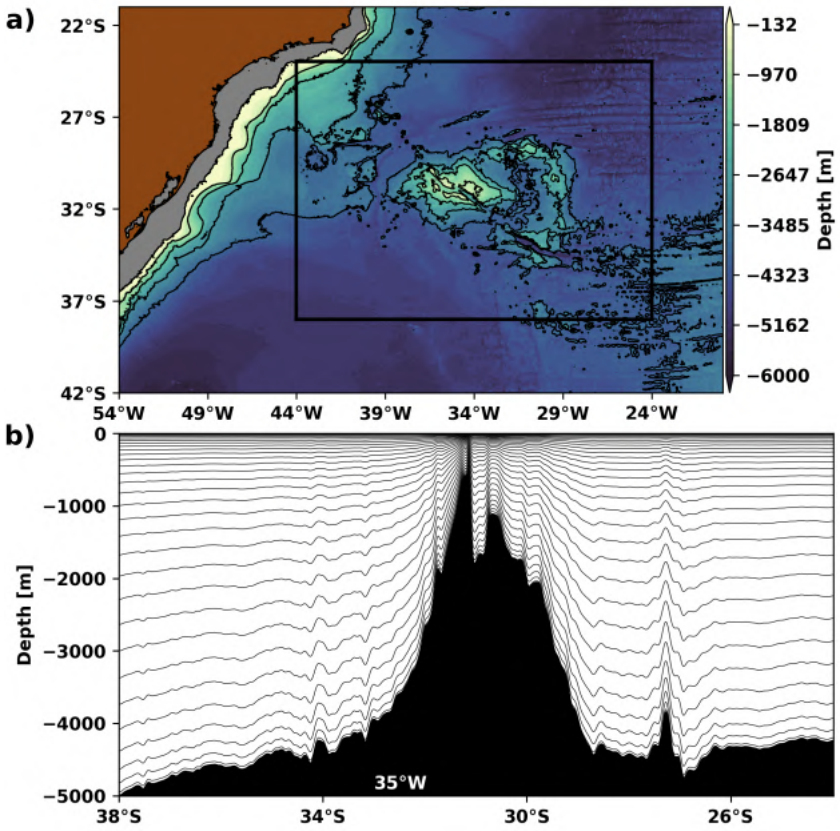

Figure 2.3: Domain setup. a) The black rectangle demarks the model horizontal domain, which covers the area between 24°W and 44°W in longitude, and 24°S and 38°S in latitude. b) Section at 35°W showing the 30 vertical levels distribution. The RGR is present in the center of both images.

allows the formation of steep gradients, improving the solution's effective resolution (Shchepetkin & McWilliams, 1998; Soufflet et al., 2016), reducing spurious diapycnal mixing (Soufflet et al., 2016). Explicit lateral viscosity is not necessary to reduce numerical dispersion errors in this case since upwind advection schemes have implicit diffusion (Jullien et al., 2019).

Analogous to the horizontal momentum advection, horizontal tracers advection uses a 5th-order upwind scheme. However, it has a configuration where the diffusion part of the scheme is rotated along isopycnal surfaces to avoid spurious diapycnal mixing and loss of water masses (Marchesiello et al., 2009; Lemarié et al., 2012). Also, a highly accurate pressure gradient scheme constrains errors frequently related to terrain-following coordinate models (Shchepetkin & McWilliams, 2003).

The simulation vertical momentum advection is a 4th-order compact advection scheme. It has the benefit of being unconditionally stable, preserving a good accuracy in areas with small Courant numbers (Shchepetkin, 2015). The model vertical tracers advection discretization is a 4th-order centered advection scheme with harmonic averaging, which permits a more accurate result (Jullien et al., 2019). CROCO parametrizes the vertical mixing using the K-Profile Parametrization (KPP; Large et al., 1994).

Bathymetry for all domain is constructed from the GEBCO 2021 (GEBCO Bathymetric Compilation Group 2021, 2021), avaiable at `https://www.gebco.net/data_and_products/gridded_bathymetry_data/`, it is a global terrain model for ocean and land, providing elevation data, in meters, on a 15 arc-second interval grid.

A Hanning smoothing kernel with 4 bathymetry grid points spacing is used to prevent aliasing on any occasion that the bathymetry data has higher resolution than the model grid and to ensure the bathymetry smoothness at the grid horizontal resolution scale. Terrain-following models like CROCO have computational constrains with respect to the roughness and steepness of the bathymetry (Beckmann & Haidvogel, 1993). According to Beckmann & Haidvogel (1993), to prevent horizontal pressure gradient errors, present in terrain-following coordinate models, the model bathymetry requires that the steepness of the topography,

$$r = \frac{h_i - h_{i-1}}{h_i + h_{i-1}}, \tag{2.1}$$

does not exceed $r_{max} = 0.2$. Here, h is the bathymetry height at a grid point. In our domain, the maximum value of r is 0.19, and in the RGR domain of interest of this study, it reaches 0.15 (Figure 2.4).

Data from GLORYS12V1 reanalysis from Mercator Ocean (France) are prescribed at the boundaries using a one-way nesting approach. Also, it is used as the initial condition. GLORYS12V1 is a daily eddy-resolving reanalysis that runs on the Nucleus for European Modelling of the Ocean - Ocean General Circulation Model (NEMO-OGCM) using a 1/12° horizontal resolution and 50 vertical levels (Fernandez & Lellouche, 2018). The reanalysis is available at Copernicus Marine Environment Monitoring Service (CMEMS), and their descriptions are in Fernandez & Lellouche (2018), Gounou et al. (2019) and CMEMS (2021). GLORYS12V1 was one of the reanalysis used by Luko et al. (2021) to evaluate the SSEC branches.

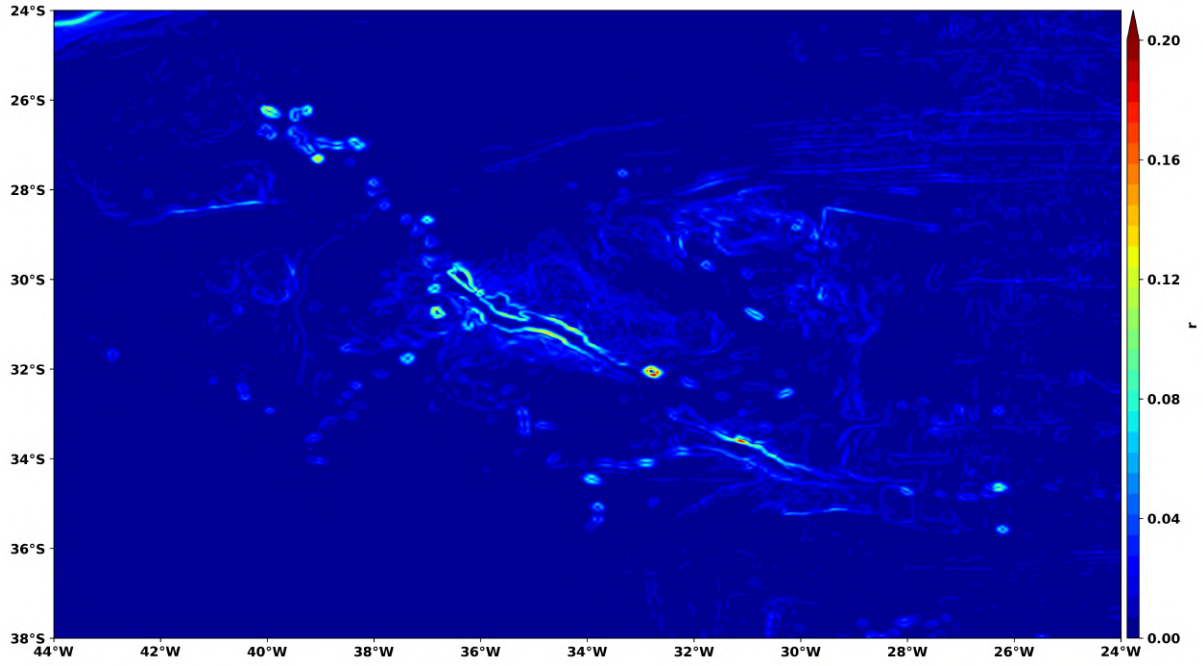

Figure 2.4: Topography steepness (r) calculated following equation 2.1 (Beckmann & Haidvogel, 1993).

ERA5 atmospheric reanalysis at the surface (Hersbach et al., 2018) forces the model. ERA5 provides hourly estimates of a large number of atmospheric variables, such as Downward longwave radiation flux, downward shortwave radiation flux, upward shortwave radiation flux, upward longwave radiation flux, precipitation rate, specific humidity, temperature, and velocity. These variables force the model. The data cover the Earth on a 30 km grid and resolve the atmosphere using 137 levels from the surface up to a height of 80 km.

At the model boundaries, we prescribe tidal elevation and barotropic currents from a global inverse barotropic tidal model (TPXO7; Egbert & Erofeeva, 2002) and consist of 10 frequencies: M2, S2, N2, K2, K1, O1, P1, Q1, Mf and Mm.

The model was run from January 1 2015 to December 31 2019. During the first year the model spin-up and during 2016/2017 we have the model adjustment to the seasonal cycle. All results discussed in this thesis used the period between 2018 and 2019. The model kinetic energy evolution can be be seem in Figure 2.5.

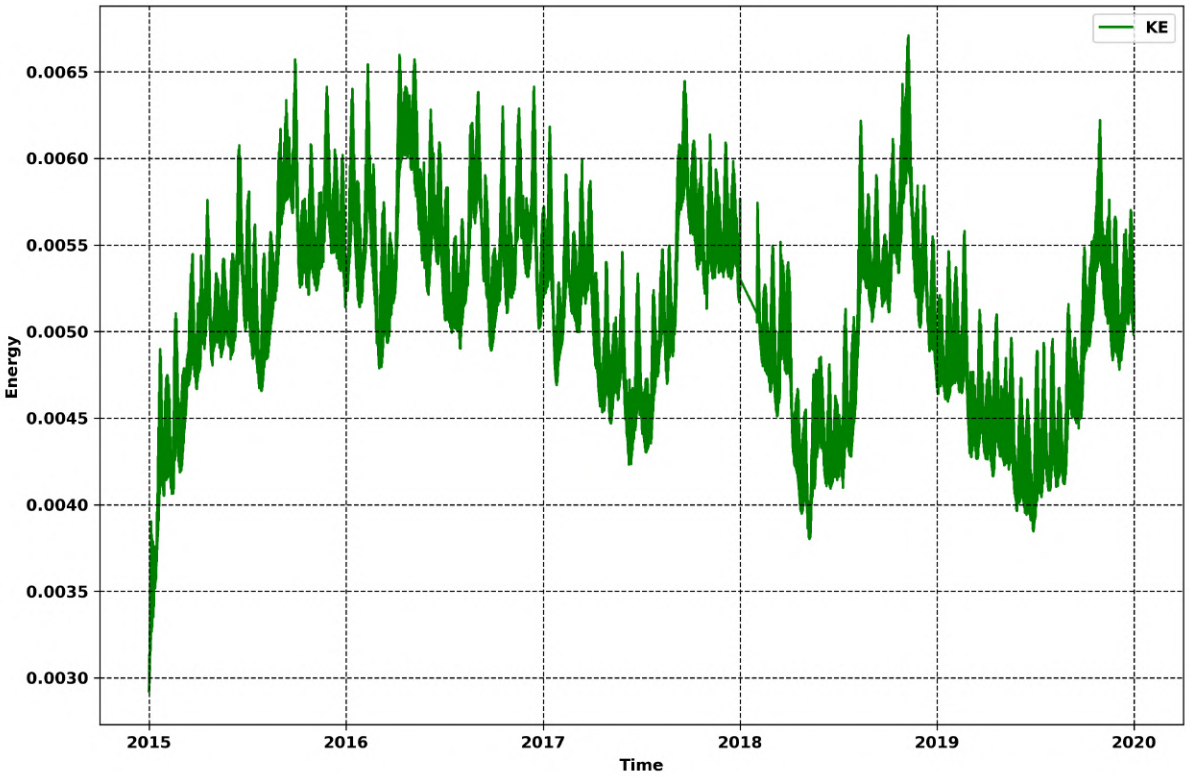

Figure 2.5: Kinetic energy (KE) evolution between 2015 and 2019.

3 Analysis of the Observational Data

3.1 The Marine E-Tech Mooring

The mooring located on the south slope of the CSR revealed several aspects of the variability existing in the approximately 70 m water column above the bottom (1250 m). From the velocity time series (Figure 3.1), the flow within the CSR has continuous velocity direction inversions, which can reach peaks greater than 0.3 m s^{-1} in magnitude. These high-frequency variations mask lower frequency variations, such as the signal observed in October 2018 and February 2019. This signal decrease with the depth increase (Figure 3.4).

Figure 3.2 presents the average velocity profile showing that the mean flow at this position and depth interval is close to zero with a slight eastward trend. However, the 95% confidence interval shows that it presents a high variability. Furthermore, the velocity tends to decrease according to the increase in depth.

Then, we calculate the rotary power spectral density (PSD) for the velocity components to identify the main frequencies responsible for current variability and possible associated phenomena. According to Thomson & Emery (2014), the rotary PSD reveals important aspects of the oscillatory flow. The method has demonstrated particularly valuable for examining flows over steep topography (Xu & Lavelle, 2017) and in many cases, one of the rotary components dominates the currents (Thomson & Emery, 2014). Negative frequencies represent the clockwise spectra and the positive frequencies, the counterclockwise spectra.

Figure 3.3 shows the spectral analysis revealing that the variability of the CSR is intrinsically linked with the clockwise spectrum of the semi-diurnal lunar tidal component (M2) with a period of 12.42 h. Followed, although much less relevant, by the diurnal components (O1) with a period of 25.82 h and by the semi-diurnal (S2) with a period of 12 h. In addition, PSD show that low frequencies processes (periods greater than 36 h) are less relevant in the 10 m layer near the bottom than in the upper portion of the mooring.

We also filtered the time series using a moving average with a 36h window (Figure 3.4), a period approximately 55% longer than the inertial period for the region (23.23 h). By filtering the

time series, it becomes evident that high frequency processes (periods lower than 36h) dominate the CSR dynamics, as the current velocity inversions have decreased, as well as there has been a considerable decrease in velocity magnitude, with most intense velocities reaching 0.1 m s^{-1}. Low frequency processes also present a decrease in magnitude as the bottom approaches.

We evaluate the velocity variance ratio to understand how much of the flow variability is explained by periods longer and shorter than 36 h (Figure 3.5). Figure 3.5 shows that high frequencies are responsible for more than 90% of the variance close to the bottom and approximately 75% at the upper-looking ADCP side of the mooring. Since tides are one of the most important processes responsible for the mooring variability (Figure 3.3), we fit the tides components harmonics using the *ttide* software package (Pawlowicz et al., 2002). The tidal harmonic fit shows that tides explain more than 40% of the variance close to the bottom and approximately 30% in more distant regions. However, periods shorter than 36 h, disregarding the tidal harmonics, explain approximately 50% of the variability in all levels. In regard to the periods higher than 36 h, we observe the increase of the relevance of these frequencies as soon as we get away from the bottom, with the variance explained increasing from 7% to almost 20%. The tidal velocity relevance can be view at Figure 3.6, where the velocity peaks at the total velocity are related with the peaks at the tidal velocity.

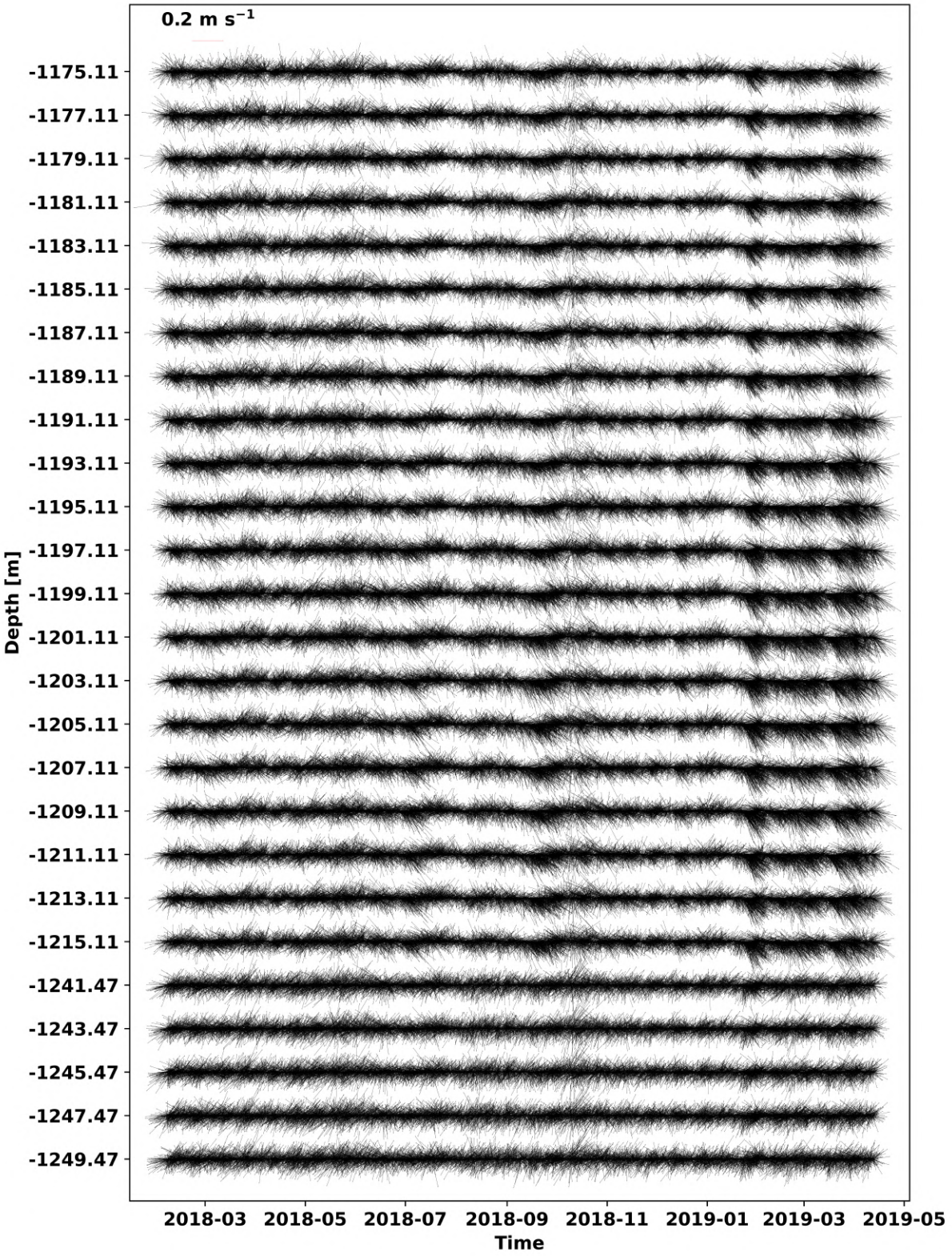

Figure 3.1: Velocity time series for all mooring levels.

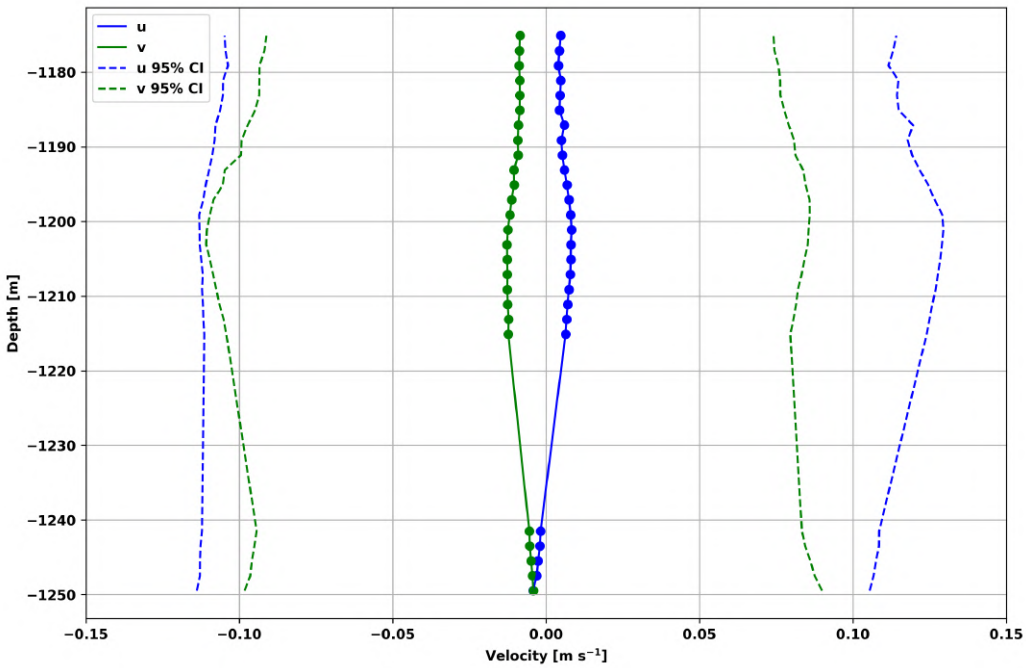

Figure 3.2: Mean velocity profile of the CSR mooring (continuous line with dots, where the dots represent the depths with data) with 95% confidence interval (dashed lines). The blue (green) lines refer to the u (v) velocity component.

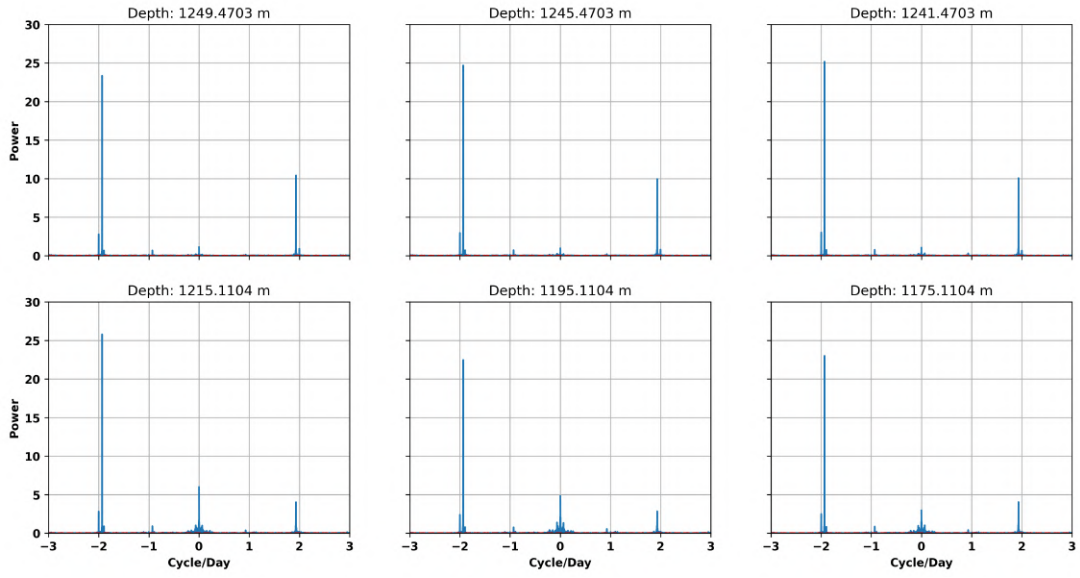

Figure 3.3: PSD of currents measured from 04/02/2018 to 12/04/2019 with 20 minutes resolution, at the depths 1175, 1195, 1215, 1241, 1245 and 1249 m. The horizontal red dashed lines mark the 95% confidence level.

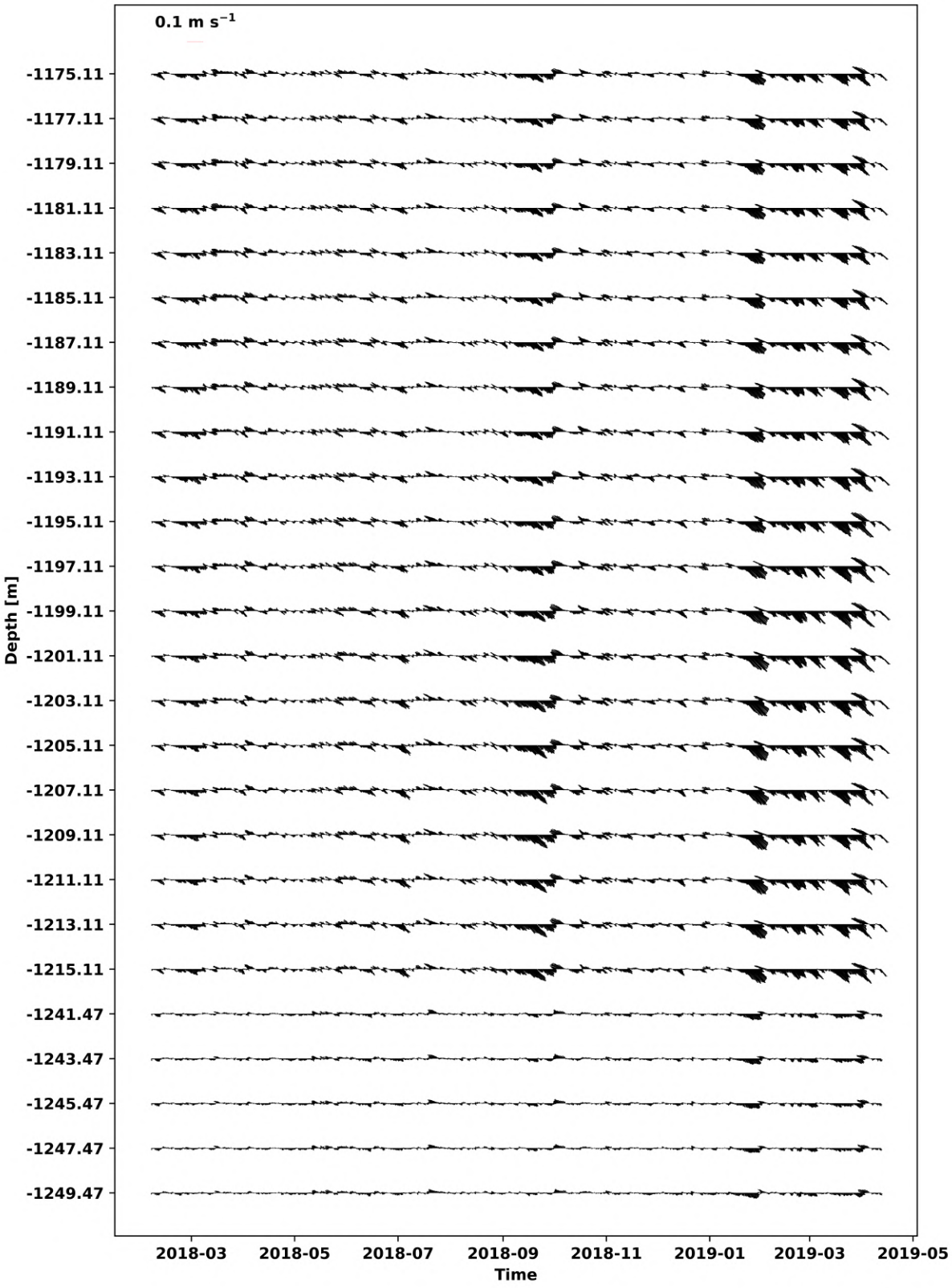

Figure 3.4: 36h filtered velocity time series for all mooring levels.

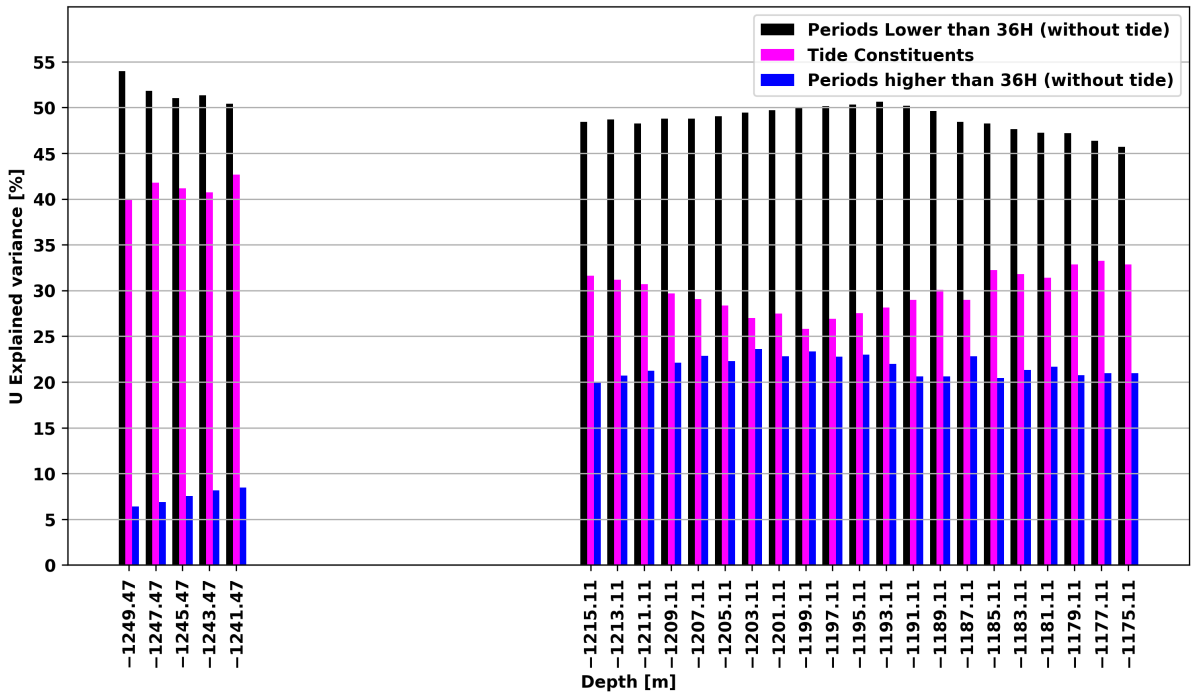

Figure 3.5: Velocity variance ratio for all mooring levels. The magenta bars represents the variance explained by the tidal harmonics. The black (blue) bars represents the variance explained by periods shorter (longer) than 36 h and removing the tidal harmonics.

Figure 3.6: Total velocity (black arrows) and harmonical fit tidal velocity (red arrows) time series for 1245 m.

3.2 Analysis of the hydrographic and LADCP measurements

3.2.1 Water mass distribution

From the CTD data, we evaluate the distribution of water masses at the oceanographic transects. The analysis adopts the neutral density interfaces (γ^n) defined by Valla et al. (2018) for the Southwest Atlantic. The interface between Tropical Water (TW) and the South Atlantic Central Water (SACW) was adapted following the temperature and salinity limits defined by Silveira et al. (2000), which defined that the TW is characterized by temperatures greater than 20°C and salinities above 36 g kg^{-1} off Southeast Brazil. Therefore, the γ^n interfaces were defined as: TW $<$ 25.85 kg m^{-3}, 25.85 kg m^{-3} $<$ SACW $<$ 27.10 kg m^{-3}, 27.10 kg m^{-3} $<$ Antarctic Intermediate Water (AAIW) $<$ 27.60 kg m^{-3} , 27.60 kg m^{-3} $<$ Upper Circumpolar Deep Water (UCDW) $<$ 27.90 kg m^{-3}, and 27.90 kg m^{-3} $<$ North Atlantic Deep Water (NADW) $<$ 28.10 kg m^{-3}.

From Figure 3.7, we observe that the TW is located between the surface and ∼180 m, the SACW between ∼180-630 m, the AAIW between ∼630-1220 m, the UCDW between ∼1220-1730 m, and the NADW below ∼1730 m.

The oxygen distribution along the water column helps to characterize the water masses within the CSR since the Figure 3.7 shows the subsurface oxygen maximum at the AT-ACAS interface, passing to the SACW oxygen minimum, followed in the middle layer by an AAIW oxygen maximum. Below the middle layer of oxygen maximum, there is the UCDW with the minimum water column oxygen concentration. In turn, in the deeper portion the oxygen concentration increases due to the presence of the NADW.

The presence of Fe-Mn crusts in the RGR were observed from the top of the RGR up to 1500 m depth (Lisniowski, 2020). It evidences that the shallow areas are under influence of the lower portion of the SACW, while a larger depth range are under influence of the oxygenated AAIW. The deepest Fe-Mn crusts areas are under effect of the UCDW (Figure 3.7). We also have the confinement of the NADW in the deeper eastern portion of the CSR. Figure 3.7 shows that the CSR valley is under the influence of two types of water masses. The deeper western

portion of the CSR valley is under the domain of the UCDW (Figure 3.7). As the water masses along the CSR valley have distinct oxygen concentrations, we speculate that this change may affect the benthic community.

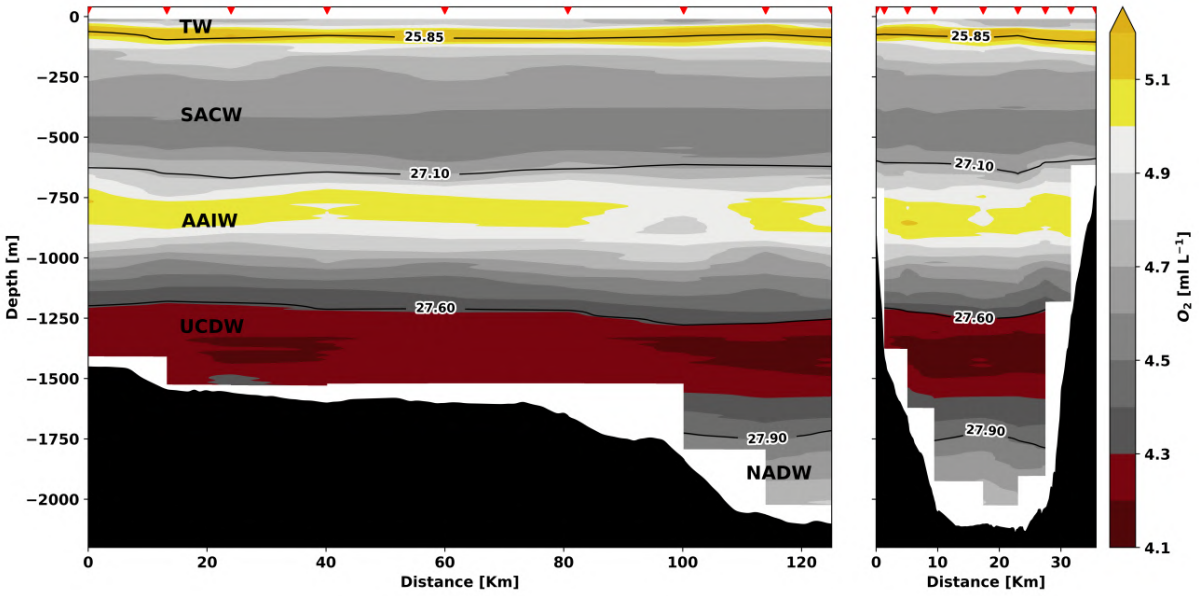

Figure 3.7: Vertical transect of dissolved oxygen with water masses interfaces. Thick black lines indicate water body interfaces in terms of neutral density. Left panel: Section parallel to the CSR edges. Right panel: Section perpendicular to the CSR. Red triangles indicate the positions of oceanographic stations.

3.2.2 Local Deformation Radius and Dynamic Modes

A key quantity to classify the physical nature of the dynamic phenomena is the local deformation radius. For instance, submesoscale phenomena are characterized by length scales smaller than the first baroclinic radius (Rd) (Capet et al., 2008a). The long (or hydrostatic) pressure modes were calculated using the hydrographic data. The linear modes originates from the variables separation in the governing equations (LeBlond & Mysak, 1981), such as:

$$P(x, y, z, t) = P_i(x, y, t)F_i(z), \tag{3.1}$$

where P is a property, P_i are the ith-mode property amplitude and F_i are the ith vertical mode. The QG vertical modes structure is determined by:

$$\frac{\partial}{\partial z}\left(\frac{1}{N^2}\frac{\partial F_i}{\partial z}\right) + \frac{F_i}{(f_0 Rd_i)^2} = 0, \tag{3.2}$$

where f_0 is the inertial frequency, Rd_i is the ith-mode internal deformation radius and N is the stratification frequency. Where $N^2 = \frac{\partial b}{\partial z}$ where $b(z) = \frac{-g\rho(z)}{\rho_0}$, b is the buoyancy, g is the gravitational acceleration, ρ is the density and $\rho_0 = 1025$ kg m^{-3}. At the boundaries it demands top rigid lid and flat bottom, leading to:

$$\frac{\partial F_i}{\partial z} = 0, \text{ at } z = 0 \text{ and } z = -H. \tag{3.3}$$

This problem was solved for each CTD profile in the along-canyon transect. Each N profile was smoothed as observed at the first row in Figure 3.8. In Figure 3.8 second row, we present the structure of the first three vertical modes for each station. The first three local baroclinic deformation radius (Rd_i, i=1,2,3) of each station are presented in Table 3.1. We observe that, with the increase of the water column depth, the Rd_i values also increase. As example, Rd_1 varies between 19.47 km and 26.14 km in the CSR valley.

Table 3.1: Along-canyon transect - Local deformation radius

Station	**H (m)**	Rd_1 **(km)**	Rd_2 **(km)**	Rd_3 **(km)**
1	1407	19.47	11.39	8.13
2	1525	21.58	12.22	8.71
3	1527	21.82	12.19	8.79
4	1570	22.53	13.94	9.28
5	1520	22.34	13.92	9.40
6	1520	21.84	13.75	9.17
7	1793	23.30	13.31	9.96
8	2022	24.50	14.15	10.78
9	2024	26.14	16.96	11.79

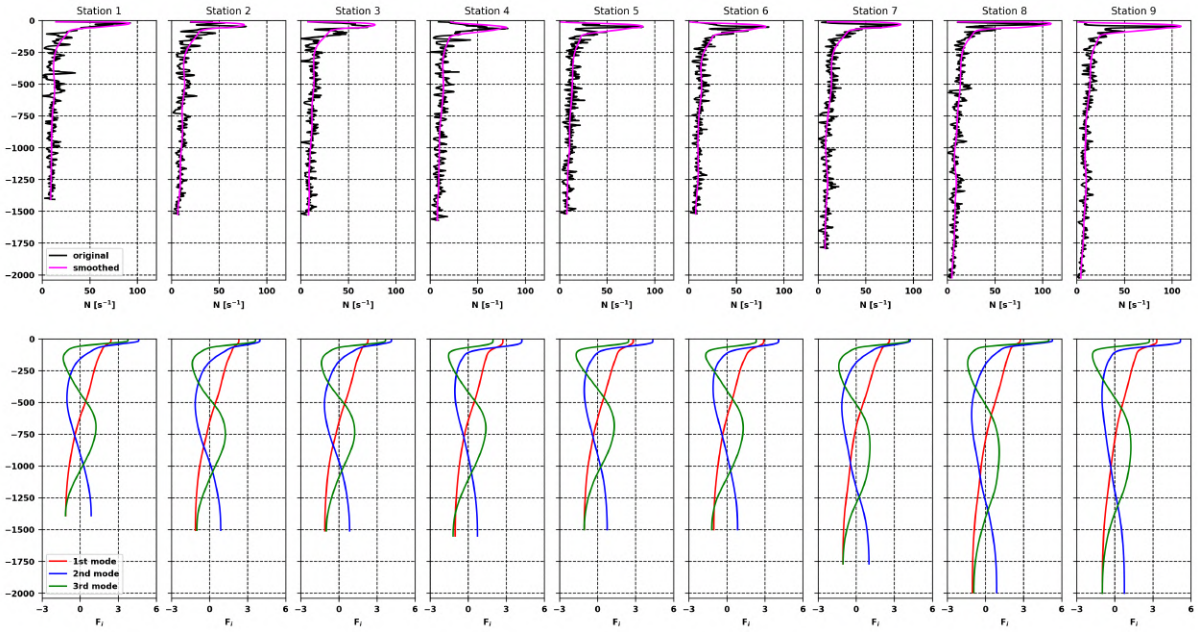

Figure 3.8: Upper row: Stratification profile for each station in the along-canyon transect. The black (magenta) line represents the original (smoothed) data. Lower row: Vertical mode structure for each station in the along-canyon transect. The red, blue and green lines represent the 1st, 2nd and 3rd vertical mode structure respectively.

3.2.3 LADCP velocity field

The LADCP vertical profiles help us to identify some characteristics of the velocity field inside the CSR. One concerning is that the along-canyon transect (Figure 2.1) was occupied in 24 hours, consisting in a frequency of one LADCP station per three hours. Regarding the cross-canyon transect (Figure 2.1), it was occupied in distinct moments. The first portion consists in the southernmost 3 LADCP stations, that was occupied in 2.5 h. The second portion consists in the northernmost 4 LADCP stations that was occupied in 5 h. The time difference between the end of first and the start of the second portion are 11 h. Because of that, we need to state that due to the high variability caused by tides (Figure 3.5), mainly the M2 component (Figure 3.3). This constituent has a period of approximately 12 h and that was observed in the mooring record causing velocity inversions (Figure 3.1). So, we will not consider all the LADCP vertical profiles as being a proper quasi-synoptic data set. For this reason, we opt to present them separately at Figure 3.9 and Figure 3.10.

Figure 3.9 shows the along-canyon velocity while Figure 3.10 shows the cross-canyon velocity. The velocity structure presents a complex circulation pattern with many velocity inversion along the water column. The velocity inside the CSR was able to reach 0.3 m s^{-1}. The left panel in Figure 3.9 shows an intense convergence between two adjacent stations at km 20 and km 40. The left panel in Figure 3.10 shows direction-alternating velocity profiles in the same position, suggesting the existence of an anticyclonic circulation.

A similar anticyclonic feature is observed between 100 km and 130 km. The left panel of Figure 3.10 shows two direction-alternating velocity profiles with 0.25 m s^{-1}. The right panel of Figure 3.10 shows the same intense velocity northward between 500 m and 1200 m inside almost all CSR width. The patterns described are shown and sketched in the Figure 3.11, where we observe both anticyclonic circulations in the along- and cross-canyon transects.

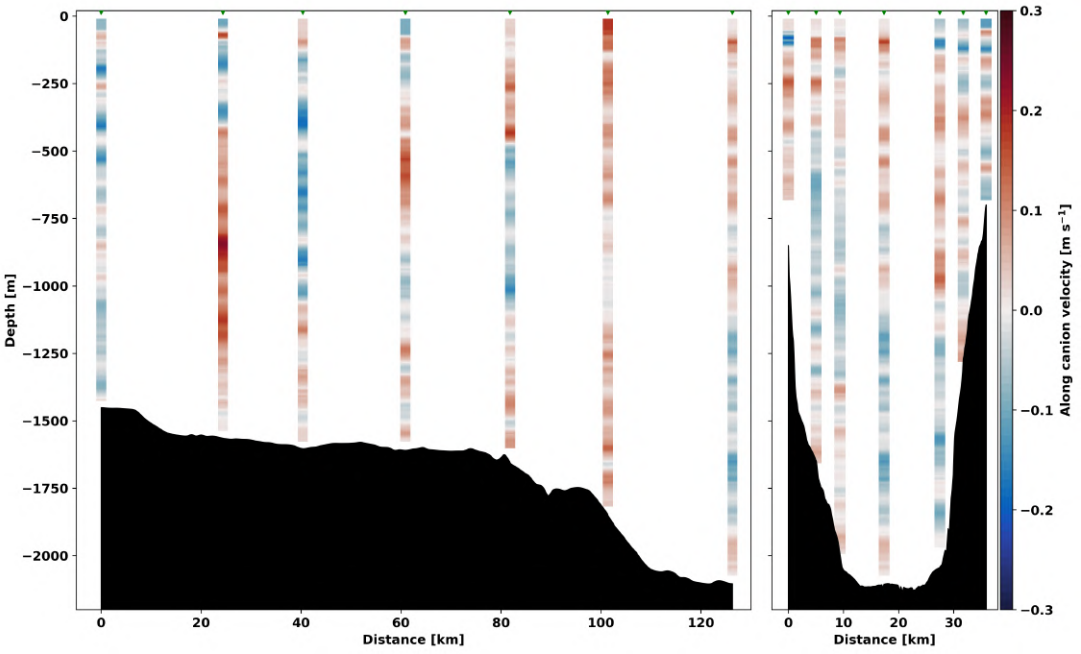

Figure 3.9: along-canyon velocity. Left panel: along-canyon transect. Right panel: cross-canyon transect. The green triangles represents the LADCP stations.

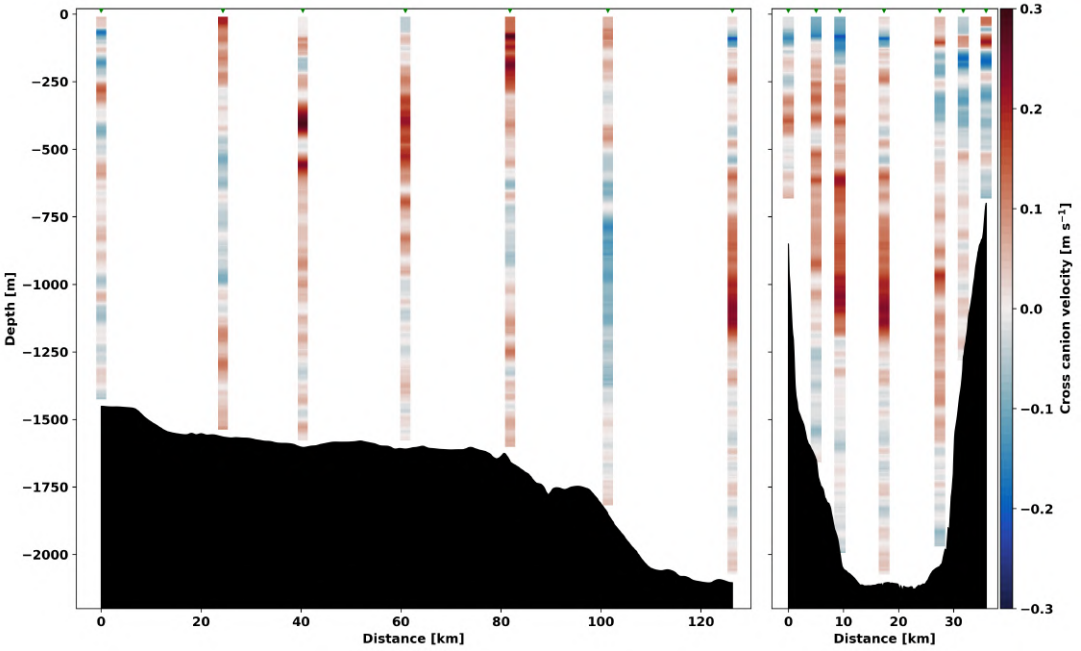

Figure 3.10: cross-canyon velocity. Left panel: along-canyon transect. Right panel: cross-canyon transect. The green triangles represents the LADCP stations.

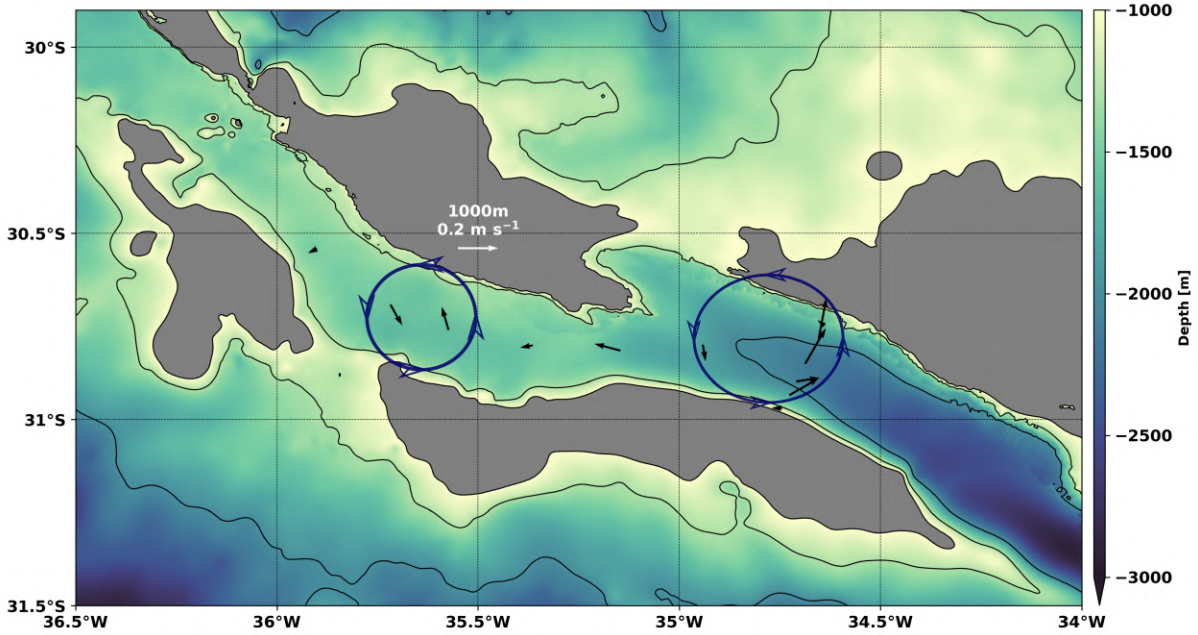

Figure 3.11: LADCP velocity map at 1000 m with a sketch of the anticyclonic circulations.

4 Circulation Model Output Skill Tests

In this work, as described in Chapter 2, we performed our own regional numerical simulations using the CROCO model initialized with a temperature-salinity-velocity field from the GLORYS12V1 reanalysis for 01 January 2015. Prior to the use of the model outputs in dynamical analyses, we need to test the skill of the model to reproduce phenomena in the simulation that are already known and which occur in the study area. The circulation model was run for five years (2015-2019) as described in section 2.2, the last two years corresponds to the interval where the energy enters in the equilibrium (Figure 2.5). We attest the usability of this period when we compare the model output with the mooring data, as well as with the World Ocean Atlas (WOA) 2018 Dataset (Locarnini et al., 2018; Zweng et al., 2019).

4.1 Skill Test with the WOA-2018

To test the skill of the model mean hydrographic field, we compare it with an independent database, the WOA 2018 (Locarnini et al., 2018; Zweng et al., 2019) climatological mean field from 1955 to 2017 with a horizontal resolution of 1/4°. We use the temperature and salinity data to conduct the skill test.

We construct surface-bottom transects in the meridional and zonal directions (Figure 4.1) using the temperature data. The zonal temperature transect located at 30°S between 42°W and 26°W for the CROCO model output (Figure 4.1 upper left panel) and the WOA data (Figure 4.1 upper right panel) shows a good similarity between the two transects with a normalized root mean square error of 0.035. In these transects, the isotherms are located at the same depth range at the surface and the bottom, regards the data and bathymetry differences. The major difference appears west of RGR between 36°W and 42°W around 1500 m, where the WOA transect presents a colder tongue between the 3°C isotherm, while in the model output this tongue is smaller and weaker.

The meridional temperature transect located at 34.5°W between 36°S and 26°S for the CROCO model output (Figure 4.1 lower left panel) and the WOA data (Figure 4.1 lower right

panel) also presents good similarity between the two transects with a normalized root mean square error of 0.220. In these transects, the isotherms having a similar vertical distribution, despite the differences in the data sources and bathymetric resolution.

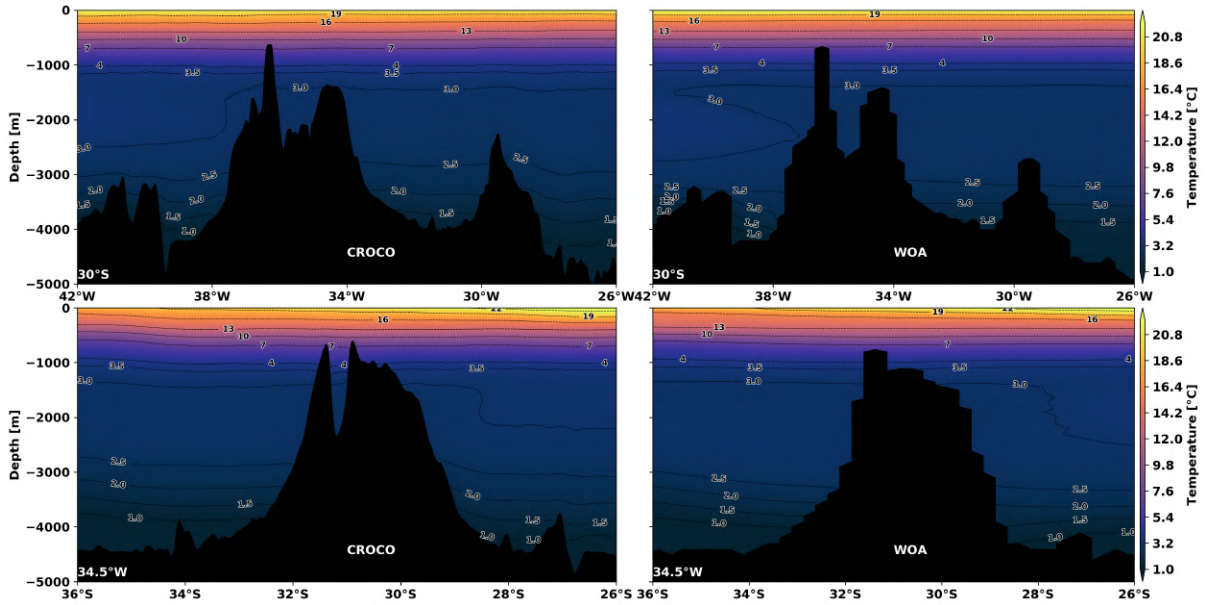

Figure 4.1: Upper panels: Mean temperature transects at 30°S between 36°W and 42°W for the CROCO model output (left panel) and the WOA 2018 dataset (right panel). Lower panels: Mean temperature transects at 34.5°W between 26°S and 36°S for the CROCO model output (left panel) and the WOA 2018 dataset (right panel).

Besides that, we construct a Temperature-Salinity (TS) diagram for the zonal transect at 30°S (Figure 4.2). Figure 4.2 shows that the CROCO model output are representing pretty well the WOA temperature and salinity mean field as the TS profiles are overlying each other. The biggest difference is located at the surface with the model output being saltier than the WOA dataset, with about a mean difference of 0.15 g kg^{-1}.

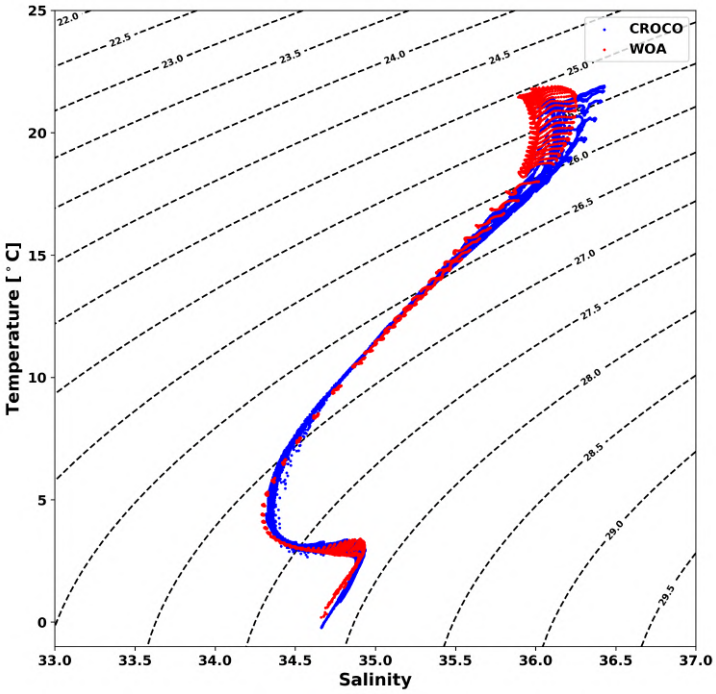

Figure 4.2: TS diagram for the zonal transect at 30°S between 36°W and 42°W. The red dots represents the WOA 2018 dataset and the blue dots the CROCO model output. The dashed lines represents the water density at atmospheric pressure minus 1000 kg m^{-3}.

4.2 Skill Test with the Mooring data

To test the skill of the CROCO model output variability, we compare the velocity time series of the closest grid point cell to the mooring location with the mooring time series. Since the predominant phenomena observed in the mooring data are related to internal tides, more precisely the M2 component, we select a period of one month with one-hour resolution to compare both time series. The period selected corresponds to February 2018. The period of only one month was chosen due to a computational limitation to store high temporal resolution outputs.

We plot both time series and compare their mean velocity components and the velocity variance (Figure 4.3). Figure 4.3 shows a similar variability between both time series, where the velocity can reach 0.2 m s^{-1} and there is consecutive velocity inversions. The last characteristic leads to a almost zero mean velocity in both components on the mooring and in the CROCO output. Both velocity series presents a similar variance (Figure 4.3). The biggest difference between both time series are in the meridional velocity direction, where the mooring presents a southward mean velocity while the CROCO output presents a northward mean velocity.

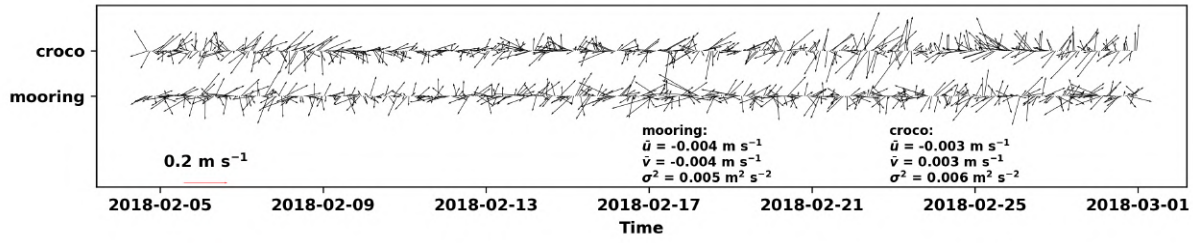

Figure 4.3: Mooring and CROCO model output velocity time series for February 2018 with one hour resolution. The time series statistic are the mean zonal velocity ($\bar{u}$), mean meridional velocity ($\bar{v}$) and the variance (σ^2).

To test the skill of the model in reproduce the M2 tide component observed in the mooring data (Figure 3.3) as being the principal source of variability in the CROCO model output, we plot the PSD for the CROCO and mooring velocity time series (Figure 4.4) with one hour resolution.

We observe that the CROCO velocity time series PSD has the same signature observed in the mooring data PSD (Figure 4.4). With the M2 component dominating, followed by the S2

and O1 components, and some low frequency processes. This indicates that the model variability agrees with the mooring variability.

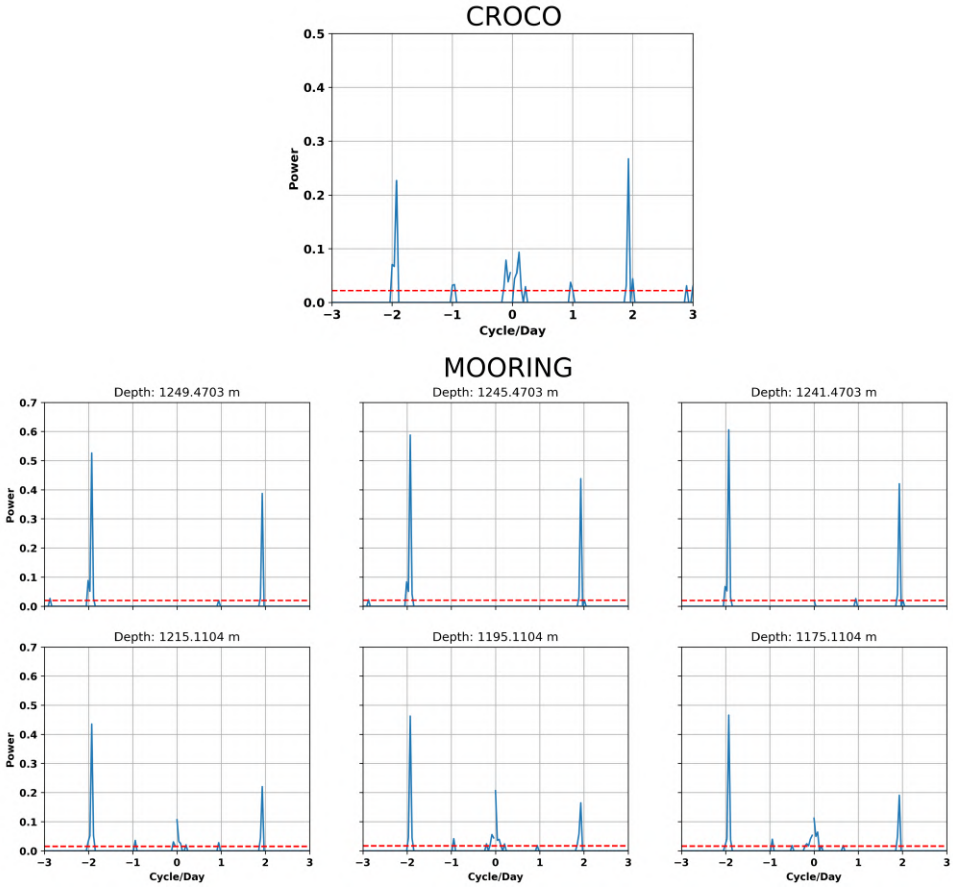

Figure 4.4: CROCO model output velocity PDF for February 2018 with one hour resolution, at 1280 m. Mooring velocity for February 2018 with one hour resolution, at the depths 1175, 1195, 1215, 1241, 1245 and 1249 m. The horizontal red dashed lines mark the 95% confidence level.

As the mooring and CROCO agrees in terms of principals sources of variability, we fit the tidal ellipses using the ttide package (Pawlowicz et al., 2002). This reveals a good agreement between both data sets (Table 4.1). With the M2 major axis intensity for the CROCO and Mooring being 0.039 and 0.056, respectively (Table 4.1). The root mean square error between the Mooring and CROCO is around 0.3 for the M2 and O1 major axis (Table 4.1). The main difference concerns the major axis of the S2 component with a root mean square error between the Mooring and CROCO being of 0.85.

Table 4.1: Ellipse major-minor axes [m s^{-1}] for CROCO and Marine E-Tech mooring in February 2018.

Tide Const.	CROCO Major axis	CROCO Minor axis	Mooring Major axis	Mooring Minor axis	Major axis RMS	Minor axis RMS
M2	0.039	0.000	0.056	-0.004	0.303	1.033
S2	0.018	-0.002	0.010	-0.007	0.852	0.732
O1	0.007	0.002	0.011	0.002	0.345	0.015

The differences observed here can be easily caused by to the fact that the mooring are located close to the bottom at the CSR slope (Figure 2.1), a place with several trenches as observed in Figure 1.3. However, the model bathymetry has a resolution of approximately 2 km with a additional smoothing to avoid pressure gradient errors (see section 2.2). Because of that, probably the local circulation found where the mooring were deployed cannot be represented perfectly.

The hydrographic field and the variability of the model are in agreement with the WOA-2018 and the Marine E-Tech Mooring, respectively. From now on, we will investigate the dynamics of the RGR focusing on the dynamics within the CSR using the CROCO output.

5 Mean Flow

This chapter describes the flow averaged of the two years of simulation after kinetic energy stabilization. It is organized in three sections, where we will approach the following topics, the mean flow around the RGR, within the CSR and at the RGR bottom. To conduct the description we will use the two years mean from CROCO output, where we choose four levels to characterize it, one above the RGR at 400 m, and the others three levels in the RGR domain at 700 m, 1000 m and 1200 m. Also, we select a few meridional vertical sections to describe the circulation vertical structure.

5.1 Mean Flow around the RGR

The large scale circulation around the RGR is characterized by the presence of the SSEC, centered around 30°S, and that bifurcates after reaching the RGR vicinities (Figure 5.1). Since we are working with a two year mean only, there is alias of mesoscale structures present in the field.

The mean velocity field at 400 m shows that the SSEC bifurcates without the physical presence of the RGR, which does not reach this level. We observe that the northern branch is much more intense than the southern branch (Figure 5.1a). The circulation at the 700 m, 1000 m and 1200 m levels also shows the SSEC bifurcation due to the direct interaction with the RGR. At all levels, the current branches also present asymmetry in transport (Figure 5.1b, Figure 5.1c, Figure 5.1d).

The zonal velocity transects present a clearer view of the currents vertical structure. At 32.6°W, we observe that the SSEC already starts to bifurcate. The northern branch, around 30.5°S, reaches 0.06 m s^{-1}; and the southern branch, at 32°S, reaches 0.01 m s^{-1} (Figure 5.2b). As we go westward, at 34°W, both branches intensify reaching 0.08 m s^{-1} and 0.03 m s^{-1}, respectively (Figure 5.2c). This occurs because of the interaction between the current and the RGR topography, which constrains the flow and increase horizontal shear. It is possible to also notice the formation of an eastward flow from the surface to the the RGR top. The

same feature is present at the transect at 35.35°W indicating the formation of a recirculation (Figure 5.2d). Looking at the 400 m field (Figure 5.1a), we depict the formation of an anticyclonic feature characterized by the relative vorticity maximum, suggesting the formation of a Taylor-like column. At 38.25°W, the SSEC is not directly interacting with the RGR anymore having a core speed of with magnitude of 0.04 m s^{-1} (Figure 5.2e).

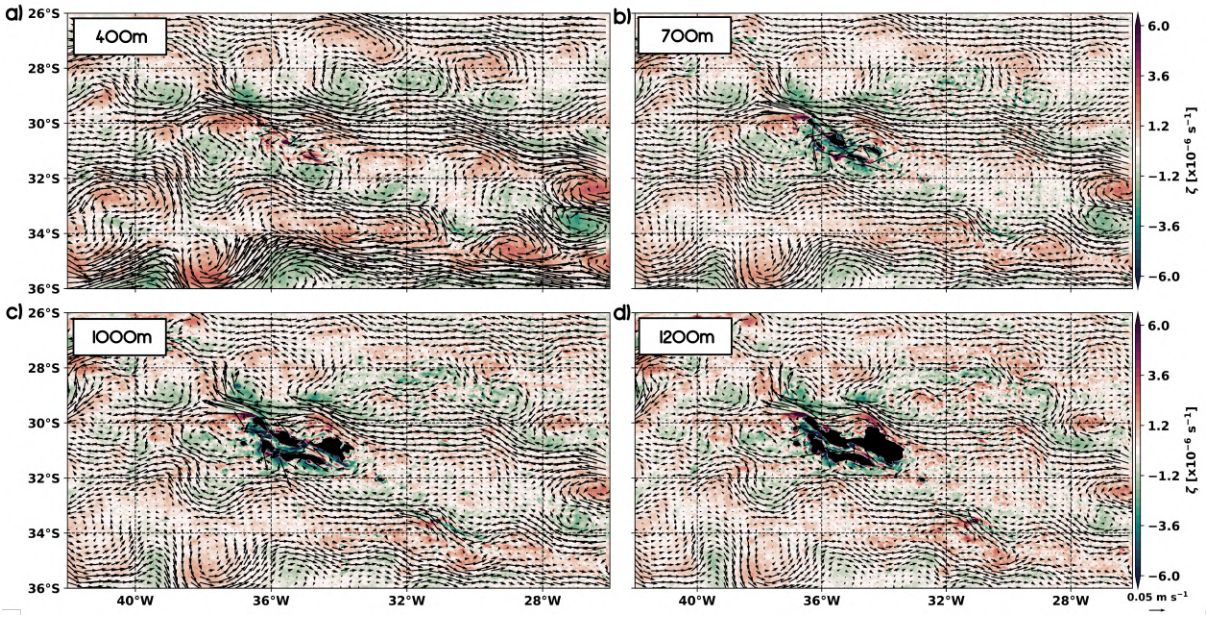

Figure 5.1: Mean velocity horizontal fields with the mean relative vorticity a) 400 m field, b) 700 m, c) 1000 m and d) 1200 m.

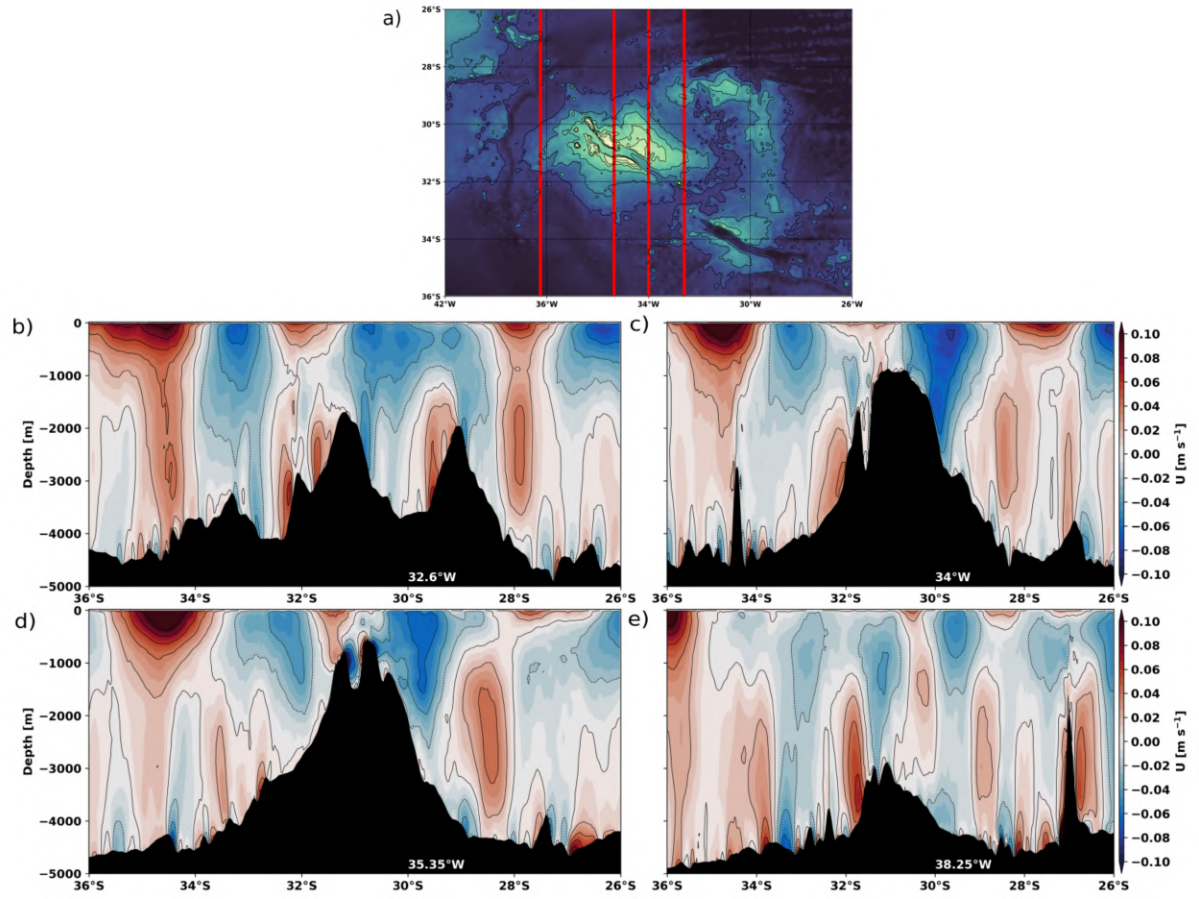

Figure 5.2: a) Bathymetric map with the vertical transects demarcated by the red lines. Mean velocity vertical transects located at b) 32.6°W, c) 34°W, d) 35.35°W and e) 38.25°W.

5.2 The CSR Mean Flow

Above the RGR, at 400 m, we observe in more detail the formation of the mean anticyclonic circulation (Figure 5.3a), corroborating the pattern observed in the Figure 5.2, which suggests the formation of an anticyclonic Taylor-like column.

Deeper, at 700 m, we observe the formation of an anticyclonic circulation around the RGR different peaks (Figure 5.3b). Also, a small portion of the northern SSEC bifurcation branch passes between the RGR peaks centered 35°W, crosses the CSR, and flows southwestward (Figure 5.3b).

At 1000 m and 1200 m, we observe that the CSR limits are well defined with the northern and southern slopes (Figure 5.3c, Figure 5.3d). Figure 5.3c shows that the SSEC northern bifurcated branch is responsible for forcing the circulation inside the CSR, entering by gap in the northern slope around 35°W. Moreover, Figure 5.3c and Figure 5.3d show that the SSEC is responsible for forcing the circulation inside the CSR through the east opening at about 34°W. At these levels, we depict four anticyclonic recirculation cells around the different peaks of the RGR (centered at 36°W and 31°S, 35.5°W and 30.75°S, 35°W and 31.25°S, and 34.5°W and 30.75°S) is still present, also forcing the circulation inside the CSR.

The transects displayed in Figure 5.4 shows the vertical structure of the anticyclonic circulations along the RGR peaks. We observe that the lobes of the anticyclonic circulations are asymmetric and can vary in thickness, width and intensity, reaching velocities greater than 0.1 m s^{-1}. The anticyclonic circulation characteristics are probably controlled by the local bathymetry.

In order to understand if the anticyclonic circulation around the RGR peaks is a steady process, we investigate it through the the daily outputs, which show that the anticyclonic circulations are present in the daily fields. Hence, they can be considered as permanent features.

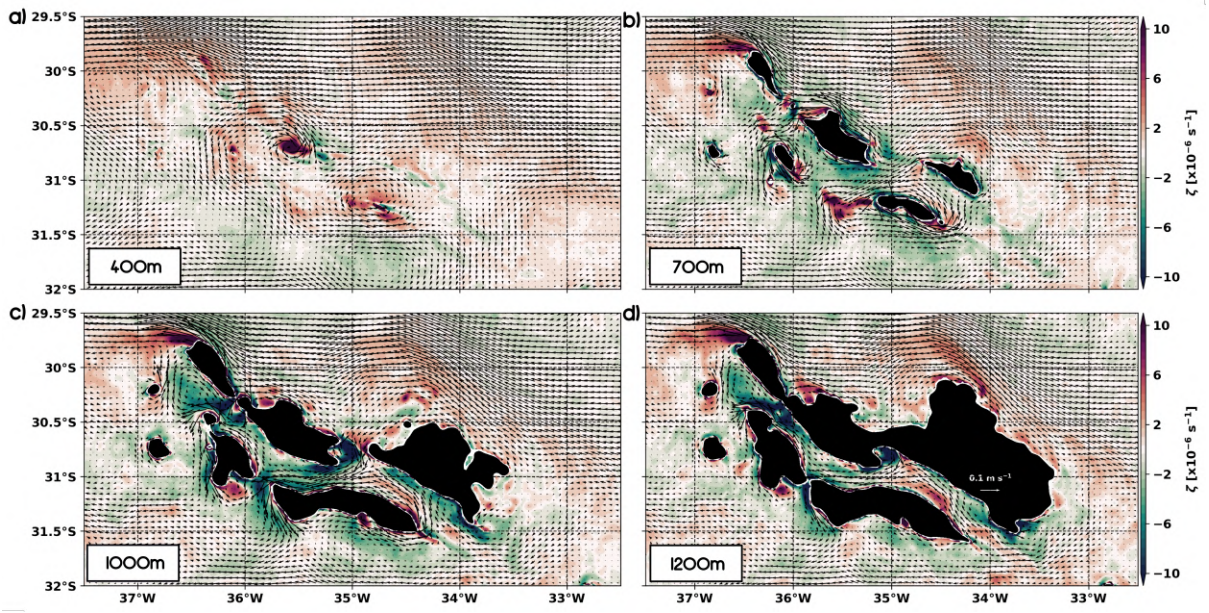

Figure 5.3: RGR mean velocity horizontal fields with the mean relative vorticity at a) 400 m, b) 700 m, c) 1000 m and d) 1200 m.

The formation of an anticyclonic circulation around the seamount summit can be found

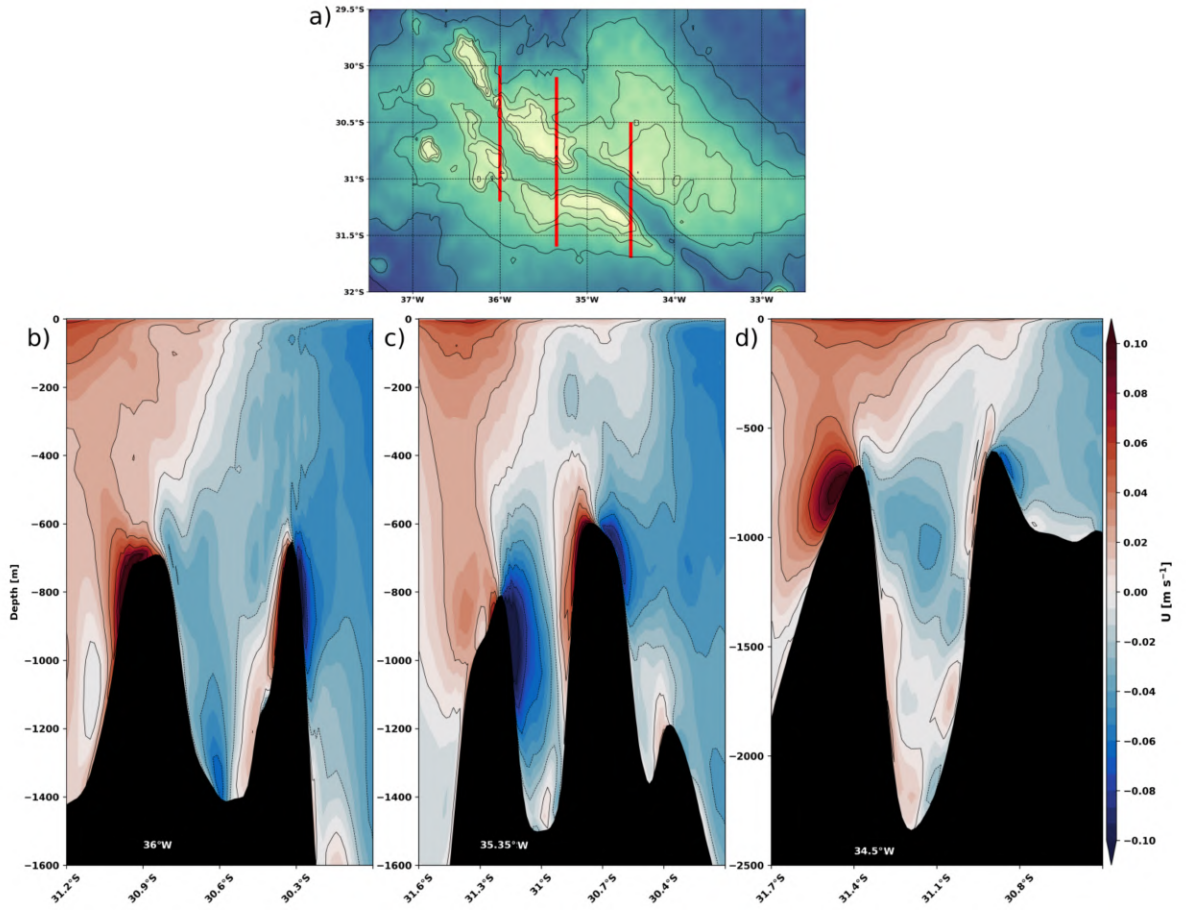

Figure 5.4: a) Bathymetric map with the vertical transects demarcated by the red lines. Mean velocity vertical transects located at b) 36°W, c) 35.35°W and d) 34.5°W.

around many topographic features, like the Le Danois Bank (González-Pola et al., 2012), Condor seamount (Bashmachnikov et al., 2013), Caiwei Guyot (Guo et al., 2020) and the Axial Seamount (Xu & Lavelle, 2017). The main mechanisms responsible for generating this type of circulation around seamounts are the presence of a impinging mean flow or/and the rectification of oscillatory flows.

The presence of an impinging mean flow allows the formation of a Taylor column when the stratification is weak and the anticyclonic circulation goes up to surface. Taylor cap is formed when the the stratification is stronger and constrain the anticyclonic circulation to the seamount summit. This process is a consequence of potential vorticity conservation when steady and stratified currents pass over a ridge or seamount (Chapman & Haidvogel, 1992; Xu & Lavelle,

2017).

The rectification of oscillatory flows occurs mainly with tidal flows. This process happens due to the nonlinear interaction between the tidal flow and the steep topography, allowing the bottom friction and the topographic acceleration develop a up-downslope water transport asymmetry, that produces a net upslope asymmetry (Haidvogel et al., 1993; Chen & Beardsley, 1995; Guo et al., 2020).

Depending on the regional setup, either the mean flow impingement or tidal rectification can be dominant. For example, in the Caiwei Guyot the impinging mean flow the principal responsible for the anticyclonic formation with the interaction between the M2 tidal component and the topography playing a secondary role (Guo et al., 2020). Otherwise, at Le Danois Bank the M2 tidal rectification plays the major role in dictating the anticyclonic circulation with the impinging mean flow as a second factor (González-Pola et al., 2012).

In the RGR there are evidences that support the formation of the anticyclonic circulation by both processes. There is the presence of the SSEC impinging on the RGR topography, and also the M2 tidal component are the principal source of super-inertial variability.

5.3 RGR Bottom Mean Flow

In order to help to explain the sediment and the Fe-Mn crusts distribution (see Figure 1.4), we evaluate the mean velocity field adjacent to the ocean bottom. This is feasible since our model has terrain-following coordinates (section 2.2).

The mean bottom velocity field reveals that at the RGR summits the mean velocity can reach 0.2 m s^{-1}, and presents an anticyclonic circulation pattern (Figure 5.5). On the other hand, the mean circulation in the CSR valley presents null velocities in almost all domain. The velocity just has an increase close to the CSR west opening around 36°W (Figure 5.5).

The velocity pattern shown in Figure 5.5 can help to explain the distribution of Fe-Mn crusts, as well as, the carbonate plates (Figure 1.4). This substrates are located in areas with a mean circulation between 0.1-0.2 m s^{-1}, which might be enough to avoid deposition.

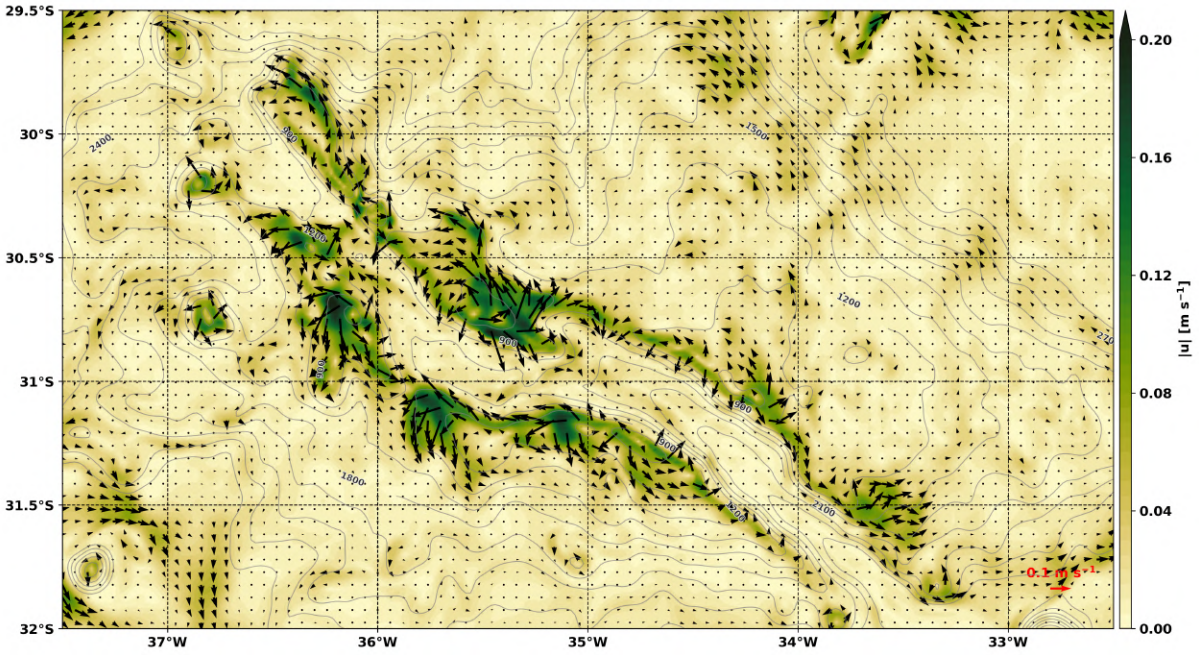

Figure 5.5: RGR mean bottom velocity.

5.4 Tidal Rectification

To understand which one of the mechanisms are the main responsible for the formation of the anticyclonic circulation, we compare the the realistic numerical experiment with the numerical experiment without tidal forcing in order to evaluate how the tides are responsible for modify the mean flow.

The Figure 5.6 shows a decrease of the anticyclonic circulation lobes intensities and in some places it almost vanishes, when compared with the Figure 5.4. It become clear when we look to the velocity at the bottom at Figure 5.7, where the velocity becomes practically null where it used to reach 0.2 m s^{-1} (Figure 5.5).

The comparison between both experiments revels that the absence of tides are responsible for greatly reduce the anticyclonic circulation. Revealing that tidal rectification is the dominant dynamical process responsible for the development of the anticyclonic circulation. The impinging mean flow plays a secondary role, allowing the development of much weaker anticyclonic recirculation.

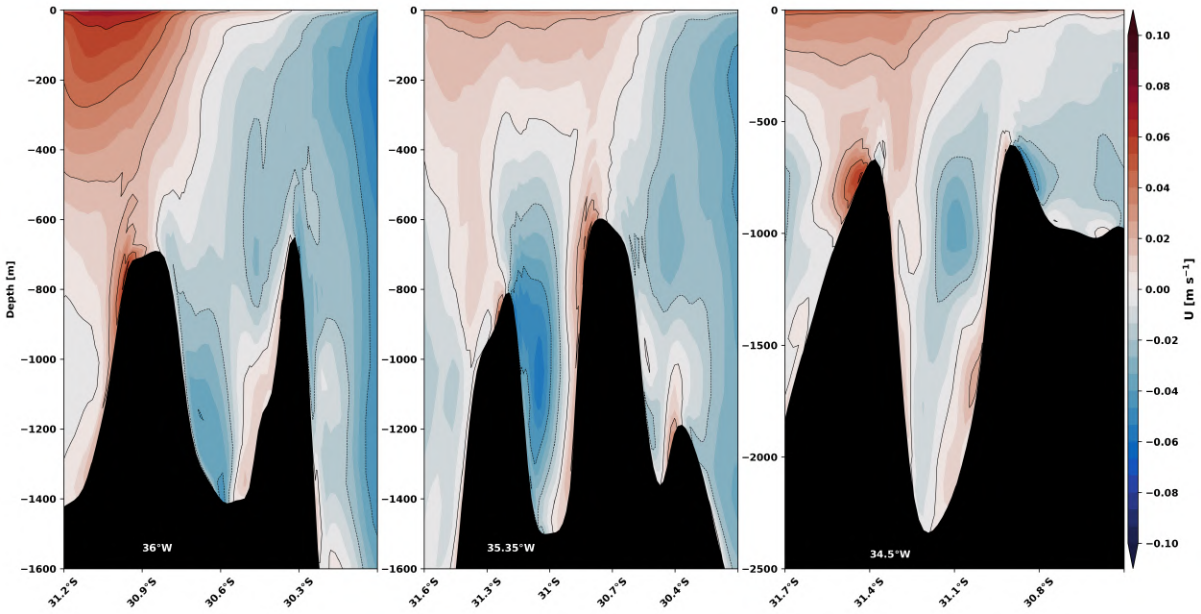

Figure 5.6: Mean velocity vertical transects located at 36°W, 35.35°W and 34.5°W for the model without tidal forcing.

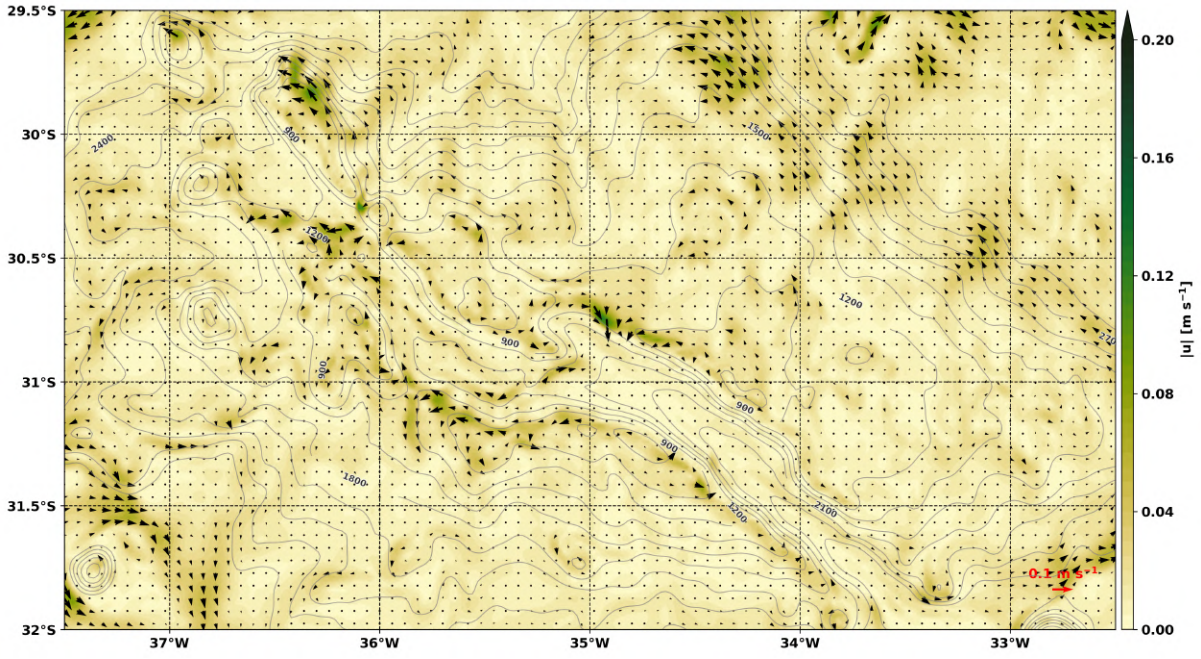

Figure 5.7: RGR mean bottom velocity for the model without tidal forcing.

6 Internal Tide Dynamics

The mooring data revealed the importance of the tides in the CSR variability, specially the M2 component. However, as we have just one mooring line close to the bottom, we do not have a fully understanding of the processes the occurs in the RGR, principally due to the limited spatial coverage.

To understand the dynamics linked to the internal tides, we employ one month of the CROCO output series with hourly resolution, the same used in the section 4.2. This time series corresponds to the month of February 2018, spanning approximately 54 M2 tidal cycles. This chapter is organized in three sections, in which we evaluate the tidal influence, the formation of tidal beams, and the existence of diapycnal mixing and baroclinic eddies.

6.1 Internal Tide Influence

Figure 6.1 shows two snapshots separated by 6h. The snapshots shows that inside a M2 tidal cycle the velocity direction inside the CSR can change and the velocity can reach 0.2 m s^{-1}. It is also responsible for changing the SSEC velocity magnitude.

Hence tides are important inside the CSR. They are responsible for the change in the velocity magnitude, sometimes generating flow inversions. Thus, we seek to understand how this influence are distributed along the water column. Figure 6.2a and Figure 6.2b reveal that the large scale circulation are almost not affected by the tidal effects, we just observe some small changes in the velocity magnitude. Otherwise, we observe some velocity inversions on the RGR top. Figure 6.2c and Figure 6.2d show that on the RGR top and inside the CSR, we have in addition to the change of velocity magnitude, velocity direction inversions, indicating that tides are more important at this site.

To compute the tide component of the flow, we fit the M2 tidal harmonic, which is to be observed the most important in the region, using ttide (Pawlowicz et al., 2002). Figure 6.3 shows the velocity due to the M2 component, as expected the velocity due to the M2 component are one order of magnitude higher on the RGR top than the others areas (Figure 6.3a, Figure 6.3b).

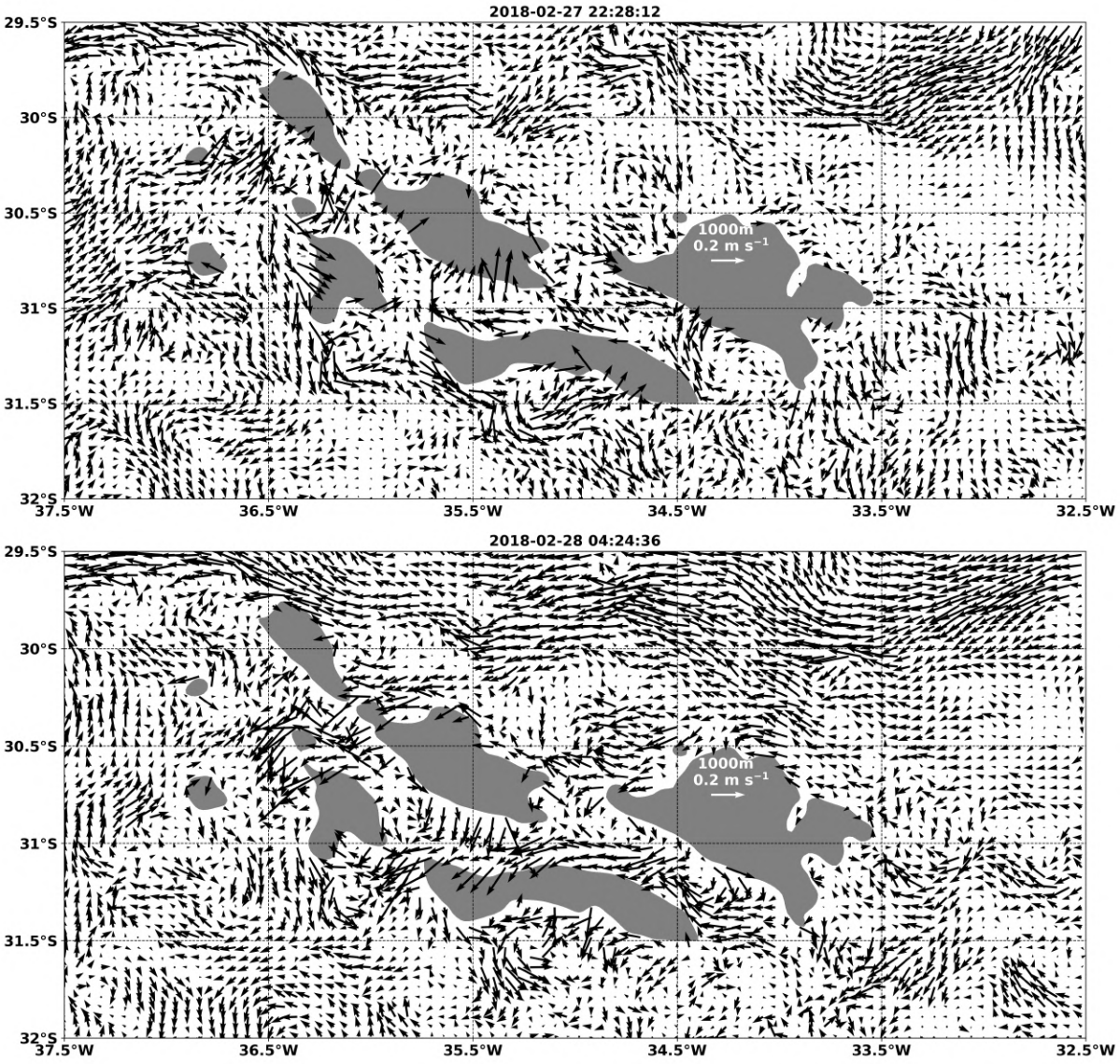

Figure 6.1: Velocity snapshots at 1000 m with 6 h difference. Click on the image to watch the temporal evolution.

The Figure 6.3c and Figure 6.3d highlight the velocity pattern observed during one tidal cycle that can lead to velocity inversions in the total velocity field. We observe that the velocity pattern bellow 1200 m inside the CSR (Figure 6.2c, Figure 6.2d) are mainly dictated by the M2 velocity pattern and resembles a second-mode structure (Figure 6.3c, Figure 6.3d).

To comprehend the role of internal tides in the flow variability, we compute the variance of the total velocity and compare it with the M2 velocity amplitude (Figure 6.4). Figure 6.4

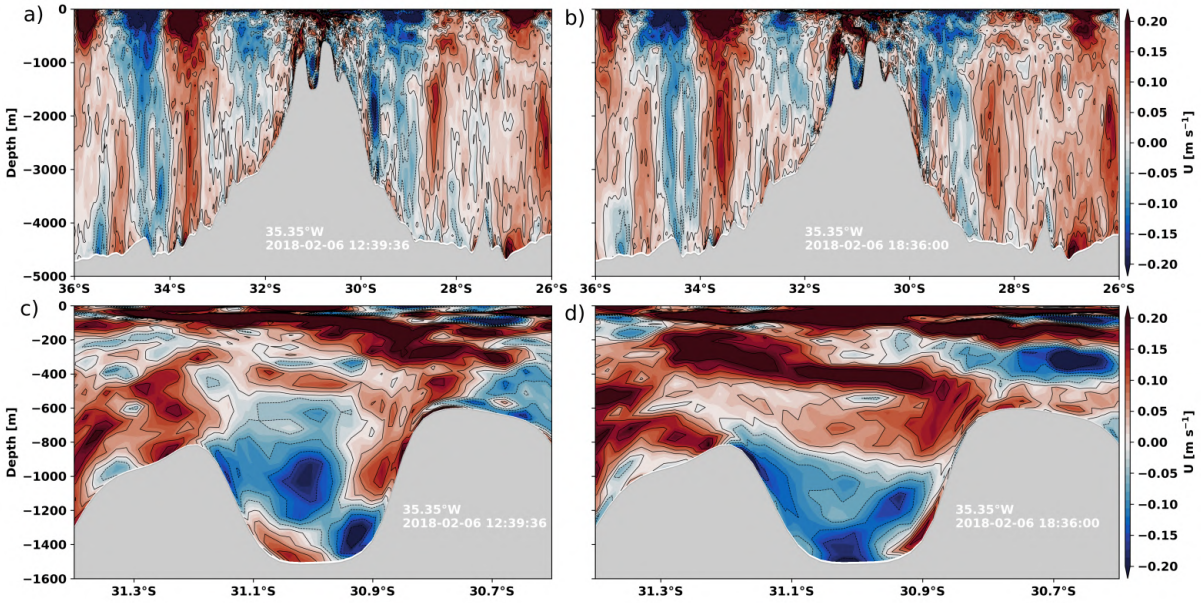

Figure 6.2: Zonal velocity transects at 35.35°W with 6 h difference. Panel a) and b) shows the are between 26°S and 36°S. Panel c) and d) shows the are between 30.8 °S and 31.4°S

shows that the M2 velocity amplitude presents almost the same pattern as that observed in the total velocity variance, showing that the M2 component is responsible for most part of the variability at the RGR top. The M2 velocity amplitude can reach 0.3 m s^{-1}, and there is the formation of beams that apparently tracks the areas where the M2 velocity amplitude are maximum (Figure 6.4).

Figure 6.5 shows the M2 velocity amplitude close to the bottom. We observe that the areas with the higher amplitudes are located at the RGR summits and in the CSR valley, with typically an amplitude of 0.2 m s^{-1}, but that can reach 0.3 m s^{-1}. This distribution might help to explain the dunes observed in Figure 1.3, since it is located on the CSR valley and on the RGR summits. Also, it can explain the distribution of Fe-Mn crusts, since they are exposed at the top of the RGR, where the tides can reach 0.3 m s^{-1}.

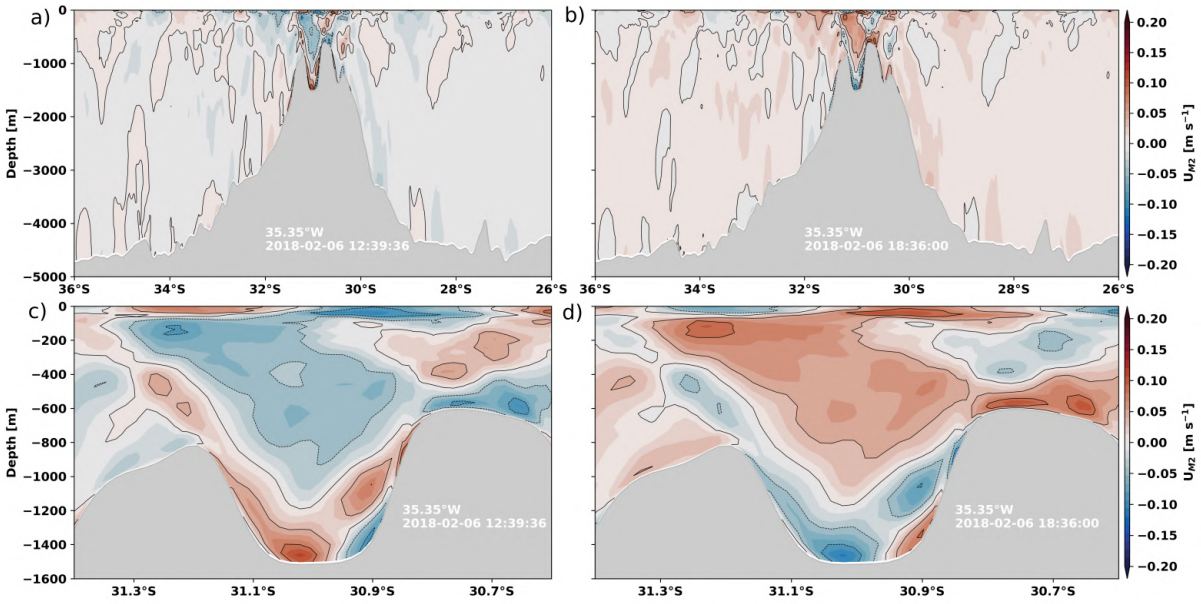

Figure 6.3: M2 tidal component zonal velocity transects at 35.35°W with 6 h difference. Panel a) and b) shows the are between 26°S and 36°S. Panel c) and d) shows the are between 30.8 °S and 31.4°S

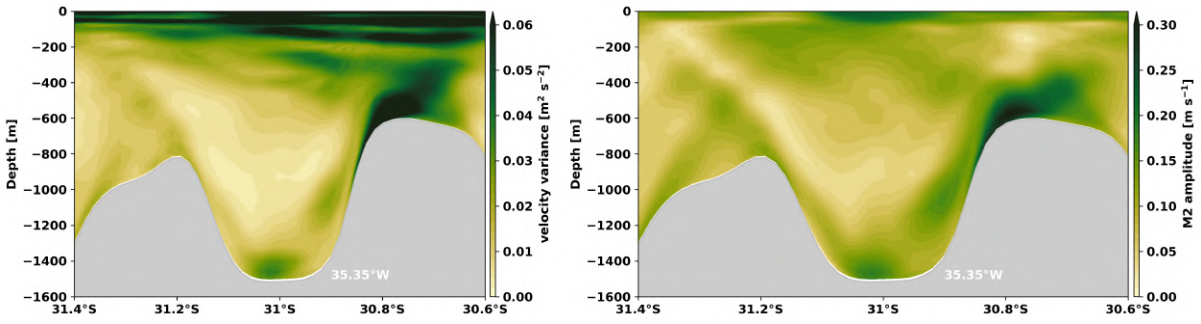

Figure 6.4: Left panel: Velocity variance. Right panel: M2 tidal velocity amplitude.

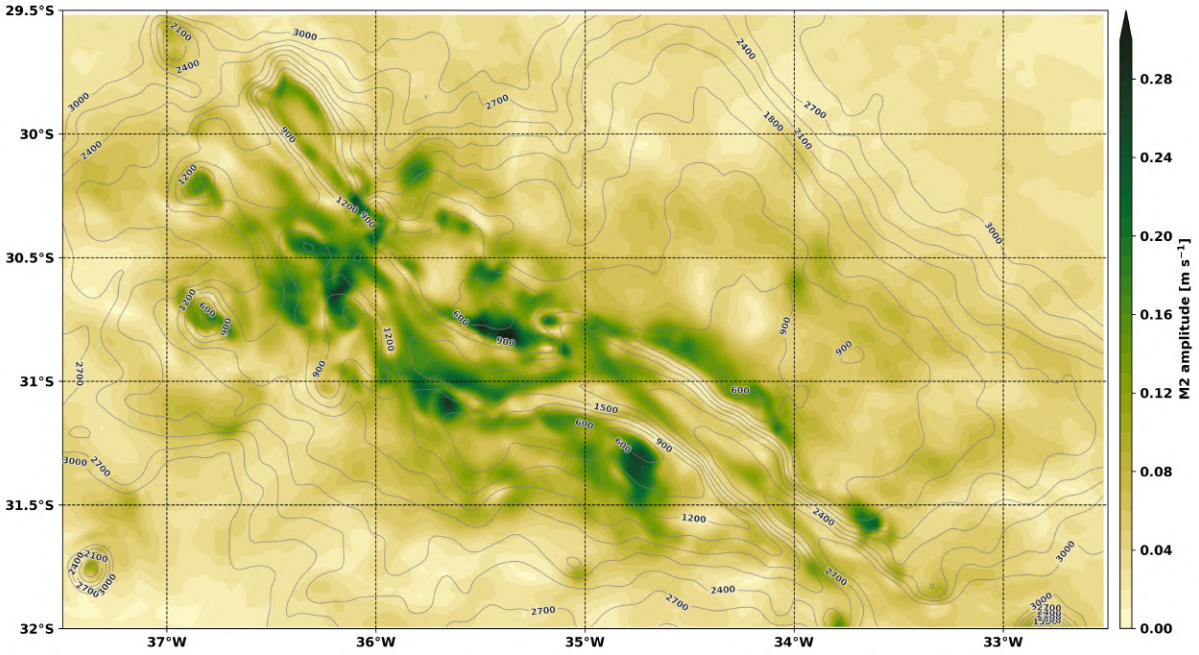

Figure 6.5: Bottom M2 tidal velocity amplitude map.

6.2 Tidal Beams

In order to understand the vertical distribution of the M2 tidal velocity amplitude (Figure 6.4), we are going to explore the possibility of the formation of tidal beams in the region. The formation of tidal beams are relatively common in regions of steep topography, such as the South Brazil Bight (Pereira et al., 2007), the Celtic Sea shelf break (Vlasenko et al., 2014), the Malin Sea continental slope (Stashchuk & Vlasenko, 2017) and the Anton Dohrn Seamount (Vlasenko et al., 2018).

The theory behind the formation of the tidal beams are described on Vlasenko et al. (2005). The dynamical processes that happens inside canyons are considerably dependent of the relative steepness of the bottom topography (α):

$$\alpha = \frac{|\nabla H(x,y)|}{|\gamma(x,y,-H)|}, \tag{6.1}$$

where |∇H(x, y)| is the topographic steepness, H is the water column depth (x and y are

the horizontal coordinates, and z is the vertical coordinate), f is the Coriolis parameter, ω is the tidal frequency, $N(x, y, -H)$ is the buoyancy frequency at the bottom. Also in Equation 6.1, γ is the slope of the internal tide energy propagation which means the inclination of the tidal beam, also known as characteristic paths:

$$\gamma(x, y, z) = \frac{dz}{dl} = \pm\sqrt{\frac{\omega^2 - f^2}{N^2(x, y, z) - \omega^2}}, \tag{6.2}$$

where $N(x, y, z)$ is the temporal mean buoyancy frequency, and l is the x or y direction.

The relative steepness of the bottom topography is responsible for determining two different tidal energy conversion regimes. The subcritical regime occurs when $\alpha < 1$, and it implies that the topography steepness does not control the propagation of the tidal baroclinic energy. Thus, the baroclinic energy propagates predominantly by the generation of lower tidal baroclinic modes (Vlasenko et al., 2005, 2016). When $\alpha > 1$, which happens for steep topographies, we have a supercritical condition that leads to the generation of a variety of baroclinic modes with equivalent amplitudes (Vlasenko et al., 2005; Stashchuk & Vlasenko, 2017). The tidal beam are formed when the modes concentrates along a narrow wave guide where the baroclinic tidal energy radiates from the bottom. The beams are originated in critical regions where $\alpha \approx 1$. The tidal beam allows the propagation of the energy downward and upward along the characteristic paths with group velocity, while the phase speed propagates perpendicular to the beam (Vlasenko et al., 2005, 2016).

To infer the possibility of the the formation of tidal beams inside the CSR in the RGR domain, we calculate the parameter α for the region (Figure 6.6), based on the fact that the M2 tidal frequency is the predominant tidal frequency. Figure 6.6 shows that the slopes of the CSR presents supercritical conditions ($\alpha > 1$), revealing that the topography has an important role in dictating the M2 tidal baroclinic energy propagation, and in allowing the tidal beams formation.

To understand if the tidal beams develop in the region, we plot the the M2 tidal velocity amplitude presented in Figure 6.4 with the characteristic paths given by Equation 6.2. We considered two calculations, one using the horizontal mean N^2 structure from the model (Figure 6.7a), and another, employing the horizontal mean N^2 profile calculated from the *in-situ* data. Figure 6.7 shows a high correspondence between the M2 tidal beams pathways and the

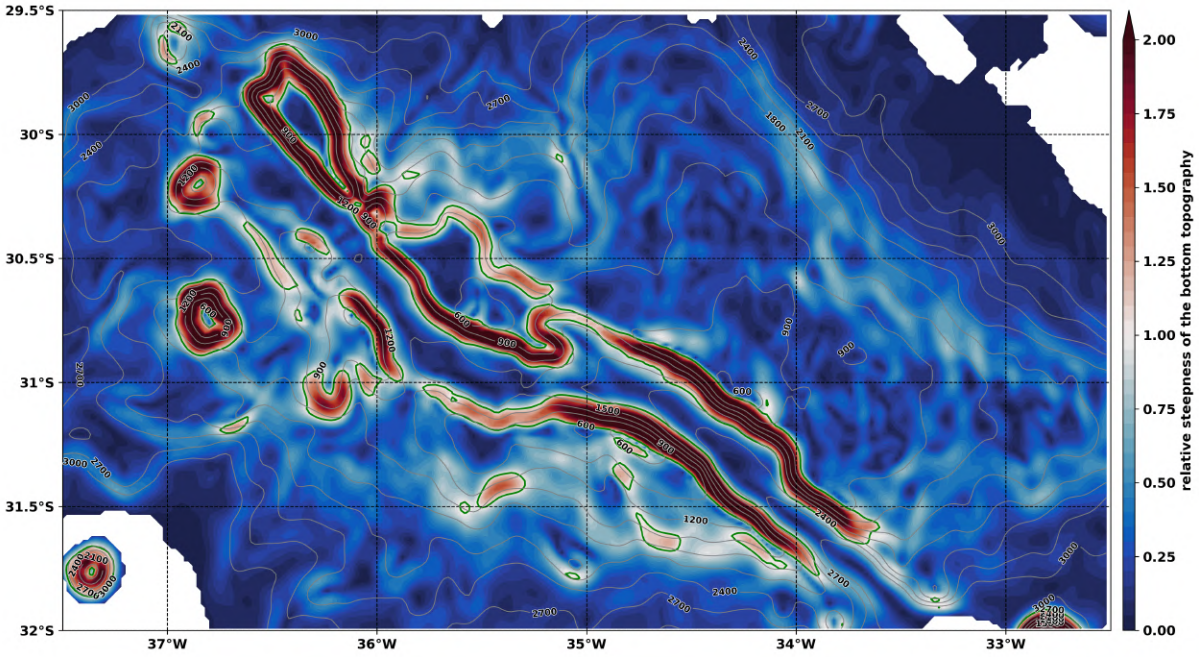

Figure 6.6: Map of the relative steepness of the bottom topography. The green line shows where $\alpha(z, y, -H) = 1$.

areas with higher M2 velocity amplitudes, corroborating that the M2 amplitude pattern occurs due to the formation of tidal beams.

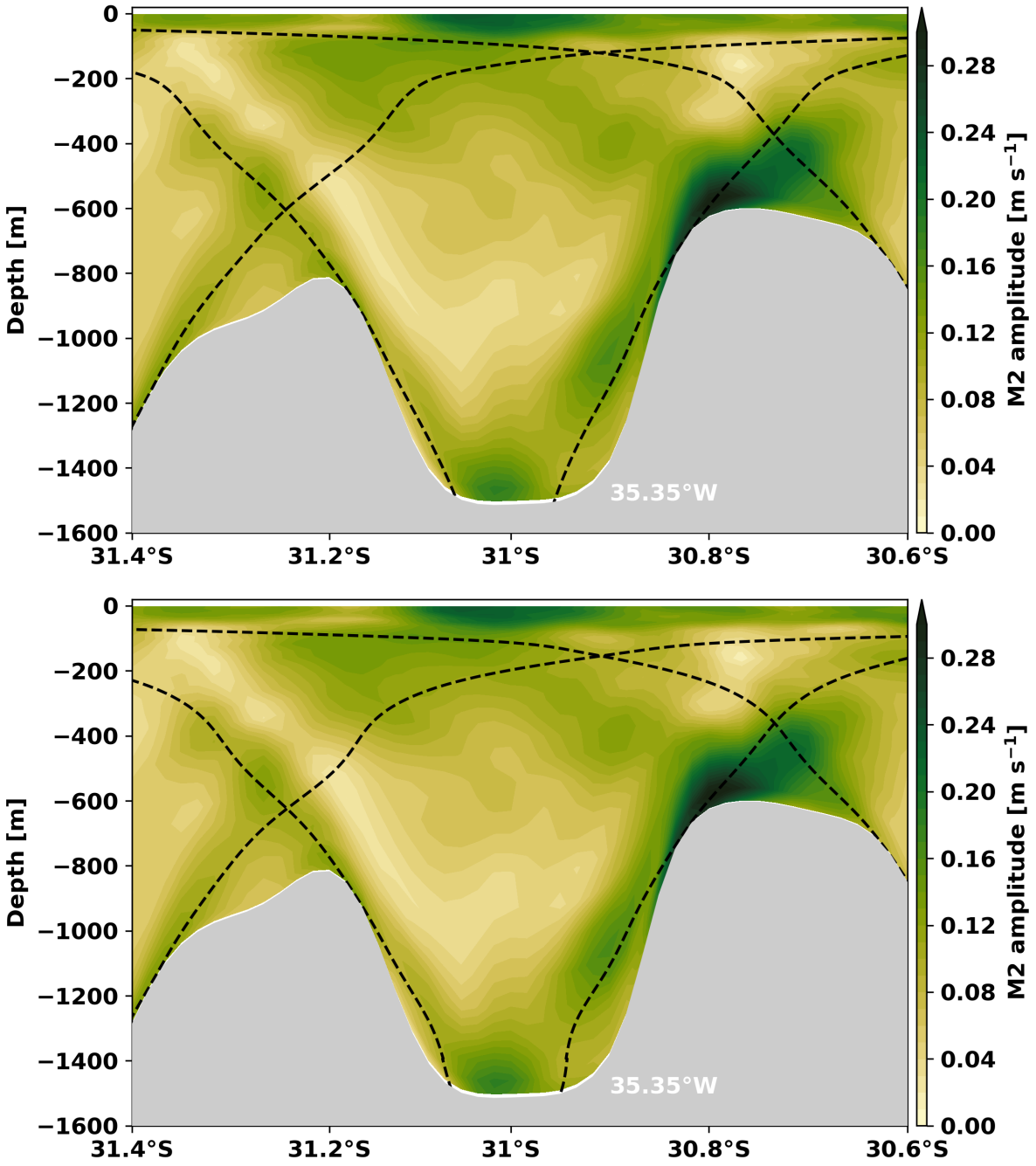

Figure 6.7: M2 tidal velocity amplitude with the characteristics paths (black dashed lines), which are originated where $\alpha(x, y, -H) = 1$. Top panel: it uses the mean N2 profile from the CROCO section. Lower panel: it uses the mean N2 profile from the along-canion observations.

6.3 Diapycnal mixing and Baroclinic Eddies

In the process that the tidal beams propagate energy downward to the CSR valley, this energy cannot be accumulated indefinitely at the bottom. This energy should increment the local mixing (Vlasenko et al., 2016). To evaluate the possibility of diapycnal mixing, we plot the eddy diffusivity (κ) that is calculated by CROCO using the KPP parametrization. We use the κ profile in the middle of the CSR in Figure 6.7. In addition to that, we also calculate the Richardson number (Ri),

$$Ri = \frac{N^2}{u_z^2 + v_z^2}, \tag{6.3}$$

that works as a proxy to the eddy diffusivity. According to Pacanowski & Philander (1981), the diffusivity coefficient can be parametrized using the the Ri number, following the given relation:

$$\kappa = \frac{\nu}{(1 + sRi)} + \kappa_b, \tag{6.4}$$

where ν is the vertical viscosity coefficient, s is an adjustable parameter, and κ_b is the background dissipation parameter. Equation 6.4 shows that κ has a negative correlation with Ri.

Figure 6.8 (left panel) reveals an increase of the diffusivity close to the bottom, and it appears in Ri profiles in Figure 6.8 (right panel). The κ values increases from approximately 0 in the middle of water column, being able to reach more than 0.03 m^2 s in the bottom. These results indicate the existence of diapycnal mixing close to the bottom, which is seen where both beams encounter the bottom (Vlasenko et al., 2016).

Moreover, we plot a 24h Hovmöller diagram for density and zonal velocity (Figure 6.9). Figure 6.9 evidences in both Hovmöllers the two M2 tidal cycles. The density Hovmöller shows a vertical displacement of the isopycnals that can reach 70 m during a tidal cycle. Also, it it observed a mirrored pattern between the isopycnals between the intervals 800-1400 m and 1400-1500 m (bottom). This pattern is also observed in in the zonal velocity Hovmöller, where between the first depth interval, we have a westward flow, and in the second interval, close to the bottom, we have an eastward flow. Also, the eastward flow adjacent to the bottom is two times stronger than the westward flow above it, with 0.2 m s^{-1} and 0.1 m s^{-1}, respectively.

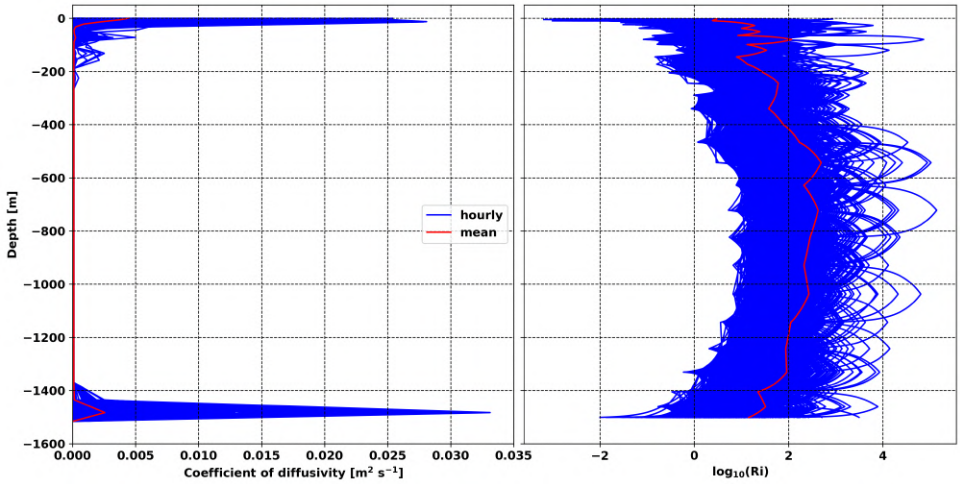

Figure 6.8: Left panel: Diffusivity coefficient profile from CROCO parametrization. Right panel: Richardson number profile. The blue lines show hourly profiles, and the red line corresponds to the mean κ and Ri profiles in each panel, respectively.

Additionally, the stronger flow adjacent to the bottom coincides with higher tidal amplitude adjacent to the bottom observed in Figure 6.7. The velocity and density pattern (Figure 6.9) indicates that the increase of the diapycnal mixing close to the bottom (Figure 6.8) seems responsible for inverting the isopycnal gradients. Looking to the mean zonal velocity section at 35.35°W, we also observe a eastward flow adjacent to the bottom (Figure 5.4c).

In this region, there is the passage of cyclonic eddies between 800-1400 m, as will be discussed in the next chapter. As a probable consequence of the enhanced diapycnal mixing approximately 100 m from the bottom, there is an inversion on the isopycnal gradients close to the bottom, leading to the generation of a baroclinic eddy (Figure 6.10). Figure 6.10 (left panel) shows the formation of a cyclonic eddy at 1000 m and an anticyclonic eddy at 1450 m at 35.35°W, with the zonal velocity vertical transect showing the opposing lobes of the eddy and the isopycnals distribution (Figure 6.10, right panel). The isopycnals distribution presents a mirrored pattern adjacent to the bottom as observed in Figure 6.9. The formation of a baroclinic eddy due to the enhancement of diapycnal mixing caused by tidal beams are also reported by Vlasenko et al. (2016). However, our case differs from the previous authors' because the tidal beams in their case meet at the canyon middle depth while ours, only at the bottom.

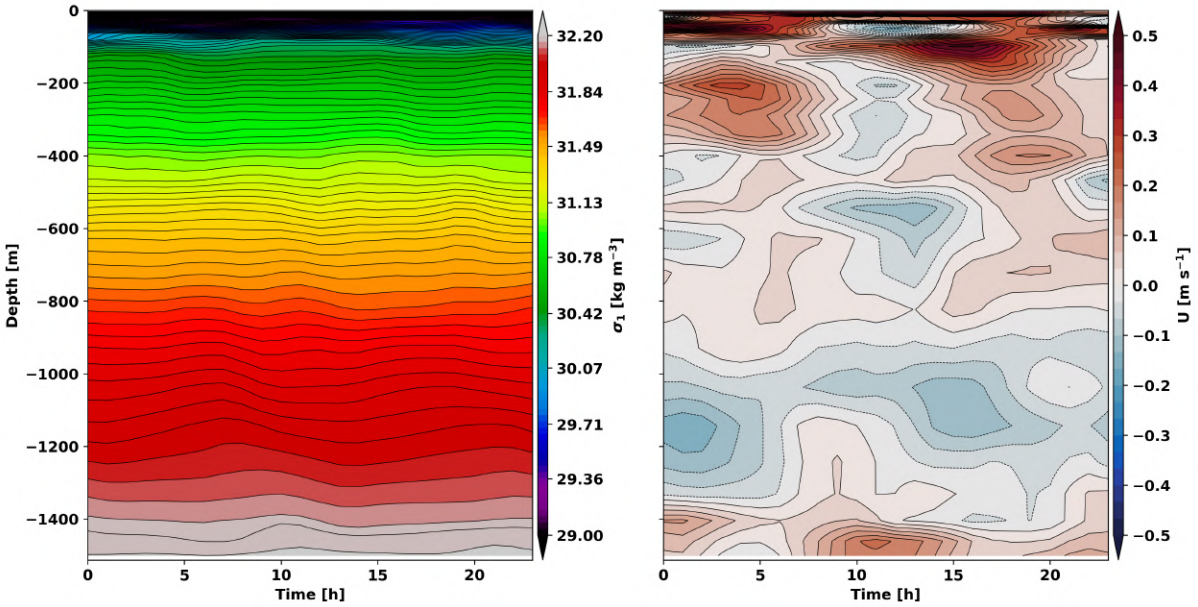

Figure 6.9: Left panel: Hovmöller diagram of the density in the middle of CSR at 35.35°W. Right panel: Hovmöller diagram of the zonal velocity in the middle of CSR at 35.35°W.

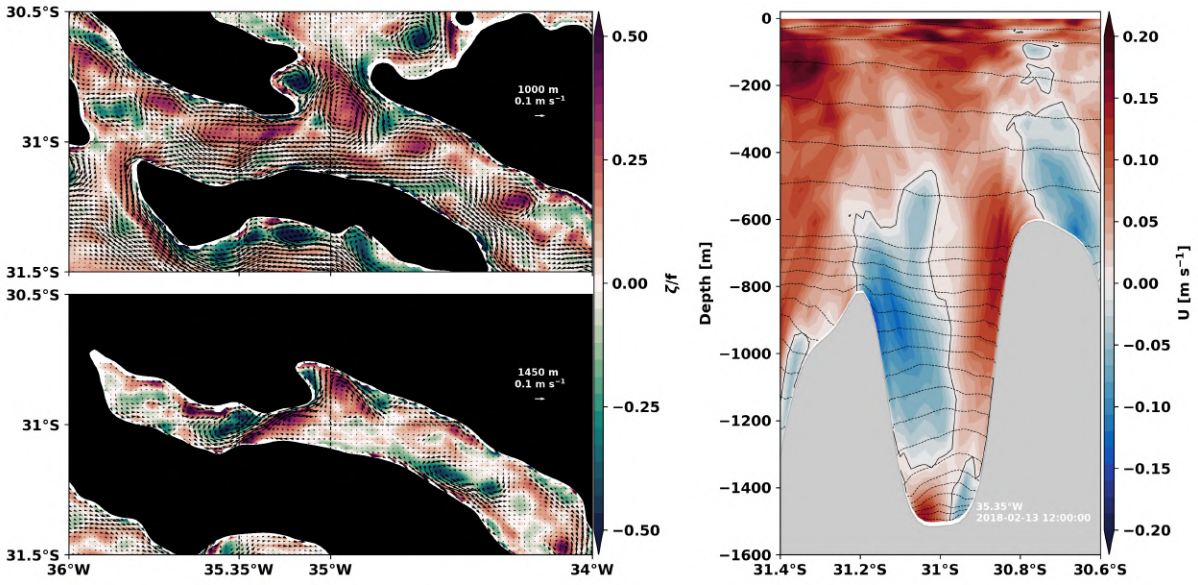

Figure 6.10: Left side: Velocity maps at 1000 m (top) and 1450 m (lowest). The maps also presents the Rossby number that is the ratio of the relative vorticity by the Coriolis parameter. Right side: Zonal velocity transect at 35.35°W. The dashed lines shows the isopycnals. These figure uses the mean daily output.

7 Submesoscale Eddies

The CROCO model output reveals that the flow inside the CSR is marked by several perturbations that can develop into eddies, adding more complexity to the local dynamics. To investigate the eddies dynamics, we use the average daily fields.

This chapter is organized in three sections, in which we describe the flow, evaluate the submesoscale dynamics, and investigate the processes that may contribute to the eddies generation.

7.1 Flow Description

The RGR circulation is complex, besides the dynamics linked to tidal processes and the anticyclonic circulation around the RGR summits, we also have the formation of eddies. The description of the flow focuses on the CSR domain.

As mentioned in the chapter 5, the SSEC forces the circulation inside the CSR by the northern slope opening at 35°W, and by the eastern opening around 34.5°W. When the current enters by any of these openings, it interacts with the topography, generating perturbations that can eventually develop into eddies. The eddies formed can be either anticyclonic or cyclonic (Figure 7.1).

The eddies formed in the eastern opening, about 34.5°W, are a result of the SSEC entering and the anticyclonic circulation around the RGR peaks. Most of the times, they are formed through the interaction of these currents with the CSR southern slope. This interaction generates perturbations that can develop into anticyclonic eddies (first column, Figure 7.2). Those vortical features propagate westward until 35°W, where they interact with the current branch entering by the northern slope, and are subsequently destroyed (Figure 7.1). At the eastern opening, Figure 7.2 (first column) evidences the formation of the anticyclonic eddy with a radius of the order of 10km, a vertical extension of 1000m (between 500 m and 1500 m) and Rossby number (Equation 7.1) order 1.

Otherwise, the SSEC entering by the northern slope about 35°W usually form both anticyclones and cyclones. These features have a radius of approximately 10 km and a vertical

extension of 1000 m (between 500 m and 1500 m), with the Rossby number reaching order 1 values (second column, Figure 7.2).

A third scenario depends of the intensity of the westward flow inside the CSR, which can initiate the formation of cyclones in the west side tip of the northern slope opening at 35°W. These cyclones can propagate until the CSR west opening about 36°W (Figure 7.1). The eddies formed at this place have a vertical extension of 1000 m (between 500 m and 1500 m) and a radius of 10 km with Rossby number order 1 (third column, Figure 7.2).

As it can be observed in Figure 7.1 and Figure 7.2, the eddies inside the CSR have Rossby number $Ro = \mathcal{O}(1)$, where

$$Ro = \frac{\zeta}{f} = \frac{v_x - u_y}{f}, \tag{7.1}$$

and ζ is the relative vorticity. It is a indicative of submesoscale activity (Thomas et al., 2008).

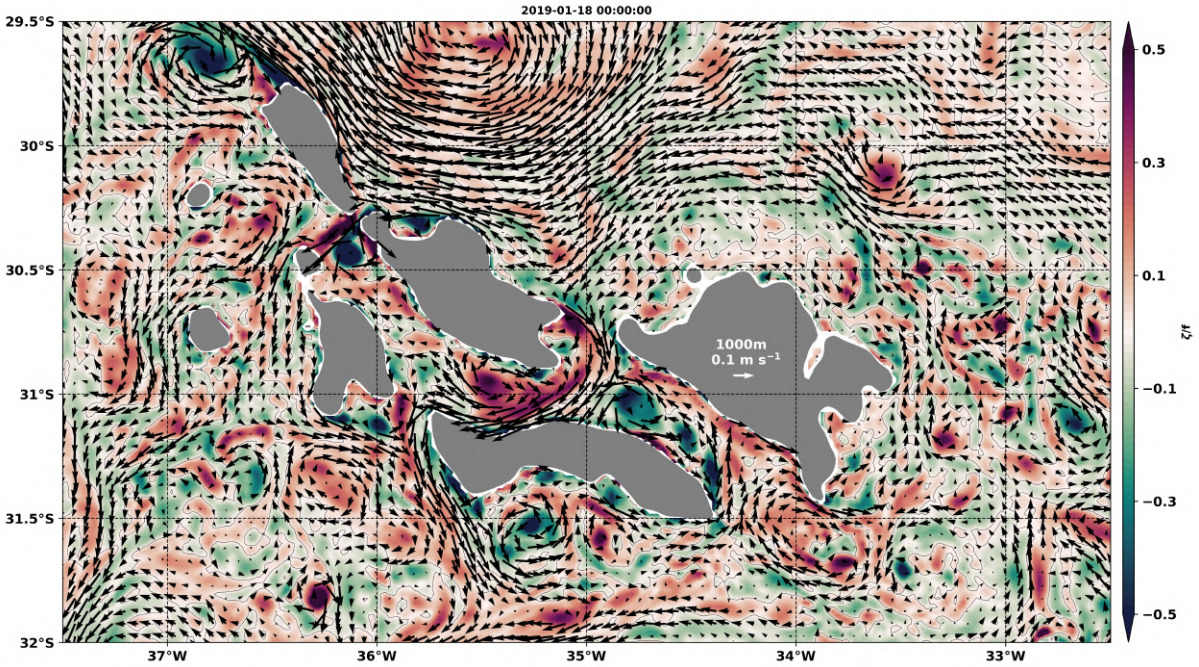

Figure 7.1: The CROCO model output velocity and Rossby number snapshot at 1000 m. Click on the image to watch the temporal evolution.

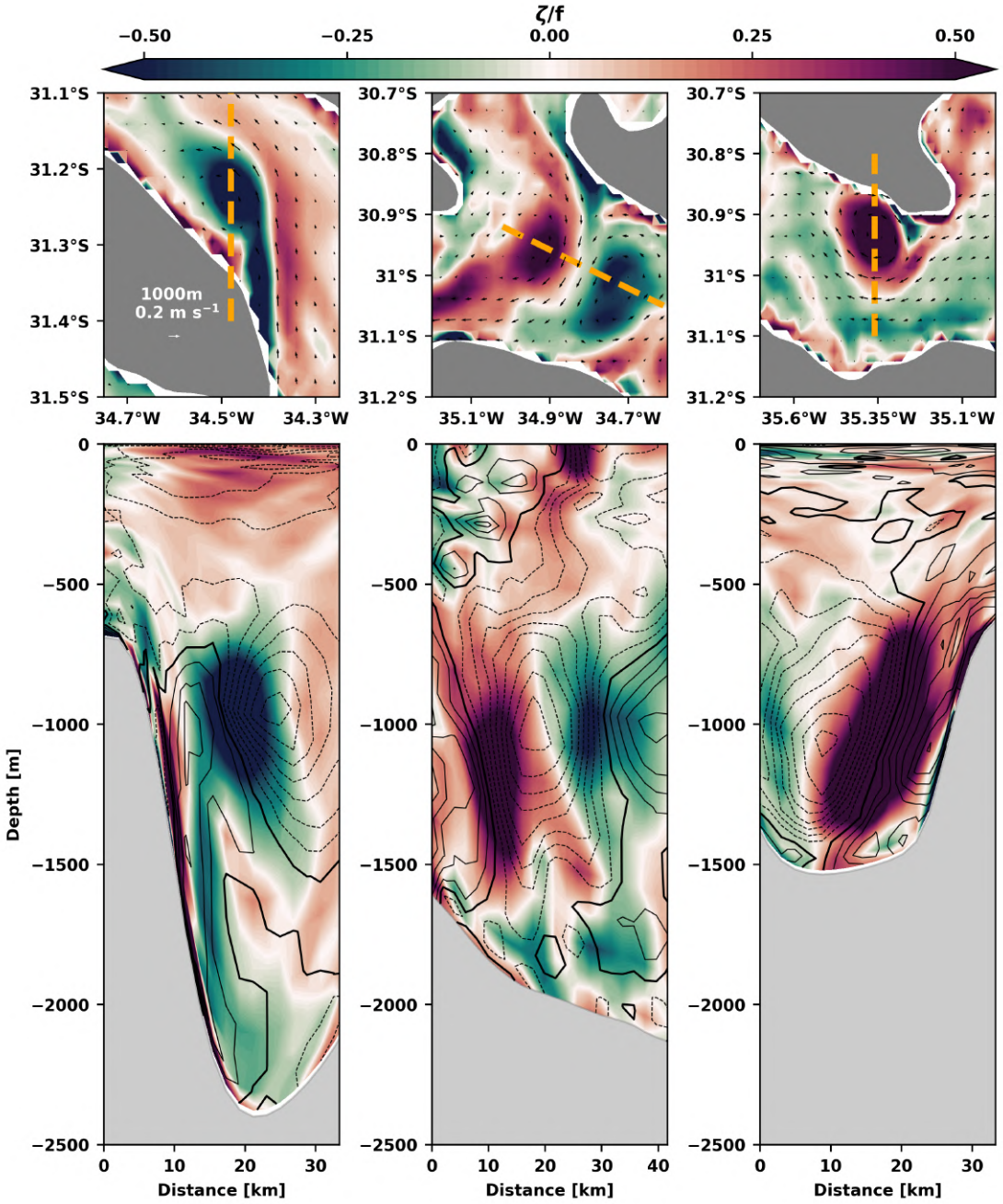

Figure 7.2: CROCO 1000m maps and vertical structure snapshots of Rossby number and velocity for each one of the areas of eddie formation. First column: eastern opening, about 34.5°W. Second column: northern slope opening at 35°W. Third column: west side tip of the northern slope opening at 35°W. The orange dashed lines in the maps delimits the vertical transects presented below. The black lines presented in the vertical transects are the isotachs spaced at each 0.025 m s^{-1}.

7.2 Evaluation of the Submesoscale Dynamics

The submesoscale activity at subtropical latitudes can be defined as the processes with the lateral scales of 0.1–10 km, less than the first baroclinic deformation radius (Mahadevan & Tandon, 2006; Capet et al., 2008a), and time scales of hours to weeks (Gula et al., 2022). These processes are characterized by a Rossby and Richardson number of order 1, and vertical velocities that can reach 100 m day^{-1} (Thomas et al., 2008).

At this scale, several physical processes happens, as density fronts, filaments and eddies (Thomas et al., 2008; Gula et al., 2022). These processes are responsible for redistributing water properties as buoyancy, momentum, heat and salt (Mahadevan, 2016). More than that, they create a route for energy dissipation by creating a bridge between larger quasi-balanced motions and smaller-scale three-dimensional turbulence (Müller et al., 2005).

The observations of submesoscale processes in areas deeper than 300 m are more scarce and have lesser known dynamics than the process that happen at surface and count with a vast dataset as satellites, ADCPs and CTDs measurements (Marez et al., 2020). Most of the understanding of the submesoscale subsurface processes came with the help of high resolution numerical models. Those models allow the comprehension of the mechanisms responsible for generating the submesoscale features (Marez et al., 2020; Gula et al., 2022).

One of the processes responsible for enhancing the submesoscale dynamics are the interaction of local currents with the topography. Submesoscale studies about flow-topography interaction are recent (Ruan et al., 2017; Garabato et al., 2019; Napolitano et al., 2021; Lazaneo et al., 2022), as well as studies that investigate the dynamics of canyons through high resolution numerical modeling (Vic et al., 2018; Lahaye et al., 2019). The numerical models reveal that the large scale currents interacting with steep slopes, seamounts and ridges allow the formation of submesoscale currents (Gula et al., 2016b; Srinivasan et al., 2019; Vic et al., 2018) that create high rates of local kinetic energy dissipation (Gula et al., 2016b).

As our numerical model horizontal resolution is 2 km, it may allow the development of submesoscale variability. However, the model can only resolve some submesoscale motion. This resolution limitation might underestimate the formation of distinct forms of instability, consequently the total amount of unstable flow (Napolitano et al., 2021). The limitations caused by the relative coarse horizontal resolution of 2 km appears when compared with a higher resolu-

tion models with a horizontal resolution of hundreds of meters as those from Gula et al. (2015) and Molemaker et al. (2015). The increase of our numerical model horizontal grid resolution is prohibitive due to a computational limitation, since we try to reproduce the dynamics around a large topographic feature, the RGR.

As shown in Figure 7.1 and Figure 7.2 the eddies inside the CSR present $Ro\ \mathcal{O}(1)$ and the largest eddies have a radius of 20 km while most of these feature present a typical radius of 10-15 km. The eddies radii are lower than the first baroclinic Rossby deformation radius of 22.6 km (mean value, Table 3.1), one more indicative of submesoscale activity. To have a better understanding of the submesoscale, we evaluate some dimensional and non-dimensional values to diagnose the CSR flow. Among those, we employ the Rossby (Equation 7.1) and Richardson (Equation 6.3) numbers, the horizontal and vertical velocity. Also, we use the divergence (δ), the strain (χ) and the Ertel potential vorticity (q), which are defined respectively as

$$\delta = \frac{\partial u}{\partial x} + \frac{\partial v}{\partial y}, \tag{7.2}$$

$$\chi = \left[\left(\frac{\partial u}{\partial x} - \frac{\partial v}{\partial y} \right)^2 + \left(\frac{\partial v}{\partial x} + \frac{\partial u}{\partial y} \right)^2 \right]^{(1/2)}, \tag{7.3}$$

$$q = \left(f\hat{k} + \nabla \times \mathbf{u} \right) \cdot \nabla b, \tag{7.4}$$

where $\mathbf{u} = (u, v, w)$. Detailed evaluations for submesoscale dynamics can be found in Mahadevan & Tandon (2006), Thomas et al. (2008), Shcherbina et al. (2013) and Napolitano et al. (2021).

We compute the probability density functions (PDFs) for the variables previously mentioned. To compute the PDFs, we use the area delimited by the red region in Figure 7.3 at 1000 m. The PDFs for the horizontal velocity magnitude, vertical velocity, Rossby number, Richardson number, Ertel potential vorticity, divergence and strain are presented at Figure 7.4 with the respective snapshots. The PDFs are accompanied by the statistical parameters as the mean, median, standard deviation (std), and skewness (Figure 7.4).

Figure 7.4a shows that the horizontal velocity reaches more than 0.3 m s^{-1} with a mean velocity of approximately 0.1 m s^{-1}, indicating the presence of highly energetic motions inside

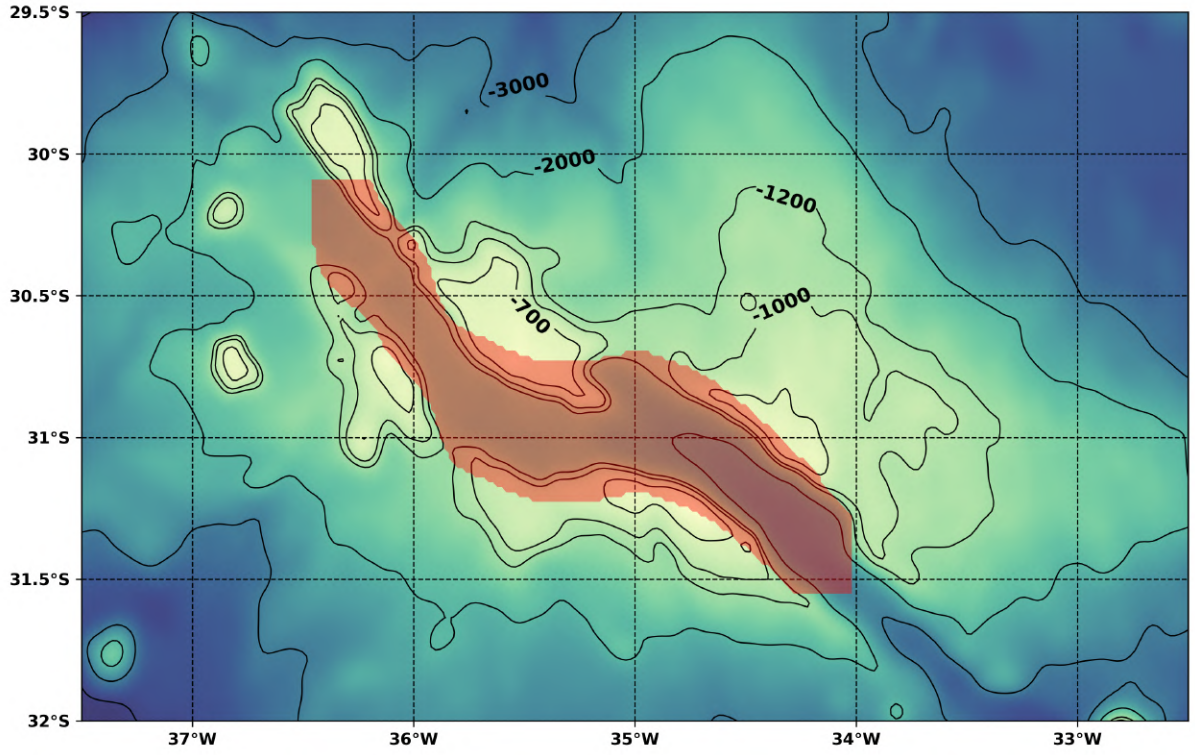

Figure 7.3: The probability density functions (PDFs) are calculated with the grid points inside the red area that delimits the CSR domain at 1000 m.

the CSR. The vertical velocity field in Figure 7.4b in turn can reach velocity order of 100 m day^{-1} with a mean of -1.7 m day^{-1} and standard deviation of 51 m day^{-1}. According to Thomas et al. (2008) the dynamics governed by submesoscale leads to vertical velocities of $\mathcal{O}$(100 m day^{-1}) against the observed $\mathcal{O}$(1 m day^{-1}) of the mesoscale.

The Rossby number snapshot and PDF in Figure 7.4c present a mean of 0.03 and standard deviation 0.33, with a long tail towards anticyclonic motions with a skewness of -1.9. Inside the eddies, both cyclonic and anticyclonic, we find Rossby number $\mathcal{O}(1)$, an indication of submesoscale activity (Thomas et al., 2008). The PDF pattern observed here is similar to that found by Shcherbina et al. (2013) between 350-400 m. The Richardson number (Figure 7.4d) also indicates the presence of submesoscale processes due to some points of $Ri = \mathcal{O}(1)$ ($\log_{10}$(Ri) order 0) (Thomas et al., 2008). We speculates that if the lower values of Ri are due to the fact that the deep ocean presents lower stratification and weaker velocity shear than the upper ocean, where most studies of submesoscale motions have been carried out so far.

Figure 7.4e shows the Ertel potential vorticity times the coriolis parameter (fq), according Thomas et al. (2013) when $fq < 0$ it allows the emergence of submesoscale instabilities. Our field allows the development of submesoscale instabilities given that the PDF in Figure 7.4e presents values of fq less than 0.

Figure 7.4f displays the strain. This property has chi-distribution with a mean of 0.25 and skew of 7.25. A skewed strain distribution, as ours, is also reported by Shcherbina et al. (2013), Rocha et al. (2016) and Napolitano et al. (2021) are characteristic of submesoscale motion. Strain rates higher than 2 are also reported by Rocha et al. (2016) in daily mean model outputs.

The divergence PDF in Figure 7.4g has an almost Gaussian distribution, with a tendency to convergence, due to a mean of -0.01 and a skew of -5.93 with a few $\mathcal{O}(1)$ values. These results show some similarities with the results obtained Shcherbina et al. (2013) and Napolitano et al. (2021).

The values observed in Figure 7.4 show that this model output exhibits the development of submesoscale processes. It present similarities with other studies about submesoscale phenomena despite most of them consisted of studies in the upper ocean and/or in boundary currents. Besides that, the internal tides observed in the region are subject to interaction with the topography and with the submesoscale processes (Whitt et al., 2018; Vic et al., 2018), thus modifying the submesoscale evaluation rates calculated in this section (Napolitano et al., 2021).

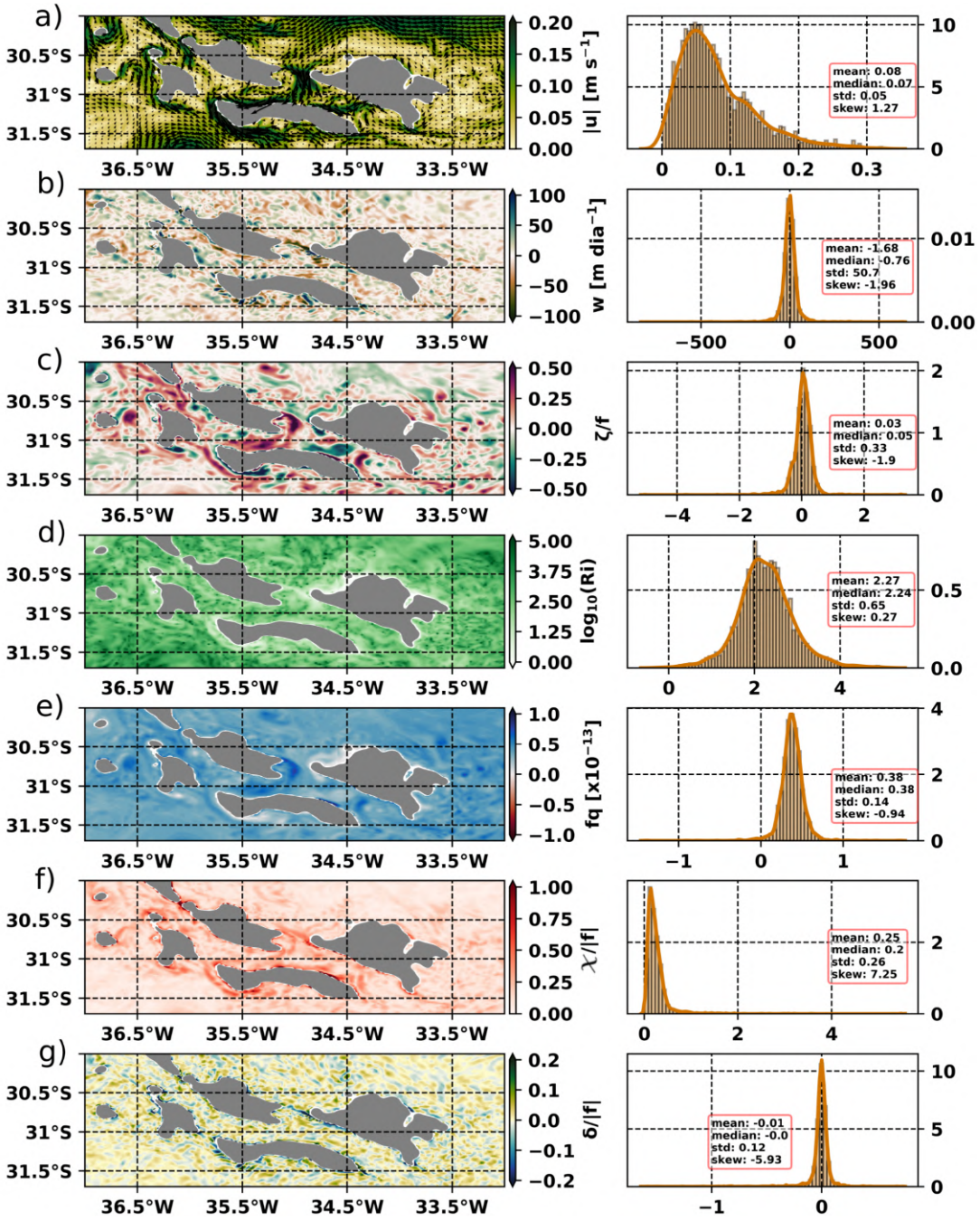

Figure 7.4: 2km CROCO model snapshots with the probability density functions (PDFs) at 1000 m showing in a) horizontal velocity magnitude, b) vertical velocity, c) Rossby number, d) Richardson number, e) Ertel potential vorticity, f) strain, g) divergence.

7.3 Formation of submesoscale eddies

Energy Analysis

In order to have a better understanding of the nature of the instabilities responsible for allowing the formation of the eddies, we are going to explore the energy conversion terms. For this analysis, we need decompose the variables u, v, w and b as $u = \bar{u}+u'$, $v = \bar{v}+v'$, $w = \bar{w}+w'$ and $b = \bar{b}+b'$, respectively. Here, the mean field is characterized by a 60-day mean, and the perturbations terms are the deviations of total field from the mean field. Following Harrison & Robinson (1978) and Gula et al. (2016a), we estimate the following energy conversion terms:

$$SP = HSP + VSP, \tag{7.5}$$

$$HSP = -\overline{u'^2}\frac{\partial \overline{u}}{\partial x} - \overline{u'v'}\frac{\partial \overline{u}}{\partial y} - \overline{v'^2}\frac{\partial \overline{v}}{\partial y} - \overline{u'v'}\frac{\partial \overline{v}}{\partial x}, \tag{7.6}$$

$$VSP = -\overline{u'w'}\frac{\partial \overline{u}}{\partial z} - \overline{v'w'}\frac{\partial \overline{v}}{\partial z}, \tag{7.7}$$

$$BP = -\overline{w'b'}, \tag{7.8}$$

where, SP is the shear production that represents the conversion of the mean kinetic to eddy kinetic energy . The SP can be written as the sum of the horizontal shear production (HSP) and the vertical shear production (VSP). The BP is the buoyancy production and represents the conversion of the eddy potential energy to the eddy kinetic energy. These terms allow us to indicate the main sources of eddy kinetic energy to the system. There is the predominance of barotropic instability for $HSP > 0$, while baroclinc instability dominates for $BP > 0$ and vertical shear instability for $VSP > 0$.

Figure 7.5 shows the mean terms of kinetic energy conversion at 1000 m, that reflects the days of eddy formation. It also indicates that HSP and BP are the main sources of eddy kinetic energy. In the eastern opening, area 2, we have predominantly the development of barotropic instability that evolves adjacent to the southern slope of the CSR, inducing the formation of

anticyclonic eddies.

In the CSR northern slope opening at 35°W, area 1, there are two mechanisms responsible for generating the eddies (Figure 7.5). First, we have a strong conversion from the eddy potential energy to the eddy kinetic energy, indicating the presence of baroclinic instability. Second, immediately southward of the baroclinic instability site, there is a strong conversion from the mean to the eddy kinetic energy due to horizontal shear production, indicating the presence of barotropic instability. Both these processes allow the formation of the cyclones and anticyclones.

At area 3, the cyclonic eddies are generated close to the western tip of the CSR northern slope opening about 35°W. They are formed mainly due to horizontal shear production, in other words, barotropic instability (Figure 7.5).

Submesoscale Instability

The PDF analyses reveals the presence of $fq < 0$ values that establishes a necessary condition to the formation of submesoscale instabilities (Thomas et al., 2013). Based on that, we explore the possibility that these processes are ones which triggers the eddy formation.

Submesoscale instabilities are responsible for creating the connection that transfers energy from the mesoscale towards the dissipation, being part of the forward cascade of kinetic energy (Capet et al., 2008b). There are several submesoscale instability processes, each with its own particularities. Their formation depends on the factor responsible for producing low potential voticity, that might be caused by the fluid baroclinicity, vertical vorticity or stratification (Thomas et al., 2013). The symmetric instability develops when the baroclinicity of the flow are responsible for reducing the potential vorticity, and extracts kinetic energy from the geostrophic flow vertical shear (Thomas et al., 2013). The gravitational instability happens when the flow present unstable stratification, i.e. $N^2 < 0$, that allows the increase of the kinetic energy fed by buoyancy fluxes (Thomas et al., 2013). In turn, the inertial (or centrifugal) instability occurs due to horizontal shear only in anticyclonic features (Thomas et al., 2013; Gula et al., 2016b), and the relative vorticity is stronger than planetary vorticity (Gula et al., 2016b). Thomas et al. (2013) develop theory by which it is possible identify the instability type by the sources of kinetic

energy. The instabilities can be differentiate using the following angle:

$$\phi_{Ri_B} = \tan^{-1}\left(-Ri_B^{-1}\right), \tag{7.9}$$

where the balanced Richardson number is defined as

$$Ri_B = \frac{f^2 N^2}{|\nabla_h b|^2}, \tag{7.10}$$

and instability happens when the angle ϕ_{Ri_B} are smaller than the critical angle (ϕ_c):

$$\phi_{Ri_B} < \phi_c \equiv \tan^{-1}\left(-\frac{f+\zeta}{f}\right). \tag{7.11}$$

According to Thomas et al. (2013), a mix of symmetric and gravitational instability arise when -135°< ϕ_{Ri_B} < -90°, and a pure gravitational instability happens when -180°< ϕ_{Ri_B} < -135°. For cyclonic motions, symmetric instability arise when -90°< $\phi_{Ri_B} < \phi_c$. For anticyclonic motions, a mix of inertial and symmetric instability appears when -45°< $\phi_{Ri_B} < \phi_c$, and a pure symmetric instability occurs when -90°< ϕ_{Ri_B} < -45°. However, as explained before, our model just solve the upper part of the submesoscale. To support the fully development of instabilities in the domain, we need a higher resolution eddy resolving model, that will allow more submesoscale instabilities to evolve.

The analysis of submesoscale instabilities in the Figure 7.6 shows that most of the instabilities develop adjacent to the topography, indicating that flow-topography interactions is the main responsible for generating submesoscale instabilities. The mix of inertial and symmetric instability represent most of the instability created in the region, and is one of the triggers responsible for create the perturbations that can develop into eddies in the eastern opening, as it can be observed in Figure 7.6. During the development of the eddies in the eastern opening the flow has Rossby number $\mathcal{O}(1)$ and the $fq < 0$ (Figure 7.6).

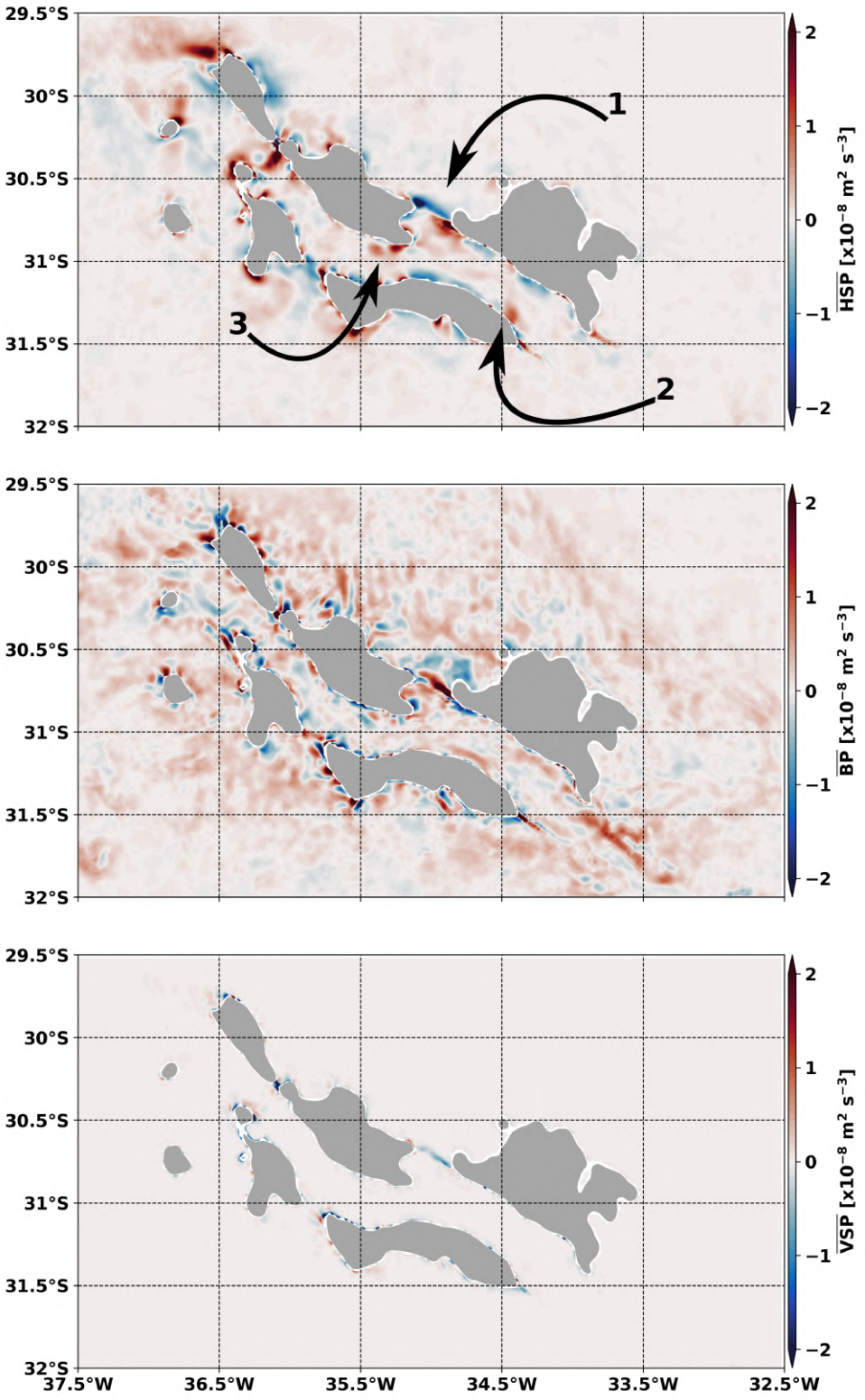

Figure 7.5: Mean kinetic energy conversion terms at 1000 m. Top panel: mean HSP, middle panel: mean BP and lower panel: mean VSP. The arrows in the top panel indicate the sites of eddy formation where (1) shows the CSR northern slope opening at 35°W, (2) shows the CSR south slope in the eastern opening and (3) shows the west tip of the CSR northern slope.

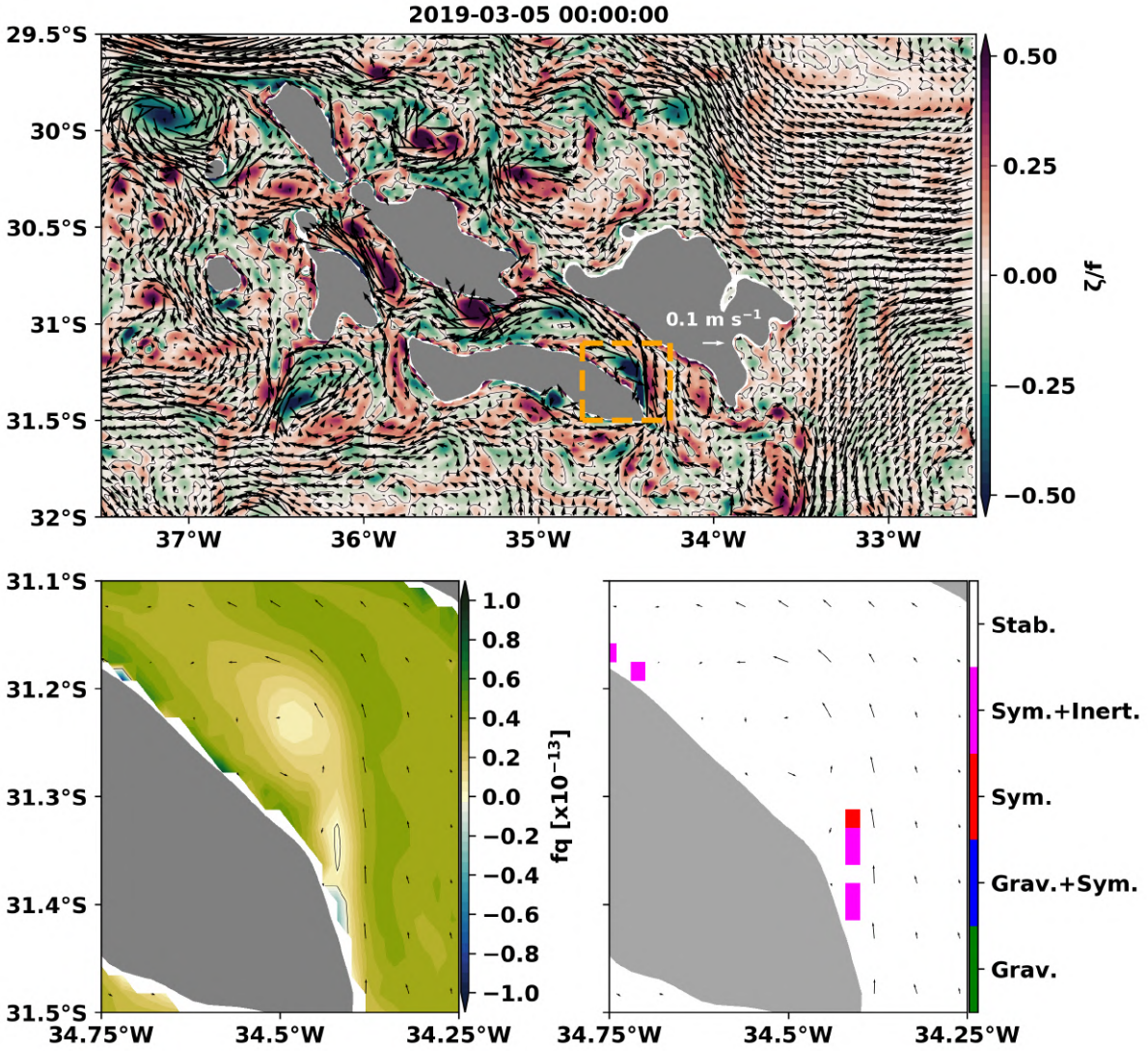

Figure 7.6: 1000 m CROCO model output snapshots. The orange dashed square on the Rossby number map demarks the zoom area of the potential vorticity times Coriolis parameter (fq), and instability maps.

8 Summary and Conclusions

The RGR is the largest plateau in South Atlantic Ocean and has a rift that cuts its structure in the west-east direction, the CSR. We anticipate that a range of dynamical processes might happens around this type of topography based on observations, theoretical approaches and numerical modeling.

In this research, we verify three hypotheses proposed in chapter 1 and focus in basically three major topics: the CSR mean flow, the internal tides and the formation of submesoscale eddies. For the mean field, we report the formation of asymmetric anticyclonic circulations around the RGR summits, that are responsible for creating a cyclonic circulation inside the CSR with the lobe characterized by westward velocities being bigger. In the literature, there exists two major processes that are responsible for allowing the development of this kind of feature: the presence of a impinging mean flow and tidal rectification. In our study area, we have both: a SSEC impinging mean flow, and the presence of intense internal tides dominated by the M2 component. Our analyses reveal that the tidal rectification is the main dynamical process responsible for generating the anticyclonic circulation. Close to the bottom, the anticyclonic velocity pattern remains and can reach 0.2 m s^{-1}. Also, we have the presence of the SSEC that is split in two major branches as it approaches the RGR, with secondary branches being able to force the circulation inside the CSR by the eastern opening and by the opening in the CSR northern slope at 35°W.

Regarding the tidal dynamics, the mooring analyses reveals that most of the variance inside the CSR can be linked directly with the tidal components, mostly the M2 component. In turn, the model reveals the spatial distribution of the M2 component. It shows that the areas with higher tidal amplitudes are in the RGR summits and at the CSR valley, reaching 0.3 m s^{-1}. This pattern can be at least partially explained by the existence of tidal beams that are allowed to develop in areas with steep topography, the CSR slope case. They propagate from the RGR summit in direction to the surface and toward the CSR bottom.

We also show the development of submesoscale eddies inside the CSR. These eddies are formed mainly due to the SSEC forcing, and we sought the processes that yield to their development. In the eastern opening, that is the formation of anticyclonic eddies that has as dynamical

trigger the presence of strong HSP, an indication of barotropic instability, and the development of a mix of inertial and symmetric submesoscale instabilities. In the opening of the CSR northern slope, the formation of cyclones and anticyclones occurs due to BP, an indication of baroclinic instability, followed immediately southward by strong HSP, indicating that barotropic instability also happens. Adjacent to the western tip of the CSR northern slope opening, there is the formation of cyclones that are allowed to develop due to strong HSP conversion, an indication of barotropic instability.

This study was able to answer the proposed scientific questions, as well as verify and confirm all three scientific hypotheses. It was possible due to the analyses made in a skilled hydrodynamical circulation model. Follow the answers to the scientific questions:

- **How is the mean flow within the CSR?**
  The mean flow is characterized by the formation of an asymmetric anticyclonic circulation around the RGR summits primarily due to tidal rectification. This asymmetric anticyclonic circulation causes the circulation within the CSR to be predominantly westward.

- **How is the distribution of the internal tides inside the CSR?**
  The internal tides are dominated mainly by the M2 component with higher velocity amplitudes over the RGR summits and in CSR valley. The velocity amplitude can reach 0.3 m s^{-1}. Also, duo to the steep topography, it tends to propagate along tidal beams.

- **If SSEC enters the CSR, how is it responsible for modifying the flow?**
  The model shows that the SSEC is mainly responsible for forcing the submesoscale motions inside the CSR. The SSEC entrance causes the development of submesoscale eddies of both polarities inside the CSR.

- **How the mean flow and the internal waves near the bottom can control the sediment distribution and exposure of Fe-Mn crusts?**
  Close to the bottom of the RGR summit, we have the presence of an anticyclonic circulation that can reach 0.2 m s^{-1} and a M2 tidal amplitude that can reach 0.3 m s^{-1}. Probably, both processes are responsible for controlling the distribution of different substrates at the RGR, such as the areas of Fe-Mn crusts and dunes.

9 Future Work

Despite the effort carried out by this thesis to characterize the local RGR dynamics, much is still not known. One of the principal and more important task that must be done is the acquisition of additional *in-situ* data to either confirm or expand the dynamical processes observed through the numerical model. The best way to do that is installing mooring arrays along the RGR, to observe the mean anticyclonic circulation, the passage of eddies and the tidal variability along the water column.

Besides that, we know that submesoscale process occur on lateral scales of 0.1-10 km. Due to the horizontal resolution of our model (1/50°) the submesoscale processes and associated instabilities are partially resolved, only the upper limit of this range of motion is resolved. For scales smaller than those resolved by the model, we have the subgrid effects arising from the parameterizations. It makes necessary run a model with a horizontal resolution of at least 1/100° and 50 vertical levels to better resolve and understand the submesoscale processes that responsible for re-distribute water properties, including buoyancy, momentum, heat, biogeochemical tracers, and enhanced vertical exchanges. In addition, we acknowledge that the submesoscale instability criteria can be improved using the curvature effect established by the recent work of Buckingham et al. (2021) and that the mean fields in the energy analysis can be reduced for periods lower than 60 days, for example, 7 days.

Also, it is necessary to understand the dynamics at the top of the RGR and its surroundings. Since the current thesis focuses on the dynamics inside the CSR. Furthermore, couple a sediment dispersion module with the hydrodynamic model to understand the sediment dispersion and deposition pattern over the RGR is essential to future Fe-Mn crusts exploration.

Bibliography

Bashmachnikov, I., Loureiro, C., Martins, A., 2013. Topographically induced circulation patterns and mixing over Condor seamount. Deep Sea Research Part II: Topical Studies in Oceanography 98, 38–51.

Beckers, J.-M., Rixen, M., 2003. EOF calculations and data filling from incomplete oceanographic datasets. Journal of Atmospheric and oceanic technology 20 (12), 1839–1856.

Beckmann, A., Haidvogel, D. B., 1993. Numerical simulation of flow around a tall isolated seamount. Part I: Problem formulation and model accuracy. Journal of Physical Oceanography 23 (8), 1736–1753.

Benites, M., Hein, J. R., Mizell, K., Blackburn, T., Jovane, L., 2020. Genesis and evolution of ferromanganese crusts from the summit of Rio Grande Rise, Southwest Atlantic Ocean. Minerals 10 (4), 349.

Boebel, O., Davis, R., Ollitrault, M., Peterson, R., Richardson, P., Schmid, C., Zenk, W., 1999. The intermediate depth circulation of the western South Atlantic. Geophysical Research Letters 26 (21), 3329–3332.

Buckingham, C. E., Gula, J., Carton, X., 2021. The role of curvature in modifying frontal instabilities. Part I: review of theory and presentation of a nondimensional instability criterion. Journal of Physical Oceanography 51 (2), 299–315.

Camboa, L. A. P., Rabinowitz, P. D., 1984. The evolution of the Rio Grande Rise in the Southwest Atlantic Ocean. Marine Geology 58 (1-2), 35–58.

Capet, X., McWilliams, J. C., Molemaker, M. J., Shchepetkin, A. F., 2008a. Mesoscale to submesoscale transition in the California Current System. Part I: Flow structure, eddy flux, and observational tests. Journal of physical oceanography 38 (1), 29–43.

Capet, X., McWilliams, J. C., Molemaker, M. J., Shchepetkin, A. F., 2008b. Mesoscale to submesoscale transition in the California Current System. Part III: Energy balance and flux. Journal of Physical Oceanography 38 (10), 2256–2269.

Cavalcanti, J. A. D., Santos, R. V., Lacasse, C. M., Rojas, J. N. L., Nobrega, M., 2015. Potential mineral resources of phosphates and trace elements on the Rio Grande Rise, South Atlantic Ocean. Nearshore Underwater Mining: Critical Commodities for the Future UMC.

Chapman, D. C., Haidvogel, D. B., 1992. Formation of Taylor caps over a tall isolated seamount in a stratified ocean. Geophysical & Astrophysical Fluid Dynamics 64 (1-4), 31–65.

Chen, C., Beardsley, R. C., 1995. A numerical study of stratified tidal rectification over finite-amplitude banks. Part I: Symmetric banks. Journal of Physical Oceanography 25 (9), 2090–2110.

CMEMS, 2021. CMEMS: Copernicus Marine Modelling Service global ocean physics reanalysis product (GLORYS12V1), CMEMS [data set]. https://doi.org/10.48670/moi-00021.

Egbert, G. D., Erofeeva, S. Y., 2002. Efficient inverse modeling of barotropic ocean tides. Journal of Atmospheric and Oceanic technology 19 (2), 183–204.

Fernandez, E., Lellouche, J. M., 2018. Product User Manual for the Global Ocean Physical Reanalysis Product GLOBAL_REANALYSIS_PHY_001_030, 15.

Garabato, A. C. N., Frajka-Williams, E. E., Spingys, C. P., Legg, S., Polzin, K. L., Forryan, A., Abrahamsen, E. P., Buckingham, C. E., Griffies, S. M., McPhail, S. D., et al., 2019. Rapid mixing and exchange of deep-ocean waters in an abyssal boundary current. Proceedings of the National Academy of Sciences 116 (27), 13233–13238.

Garzoli, S. L., Matano, R., 2011. The South Atlantic and the Atlantic Meridional Overturning Circulation. Deep Sea Research Part II: Topical Studies in Oceanography 58 (17-18), 1837–1847.

GEBCO Bathymetric Compilation Group 2021, 2021. The GEBCO_2021 Grid-a continuous terrain model of the global oceans and land.

González-Pola, C., del Río, G. D., Ruiz-Villarreal, M., Sánchez, R. F., Mohn, C., 2012. Circulation patterns at Le Danois Bank, an elongated shelf-adjacent seamount in the Bay of Biscay. Deep Sea Research Part I: Oceanographic Research Papers 60, 7–21.

Gounou, A., Drévillon, M., Clavier, M., 2019. Product User Manual for Global Ocean Reanalysis Product GLOBAL-REANALYSIS-PHY-001-031, 32.

Gula, J., Molemaker, M. J., McWilliams, J. C., 2015. Gulf Stream dynamics along the Southeastern US Seaboard. Journal of Physical Oceanography 45 (3), 690–715.

Gula, J., Molemaker, M. J., McWilliams, J. C., 2016a. Submesoscale dynamics of a Gulf Stream frontal eddy in the South Atlantic Bight. Journal of Physical Oceanography 46 (1), 305–325.

Gula, J., Molemaker, M. J., McWilliams, J. C., 2016b. Topographic generation of submesoscale centrifugal instability and energy dissipation. Nature communications 7 (1), 1–7.

Gula, J., Taylor, J., Shcherbina, A., Mahadevan, A., 2022. Submesoscale processes and mixing. In: Ocean Mixing. Elsevier, pp. 181–214.

Guo, B., Wang, W., Shu, Y., He, G., Zhang, D., Deng, X., Liang, Q., Yang, Y., Xie, Q., Wang, H., et al., 2020. Observed deep anticyclonic cap over Caiwei Guyot. Journal of Geophysical Research: Oceans 125 (10), e2020JC016254.

Haidvogel, D. B., Beckmann, A., Chapman, D. C., Lin, R.-Q., 1993. Numerical simulation of flow around a tall isolated seamount. Part II: Resonant generation of trapped waves. Journal of physical oceanography 23 (11), 2373–2391.

Harlamov, V., Lisniowski, M., Frazão, E., Pessoa, J., Aguiar, R., Lopes, V., Nobrega, M., Lisboa, M., Simões, H., Cavalacanti, J., et al., 2015. Preliminary results on mid-depth circulation features on Rio Grande Rise. In: 2015 IEEE/OES Acoustics in Underwater Geosciences Symposium (RIO Acoustics). IEEE, pp. 1–8.

Harrison, D., Robinson, A., 1978. Energy analysis of open regions of turbulent flows—Mean eddy energetics of a numerical ocean circulation experiment. Dynamics of Atmospheres and Oceans 2 (2), 185–211.

Hein, J. R., Mizell, K., Koschinsky, A., Conrad, T. A., 2013. Deep-ocean mineral deposits as a source of critical metals for high-and green-technology applications: Comparison with land-based resources. Ore Geology Reviews 51, 1–14.

Hersbach, H., Bell, B., Berrisford, P., Biavati, G., Horányi, A., Muñoz Sabater, J., Nicolas, J., Peubey, C., Radu, R., Rozum, I., et al., 2018. ERA5 hourly data on pressure levels from 1979 to present, Copernicus Climate Change Service (C3S) Climate Data Store (CDS).

Jovane, L., Hein, J. R., Yeo, I. A., Benites, M., Bergo, N. M., Correa, P. V. F., Couto, D. d. M., Guimarães, A. D. F., Howarth, S. A., Miguel, H., et al., 2019. Multidisciplinary scientific cruise to the Rio Grande Rise. Frontiers in Marine Science 6, 252.

Jullien, S., Caillaud, M., Benshila, R., Bordois, L., Cambon, G., Dumas, F., 2019. Technical and numerical doc. Retrieved from https://www.croco-ocean.org/documentation/.

Lahaye, N., Gula, J., Thurnherr, A. M., Reverdin, G., Bouruet-Aubertot, P., Roullet, G., 2019. Deep currents in the rift valley of the North Mid-Atlantic Ridge. Frontiers in Marine Science 6, 597.

Large, W. G., McWilliams, J. C., Doney, S. C., 1994. Oceanic vertical mixing: A review and a model with a nonlocal boundary layer parameterization. Reviews of Geophysics 32 (4), 363–403.

Lazaneo, C., Calil, P., Tandon, A., da Silveira, I., 2022. Submesoscale coherent vortices in the South Atlantic Ocean: A pathway for energy dissipation. Journal of Geophysical Research: Oceans 127 (2), e2020JC017099.

LeBlond, P. H., Mysak, L. A., 1981. Waves in the Ocean. Elsevier.

Legeais, J.-F., Ollitrault, M., Arhan, M., 2013. Lagrangian observations in the Intermediate Western Boundary Current of the South Atlantic. Deep Sea Research Part II: Topical Studies in Oceanography 85, 109–126.

Lemarié, F., Kurian, J., Shchepetkin, A. F., Molemaker, M. J., Colas, F., McWilliams, J. C., 2012. Are there inescapable issues prohibiting the use of terrain-following coordinates in climate models? Ocean Modelling 42, 57–79.

Lisniowski, M. A., 2020. Caracterização de potenciais habitats bentônicos na elevação do Rio Grande. Ph.D. thesis.

Lisniowski, M. A., Harlamov, V., Frazão, E. P., Pessanha, I. B., Neto, A. A., 2017. Sediment waves on the Rio Grande Rise. In: 2017 IEEE/OES Acoustics in Underwater Geosciences Symposium (RIO Acoustics). IEEE, pp. 1–5.

Locarnini, M., Mishonov, A., Baranova, O., Boyer, T., Zweng, M., Garcia, H., Seidov, D., Weathers, K., Paver, C., Smolyar, I., et al., 2018. World Ocean Atlas 2018, volume 1: Temperature.

Luko, C., Silveira, I., Simoes-Sousa, I., Araujo, J., Tandon, A., 2021. Revisiting the Atlantic South Equatorial Current. Journal of Geophysical Research: Oceans 126 (7), e2021JC017387.

Mahadevan, A., 2016. The impact of submesoscale physics on primary productivity of plankton. Annual Review of Marine Science 8, 161–184.

Mahadevan, A., Tandon, A., 2006. An analysis of mechanisms for submesoscale vertical motion at ocean fronts. Ocean Modelling 14 (3-4), 241–256.

Marchesiello, P., Debreu, L., Couvelard, X., 2009. Spurious diapycnal mixing in terrain-following coordinate models: The problem and a solution. Ocean Modelling 26 (3-4), 156–169.

Marez, C., Carton, X., Corréard, S., L'Hégaret, P., Morvan, M., 2020. Observations of a deep submesoscale cyclonic vortex in the Arabian Sea. Geophysical Research Letters 47 (13), e2020GL087881.

Molemaker, M. J., McWilliams, J. C., Dewar, W. K., 2015. Submesoscale instability and generation of mesoscale anticyclones near a separation of the California Undercurrent. Journal of Physical Oceanography 45 (3), 613–629.

Montserrat, F., Guilhon, M., Corrêa, P. V. F., Bergo, N. M., Signori, C. N., Tura, P. M., de los Santos Maly, M., Moura, D., Jovane, L., Pellizari, V., et al., 2019. Deep-sea mining on the Rio Grande Rise (Southwestern Atlantic): A review on environmental baseline, ecosystem services and potential impacts. Deep Sea Research Part I: Oceanographic Research Papers 145, 31–58.

Müller, P., McWilliams, J., Molemaker, M., 2005. Routes to dissipation in the ocean: The 2D/3D turbulence conundrum. Marine turbulence: theories, observations and models 397, 405.

Napolitano, D., da Silveira, I., Tandon, A., Calil, P., 2021. Submesoscale Phenomena Due to the Brazil Current Crossing of the Vitória-Trindade Ridge. Journal of Geophysical Research: Oceans 126 (1), e2020JC016731.

Núñez-Riboni, I., Boebel, O., Ollitrault, M., You, Y., Richardson, P. L., Davis, R., 2005. Lagrangian circulation of Antarctic Intermediate Water in the subtropical South Atlantic. Deep Sea Research Part II: Topical Studies in Oceanography 52 (3-4), 545–564.

Pacanowski, R., Philander, S., 1981. Parameterization of vertical mixing in numerical models of tropical oceans. Journal of Physical Oceanography 11 (11), 1443–1451.

Pawlowicz, R., Beardsley, B., Lentz, S., 2002. Classical tidal harmonic analysis including error estimates in matlab using t_tide. Computers & Geosciences 28 (8), 929–937.

Pereira, A., Castro, B., Calado, L., da Silveira, I., 2007. Numerical simulation of M2 internal tides in the South Brazil Bight and their interaction with the Brazil Current. Journal of Geophysical Research: Oceans 112 (C4).

Peterson, R. G., Stramma, L., 1991. Upper-level circulation in the South Atlantic Ocean. Progress in oceanography 26 (1), 1–73.

Praxedes, A. G. P., de Castro, D. L., Torres, L. C., Gambôa, L. A. P., Hackspacher, P. C., 2019. New insights of the tectonic and sedimentary evolution of the Rio Grande Rise, South Atlantic Ocean. Marine and Petroleum Geology 110, 335–346.

Rocha, C. B., da Silveira, I. C., Castro, B. M., Lima, J. A. M., 2014. Vertical structure, energetics, and dynamics of the Brazil Current System at 22 S–28 S. Journal of Geophysical Research: Oceans 119 (1), 52–69.

Rocha, C. B., Gille, S. T., Chereskin, T. K., Menemenlis, D., 2016. Seasonality of submesoscale dynamics in the Kuroshio Extension. Geophysical Research Letters 43 (21), 11–304.

Rodrigues, R. R., Rothstein, L. M., Wimbush, M., 2007. Seasonal variability of the South Equatorial Current bifurcation in the Atlantic Ocean: A numerical study. Journal of Physical Oceanography 37 (1), 16–30.

Ruan, X., Thompson, A. F., Flexas, M. M., Sprintall, J., 2017. Contribution of topographically generated submesoscale turbulence to Southern Ocean overturning. Nature Geoscience 10 (11), 840–845.

Santos, R. V., Ganade, C. E., Lacasse, C. M., Costa, I. S., Pessanha, I., Frazão, E. P., Dantas, E. L., Cavalcante, J. A., 2019. Dating Gondwanan continental crust at the Rio Grande Rise, South Atlantic. Terra Nova 31 (5), 424–429.

Shchepetkin, A. F., 2015. An adaptive, Courant-number-dependent implicit scheme for vertical advection in oceanic modeling. Ocean Modelling 91, 38–69.

Shchepetkin, A. F., McWilliams, J. C., 1998. Quasi-monotone advection schemes based on explicit locally adaptive dissipation. Monthly weather review 126 (6), 1541–1580.

Shchepetkin, A. F., McWilliams, J. C., 2003. A method for computing horizontal pressure-gradient force in an oceanic model with a nonaligned vertical coordinate. Journal of Geophysical Research: Oceans 108 (C3).

Shchepetkin, A. F., McWilliams, J. C., 2005. The regional oceanic modeling system (ROMS): a split-explicit, free-surface, topography-following-coordinate oceanic model. Ocean Modelling 9 (4), 347–404.

Shcherbina, A. Y., D'Asaro, E. A., Lee, C. M., Klymak, J. M., Molemaker, M. J., McWilliams, J. C., 2013. Statistics of vertical vorticity, divergence, and strain in a developed submesoscale turbulence field. Geophysical Research Letters 40 (17), 4706–4711.

Silva, A. P., 2021. Brazil advances over the Area: The inclusion of the Rio Grande Rise within the Brazilian outer continental shelf and its consequences for other states and for the common heritage of mankind. Marine Policy 125, 104399.

Silveira, I., Calado, L., Castro, B., Cirano, M., Lima, J., Mascarenhas, A. d. S., 2004. On the

baroclinic structure of the brazil current–intermediate western boundary current system at 22–23 s. Geophysical Research Letters 31 (14).

Silveira, I. C. A., Schmidt, A. C. K., Campos, E. J. D., Godoi, S. S. d., Ikeda, Y., 2000. A corrente do Brasil ao largo da costa leste brasileira. Revista Brasileira de Oceanografia 48 (2), 171–183.

Simoes-Sousa, I. T., Silveira, I. C. A., Tandon, A., Flierl, G. R., Ribeiro, C. H., Martins, R. P., 2021. The Barreirinhas Eddies: Stable energetic anticyclones in the near-equatorial South Atlantic. Frontiers in Marine Science.

Soufflet, Y., Marchesiello, P., Lemarié, F., Jouanno, J., Capet, X., Debreu, L., Benshila, R., 2016. On effective resolution in ocean models. Ocean Modelling 98, 36–50.

Srinivasan, K., McWilliams, J. C., Molemaker, M. J., Barkan, R., 2019. Submesoscale vortical wakes in the lee of topography. Journal of Physical Oceanography 49 (7), 1949–1971.

Stashchuk, N., Vlasenko, V., 2017. Bottom trapped internal waves over the Malin Sea continental slope. Deep Sea Research Part I: Oceanographic Research Papers 119, 68–80.

Stramma, L., 1991. Geostrophic transport of the South Equatorial Current in the Atlantic. Journal of Marine Research 49 (2), 281–294.

Stramma, L., England, M., 1999. On the water masses and mean circulation of the South Atlantic Ocean. Journal of Geophysical Research: Oceans 104 (C9), 20863–20883.

Thomas, L. N., Tandon, A., Mahadevan, A., 2008. Submesoscale processes and dynamics. Ocean modeling in an Eddying Regime 177, 17–38.

Thomas, L. N., Taylor, J. R., Ferrari, R., Joyce, T. M., 2013. Symmetric instability in the Gulf Stream. Deep Sea Research Part II: Topical Studies in Oceanography 91, 96–110.

Thomson, R. E., Emery, W. J., 2014. Data analysis methods in physical oceanography. Newnes.

Thurnherr, A., 2018. How to process LADCP data with the LDEO software. version IX.13.

Valla, D., Piola, A. R., Meinen, C. S., Campos, E., 2018. Strong mixing and recirculation in the Northwestern Argentine Basin. Journal of Geophysical Research: Oceans 123 (7), 4624–4648.

Vic, C., Gula, J., Roullet, G., Pradillon, F., 2018. Dispersion of deep-sea hydrothermal vent effluents and larvae by submesoscale and tidal currents. Deep Sea Research Part I: Oceanographic Research Papers 133, 1–18.

Vlasenko, V., Stashchuk, N., Hutter, K., 2005. Baroclinic tides: theoretical modeling and observational evidence. Cambridge University Press.

Vlasenko, V., Stashchuk, N., Inall, M. E., Hopkins, J. E., 2014. Tidal energy conversion in a global hot spot: On the 3-D dynamics of baroclinic tides at the Celtic Sea shelf break. Journal of Geophysical Research: Oceans 119 (6), 3249–3265.

Vlasenko, V., Stashchuk, N., Inall, M. E., Porter, M., Aleynik, D., 2016. Focusing of baroclinic tidal energy in a canyon. Journal of Geophysical Research: Oceans 121 (4), 2824–2840.

Vlasenko, V., Stashchuk, N., Nimmo-Smith, W. A. M., 2018. Three-dimensional dynamics of baroclinic tides over a seamount. Journal of Geophysical Research: Oceans 123 (2), 1263–1285.

Whitt, D. B., Thomas, L. N., Klymak, J. M., Lee, C. M., D'Asaro, E. A., 2018. Interaction of superinertial waves with submesoscale cyclonic filaments in the north wall of the Gulf Stream. Journal of Physical Oceanography 48 (1), 81–99.

Xu, G., Lavelle, J., 2017. Circulation, hydrography, and transport over the summit of Axial Seamount, a deep volcano in the Northeast Pacific. Journal of Geophysical Research: Oceans 122 (7), 5404–5422.

Yeo, I., Howarth, S., Spearman, J., Cooper, A., Crossouard, N., Taylor, J., Turnbull, M., Murton, B., 2019. Distribution of and hydrographic controls on ferromanganese crusts: tropic seamount, Atlantic. Ore Geology Reviews 114, 103131.

Zweng, M., Seidov, D., Boyer, T., Locarnini, M., Garcia, H., Mishonov, A., Baranova, O., Weathers, K., Paver, C., Smolyar, I., et al., 2019. World Ocean Atlas 2018, volume 2: Salinity.